Deposition or diagenesis? Probing the Ediacaran Shuram excursion in South China by SIMS☆

Huan Cui [a,b,c,d,*], Kouki Kitajima [c], Ian J. Orland [c,e], Shuhai Xiao [f], Jean-Marc Baele [g], Alan J. Kaufman [h], Adam Denny [c,i], Chuanming Zhou [j], Michael J. Spicuzza [c], John H. Fournelle [c], John W. Valley [c,d]

[a] Equipe Géomicrobiologie, Institut de Physique du Globe de Paris (IPGP), Université de Paris, 75005 Paris, France
[b] Stable Isotope Laboratory, Department of Earth Sciences, University of Toronto, Toronto, ON M5S 3B1, Canada
[c] Department of Geoscience, University of Wisconsin–Madison, Madison, WI 53706, USA
[d] NASA Astrobiology Institute, University of Wisconsin–Madison, Madison, WI 53706, USA
[e] Wisconsin Geological and Natural History Survey, University of Wisconsin–Madison, Madison, WI 53705, USA
[f] Department of Geosciences, Virginia Tech, Blacksburg, VA 24061, USA
[g] Department of Geology, Faculty of Engineering, University of Mons, 7000 Mons, Belgium
[h] Department of Geology and Earth System Science Interdisciplinary Center, University of Maryland, College Park, MD 20742, USA
[i] Pacific Northwest National Laboratory, Richland, WA 99354, USA
[j] State Key Laboratory of Palaeobiology and Stratigraphy, Nanjing Institute of Geology and Palaeontology, and Center for Excellence in Life and Paleoenvironment, Chinese Academy of Sciences, Nanjing 210008, China

ARTICLE INFO

ABSTRACT

The Ediacaran Period (ca. 635–541 Ma) witnessed the earliest paleontological evidence for macroscopic animals (i.e., Ediacara biota) and geochemical observations of the largest carbon cycle anomaly in Earth history (i.e., Shuram Excursion, SE). Numerous hypotheses have been proposed for the origins of the SE, ranging from primary seawater anomaly to syn- or post-depositional diagenesis. Despite intensive geochemical and theoretical work published in the past decade, empirical evidence that is strictly based on fundamental petrographic results at the micrometer scale is still limited. To evaluate depositional compositions and diagenetic effects on samples from the SE, we investigated the EN3 interval in the Doushantuo Formation of South China via integrated cathodoluminescence (CL), secondary ion mass spectrometry (SIMS), and scanning electron microscope (SEM). Detailed petrographic observations reveal that the EN3 limestone is dominated by calcite microspar, with minor but variable amounts of disseminated zoned dolomite crystals. The former likely formed via neomorphism of depositional micrite, while the latter was the result of progressive post-depositional dolomitization. The mean values of paired SIMS $\delta^{13}C_{calcite}$ and $\delta^{13}C_{dolomite}$ compositions are indistinguishable in each sample and consistent with published micro-drilled bulk-powder $\delta^{13}C$ values, which we interpret to represent depositional "background" signals of seawater dissolved inorganic carbon (DIC). We also observed μm-scale variability of SIMS $\delta^{13}C$ data that may reflect a variable diagenetic overprint after deposition. Our integrated petrographic and geochemical results are consistent with a depositional origin of the SE and provide little evidence for the hypothesized isotope alteration by meteoric and mixing-zone diagenesis or late burial diagenesis. In light of this study, we propose that the SE indeed represents a marine carbon cycle anomaly that bears a close temporal link to the Ediacaran surface environment.

1. Introduction

The globally recorded middle Ediacaran Shuram Excursion (SE) is widely regarded as one of the largest carbonate carbon isotope ($\delta^{13}C_{carb}$) negative anomalies preserved in bedded marine carbonates in Earth's history (Grotzinger et al., 2011). Typically, the SE is characterized by $\delta^{13}C_{carb}$ values that plunge from background values of ca. $+5‰$ to a nadir of ca. $-12‰$ over a short stratigraphic interval and then rise steadily in the overlying tens to hundreds of meters before recovering back to positive values (Burns and Matter, 1993; Fike et al., 2006; McFadden et al., 2008; Grotzinger et al., 2011; Husson et al., 2015b). Various hypotheses have been proposed for the SE, ranging from primary biogeochemical perturbations (Fike et al., 2006; Kaufman et al., 2007; Lu et al., 2013; Husson et al., 2015a; Shields et al., 2019; Zhang et al., 2019; Li et al., 2020) to a wide spectrum of diagenetic processes, including early syndepositional diagenesis (Schrag et al., 2013; Cui et al., 2017; Jiang et al., 2019), meteoric and mixing-zone diagenesis (Knauth and Kennedy, 2009; Zhao et al., 2020), and late burial diagenesis (Derry, 2010). More recently, hypotheses that link mantle-derived deep carbon to the SE have also been proposed (Paulsen et al., 2017; Cui, 2021; Liu et al., 2021). Given the close relationship between the SE and the earliest fossil evidence of macroscopic animals (Xiao et al., 2016; Darroch et al., 2018; Rooney et al., 2020; Xiao and Narbonne, 2020), a better understanding of the effect of diagenesis on the SE is thus critical to unraveling the causal link between the deep-time carbon cycle and early animal evolution.

Although post-depositional diagenesis has been repeatedly invoked to explain the SE (Knauth and Kennedy, 2009; Derry, 2010; Zhao et al., 2020), whether it has played a pivotal role in the preservation of anomalously negative $\delta^{13}C$ compositions of carbonates remains ambiguous. Why, for example, is the middle Ediacaran Period the only time in Earth history that diagenesis imparted such a strong and lasting signal on $\delta^{13}C$ composition of sedimentary carbonates when similar alteration processes must have been active in the succeeding Paleozoic and younger intervals? Fortunately, diagenesis can leave distinct petrographic and geochemical fingerprints (Scholle and Ulmer-Scholle, 2003; Tucker et al., 2009), so that high spatial resolution investigations of SE carbonates hold the potential to better constrain its origins. In recent years, in situ analysis of sedimentary carbonates by scanning electron microscope (SEM) and secondary ion mass spectrometer (SIMS) has emerged to be a powerful tool in uncovering their complex diagenetic histories (Śliwiński et al., 2016b; Andrieu et al., 2017; Denny et al., 2017; Śliwiński et al., 2017; Cui et al., 2019a; Xiao et al., 2019; Denny et al., 2020; Husson et al., 2020; Xiao et al., 2020b). Detailed SEM–SIMS analysis can reveal information with much higher spatial resolution than the traditional sampling approach of micro-drilling. Notably, a recent SIMS study of the SE-equivalent Wonoka Formation in South Australia reveals large $\delta^{13}C_{carb}$ variability at a μm scale (Husson et al., 2020), suggesting complex depositional and diagenetic processes.

Despite intensive studies on the SE, no samples from the SE interval in South China have been investigated by SIMS in high spatial resolution. Here, we conduct a μm-scale study on samples from the SE-equivalent EN3 interval of the Doushantuo Formation in South China via integrated cathodoluminescence (CL), SEM and SIMS analysis. The main goals of this study are (1) to further constrain the diagenetic histories of SE samples in South China through detailed petrographic observations; (2) to evaluate the variability of $\delta^{13}C_{carb}$ at a micrometer scale; (3) to compare the SIMS data with previous published $\delta^{13}C_{carb}$ data measured on micro-drilled powders of the Doushantuo samples (McFadden et al., 2008); (4) to compare the SIMS data from EN3 with the recently published SIMS data from the Wonoka Formation, South Australia (Husson et al., 2020); and finally (5) to evaluate some of the published hypotheses for the SE (Knauth and Kennedy, 2009; Derry, 2010; Zhao et al., 2020) based on our new results.

2. Background

2.1. Geological background

Ediacaran successions in the Yangtze block of South China (Fig. 1A, B) include the richly fossiliferous Doushantuo and Dengying formations (Zhou and Xiao, 2007; Zhu et al., 2007b; Zhou et al., 2019; Xiao et al., 2020a). Abundant three-dimensionally preserved eukaryotes, including multicellular algae, acritarchs, and putative animals, have been discovered from phosphorites and chert nodules of the Doushantuo Formation (Xiao et al., 1998; Liu et al., 2014; Xiao et al., 2014; Yin et al., 2015; Cunningham et al., 2017; Ouyang et al., 2017; Liu and Moczydłowska, 2019; Ouyang et al., 2019; Ouyang et al., 2021), while the Dengying Formation contains macroscopic Ediacaran body and trace fossils, including the earliest biomineralizing animals (Xiao et al., 2005; Hua et al., 2007; Cai et al., 2010; Chen et al., 2013; Chen et al., 2014; Meyer et al., 2014; Cui et al., 2016a; Cui et al., 2019b; Liang et al., 2020; Xiao et al., 2020a).

Deposition of the Doushantuo Formation in the Yangtze Craton of South China can be divided into two stages, beginning with an open ramp shelf that gradually transitioned into a rimmed shelf with an intra-shelf basin (Jiang et al., 2011). Stratigraphic data and paleogeographic reconstructions indicate an increase in water depth from proximal intertidal environments in the northwest to distal deep basinal settings in the southeast of the Yangtze Craton. Three platform facies belts are apparent, including a proximal inner shelf dominated by peritidal carbonates, an intra-shelf basin containing mixed carbonates and shales, and an outer shelf shoal complex consisting primarily of carbonates and phosphorites (Fig. 1B).

The basal Doushantuo Formation overlies the Nantuo diamictite and begins with a ca. 635 Ma cap carbonate (Fig. 1C) (Condon et al., 2005). It has been suggested that the uppermost Doushantuo Formation corresponds to a ca. 551 Ma ash bed (Condon et al., 2005), but based on a more recent litho- and chemo-stratigraphic study, this ash bed has been attributed to the Shibantan Member of the Dengying Formation, thereby pushing the Doushantuo-Dengying boundary (and the EN3/Shuram excursion preserved there) back in time (An et al., 2015; see also Zhou et al., 2017 for a different view).

The Doushantuo Formation in the Yangtze Gorges area has been informally divided into four distinct members (Zhou and Xiao, 2007; McFadden et al., 2008) and is typically capped by massive dolostones of the Dengying Formation (Zhu et al., 2007b; Jiang et al., 2011; Zhu et al., 2013). The mixed intra-shelf shale and carbonate succession of the Doushantuo Formation at Jiulongwan, which is well exposed along a road cut made during the construction of the Yangtze Gorges Dam, has a thickness of ~160 m (Jiang et al., 2007; McFadden et al., 2008). The EN3 interval of the Jiulongwan section represents the upper ca. 55 m of the Doushantuo Formation, which is mainly composed of bedded dolostone in the lower 20 m, bedded limestone in the middle ca. 25 m, and black shale with large (meter-sized) carbonate nodules in the upper ca. 10 m of the formation (Figs. 2, 3).

2.2. Chemostratigraphic background

$\delta^{13}C_{carb}$ chemostratigraphy. — Bulk-sample chemostratigraphy of the Doushantuo Formation in South China has been intensively studied (Zhou and Xiao, 2007; Zhu et al., 2007b; Zhou et al., 2012; Ling et al., 2013; Lu et al., 2013; Zhu et al., 2013; Cui et al., 2015; Li et al., 2017). The $\delta^{13}C_{carb}$ profile of the Doushantuo Formation at Jiulongwan shows three discrete Ediacaran Negative (EN) excursions: EN1 in the basal cap carbonate, EN2 in the middle section, and EN3 at the top (Fig. 3A) (Jiang et al., 2007; McFadden et al., 2008; Ling et al., 2013; Tahata et al., 2013). Extremely negative $\delta^{13}C_{carb}$ signals down to $-40‰$ have been reported from the EN1 interval (Jiang et al., 2003; Jiang et al., 2006; Wang et al., 2008; Zhou et al., 2010; Lin et al., 2011; Zhou et al., 2016), although the origin of these signatures, likely to be related to methane
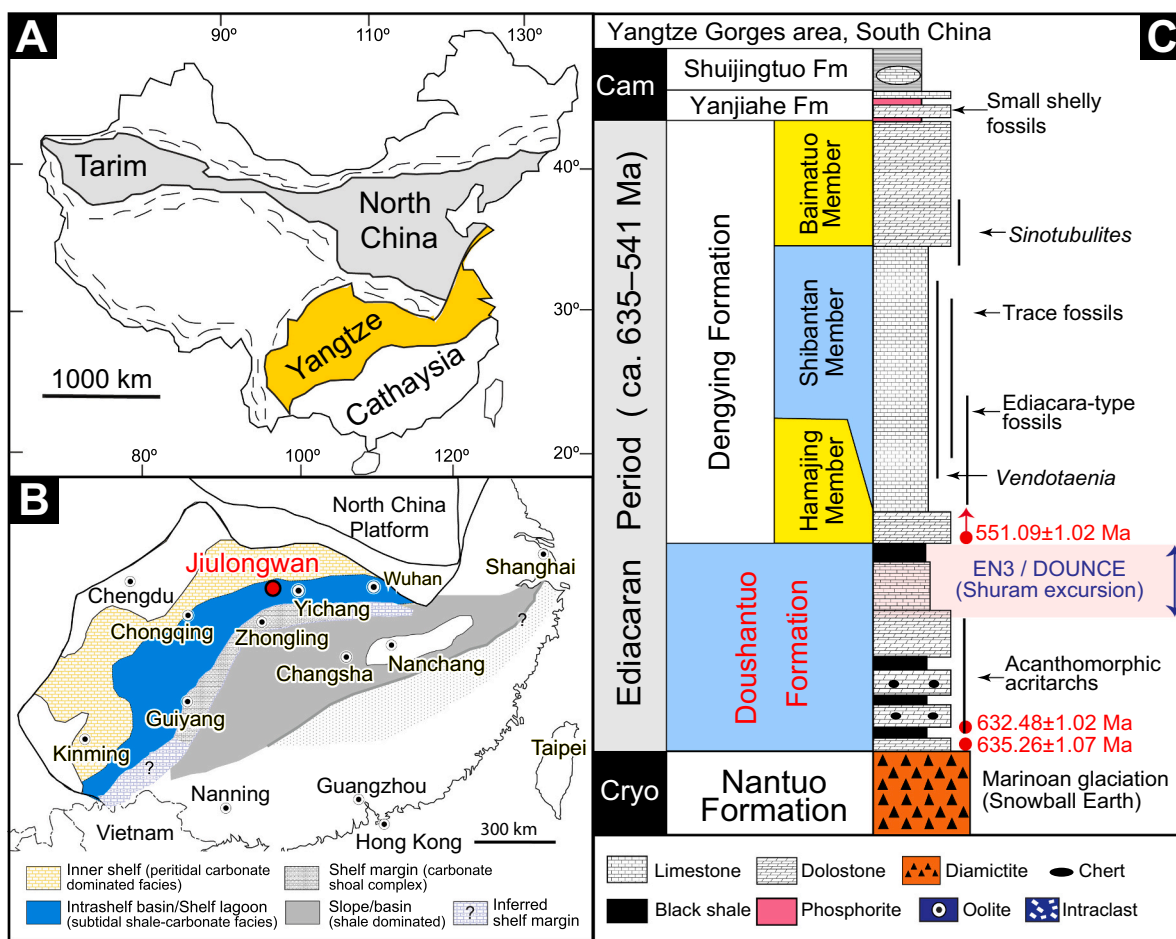
Fig. 1. (**A**) Geological map of China, with the Yangtze block in yellow color. (**B**) Reconstructed Ediacaran depositional environments on the Yangtze Craton (Jiang et al., 2011). Red dot indicates the location of the intra-shelf Jiulongwan section. (**C**) Simplified litho-, bio-, and chrono-stratigraphy of the Ediacaran Doushantuo and Dengying formations in South China. The SE is widely reported from the upper Doushantuo Formation, which is also referred to as N3 (Negative 3) (Jiang et al., 2007; Wang et al., 2016), EN3 (Ediacaran Negative 3) (Zhou and Xiao, 2007; McFadden et al., 2008), or DOUNCE (DOUshantuo Negative Carbon isotope Excursion) (Zhu et al., 2007a; Lu et al., 2013; Zhu et al., 2013). Red-shaded interval denotes the EN3/DOUNCE interval. Modified from Chen et al. (2013) and Cui et al. (2016b). Radiometric ages from Condon et al. (2005) and Schmitz (2012). Note that the stratigraphic assignment of the U-Pb age 551.09 ± 1.02 Ma was initially placed to the Doushantuo–Dengying boundary (Condon et al., 2005), but was later re-assigned to the Shibantan Member of the Dengying Formation (An et al., 2015), although it still remains a matter of debate (Zhou et al., 2017). Thickness is not to scale. Cam = Cambrian; Cryo = Cryogenian. (For interpretation of the references to color in this figure legend, the reader is referred to the web version of this article.)

oxidation, is still highly controversial — both syndepositional (Jiang et al., 2003; Jiang et al., 2006) and post-depositional (Zhou et al., 2010; Bristow et al., 2011; Lin et al., 2011; Cui et al., 2019a) origins have been proposed. EN2 has been proposed to be correlated with the middle Ediacaran Gaskiers glaciation (Tahata et al., 2013), although this age assignment remains a matter of debate (Narbonne et al., 2012; Xiao et al., 2016).

The SE is widely reported from the upper Doushantuo Formation, which is also referred to as N3 (Negative 3) (Jiang et al., 2007; Wang et al., 2016), EN3 (Ediacaran Negative excursion 3) (Zhou and Xiao, 2007; McFadden et al., 2008), or DOUNCE (DOUshantuo Negative Carbon isotope Excursion) (Zhu et al., 2007a; Lu et al., 2013; Zhu et al., 2013).The EN3 interval at Jiulongwan shows a notable $\delta^{13}C_{carb}$ negative excursion from 0‰ down to −9‰ over a five meter interval, remains invariant for another ~40 m, and then recovers back to around 0‰ over the next 15 m (Fig. 3A) (Jiang et al., 2007; McFadden et al., 2008; Zhou et al., 2012; Lu et al., 2013; Tahata et al., 2013; Zhu et al., 2013), and it has been proposed to be correlative with the SE on a global scale (Jiang et al., 2007; Grotzinger et al., 2011). These $\delta^{13}C_{carb}$ excursions have been interpreted as resulting from pulsed oxidation of marine DOC (dissolved organic carbon) reservoirs during deposition (Jiang et al., 2007; McFadden et al., 2008; Ader et al., 2009).

$\delta^{18}O_{carb}$ chemostratigraphy. — Bulk-sample $\delta^{18}O_{carb}$ profile of the EN3 interval at Jiulongwan shows an overall negative excursion down to −10‰ (VPDB), which broadly co-varies with the $\delta^{13}C_{carb}$ profile (Fig. 3A–B). Within the EN3 interval, dolomite-dominated layers show overall higher $\delta^{18}O_{carb}$ than limestone-dominated layers (Fig. 3B), which is likely due to the effect of dolomitization. Covariations of $\delta^{13}C_{carb}$ and $\delta^{18}O_{carb}$ have also been reported from the SE at many other sections worldwide (Grotzinger et al., 2011). Multiple mechanisms have been proposed to account for this correlation, including meteoric water diagenesis (Knauth and Kennedy, 2009; Zhao et al., 2020), burial diagenesis (Derry, 2010), primary paleoclimatic change that involves global warming and glacial melt during deposition (Bjerrum and Canfield, 2011), early authigenesis in shallow marine sediments (Cui et al., 2017), and different degrees of mixing by carbonatite volcanic ash (Liu et al., 2021). Therefore, the origin of this $\delta^{13}C_{carb}$–$\delta^{18}O_{carb}$ covariation still remains a matter of debate.

$\delta^{13}C_{org}$ chemostratigraphy. — Bulk-sample $\delta^{13}C_{org}$ profile of the EN3 interval shows overall consistent values of ca. −26‰ in the lower half of the EN3 interval before decreasing to ca. −38‰ in the Member IV shale interval (Fig. 3C) (McFadden et al., 2008). The decoupled $\delta^{13}C_{carb}$–$\delta^{13}C_{org}$ chemostratigraphic patterns in EN3 do not follow expectations of carbon isotope variations driven by organic carbon burial

Fig. 2. Field outcrops of the upper Doushantuo Formation at the intra-shelf Jiulongwan section, South China. Stratigraphic positions of the field photos have been marked along the lithological column in Fig. 3. **(A)** Dolostones with three distinct, black-colored chert layers (arrows), EP2 interval. Hammer circled as scale. **(B)** A closer view of dolostones with two black-colored chert layers (arrows), EP2 interval; **(C)** Thinly bedded limestones in the EN3b interval. Hammer circled as scale. **(D)** A large carbonate nodule within the Member IV shale (EN3c interval). Hand as scale. **(E)** Stratigraphic boundary between the EN3b interval (limestone in upper Member III) and the EN3c interval (black shale in Member IV). Hammer circled as scale. **(F)** Stratigraphic boundary between Member IV shale and the overlying dolostones of the terminal Ediacaran Dengying Formation. Abbreviations used: EP = Ediacaran positive excursion; EN = Ediacaran negative excursion.

(Hayes, 1993; Kump and Arthur, 1999). Massive oxidation of a large DOC reservoir in the ocean (Rothman et al., 2003; McFadden et al., 2008; Shields et al., 2019) or different degrees of mixing between ^{13}C-depleted primary organic matter and ^{13}C-enriched detrital organic matter (Johnston et al., 2012; Li et al., 2017) has been proposed to explain the decoupled chemostratigraphic patterns of $\delta^{13}C_{carb}$ and $\delta^{13}C_{org}$.

The Member IV interval is dominated by shale (Fig. 2E–F), which shows lower carbonate content (<25%) and higher TOC (>2%, up to 8%) compared with the underlying carbonates (Fig. 3D–E). Large carbonate nodules are abundant in this interval (Fig. 2D, F), which provide opportunities for $\delta^{13}C_{carb}$ and $\delta^{18}O_{carb}$ analysis. Field observations show that the shale laminae surrounding carbonate nodules typically warp around the nodule (Fig. 2D), suggesting that the carbonate nodules were formed during early diagenesis and before sediment compaction. Based on the smooth chemostratigraphic trend of $\delta^{13}C_{carb}$ and the consistently decreasing $\delta^{34}S_{CAS}$ and $\delta^{34}S_{pyrite}$ values (instead of higher $\delta^{34}S$ as would

be expected in restricted conditions) in Member IV (McFadden et al., 2008; Shi et al., 2018), it is likely that the measured $\delta^{13}C_{carb}$ and $\delta^{18}O_{carb}$ data from these carbonate nodules still reflect signals of bottom seawater DIC (dissolved inorganic carbon) that was diffused into shallow pore space of the sediment pile.

3. Samples and analytical methods

3.1. SIMS samples

The focus of this study is the EN3 interval of the Doushantuo Formation at the intra-shelf Jiulongwan section, South China (Figs. 1, 2, 3). The ten samples in this study were collected by McFadden et al. (2008) and span over the entire ca. 55 m of the EN3 interval (Figs. 3, 4; Table 1). These ten samples cover three different lithologies: bedded dolostones (samples S1–3), bedded dolomitic limestones (S4–8), and dolomite nodules (S9–10) (Fig. 4; Table 1). Bulk-sample $\delta^{13}C_{carb}$, $\delta^{18}O_{carb}$, and
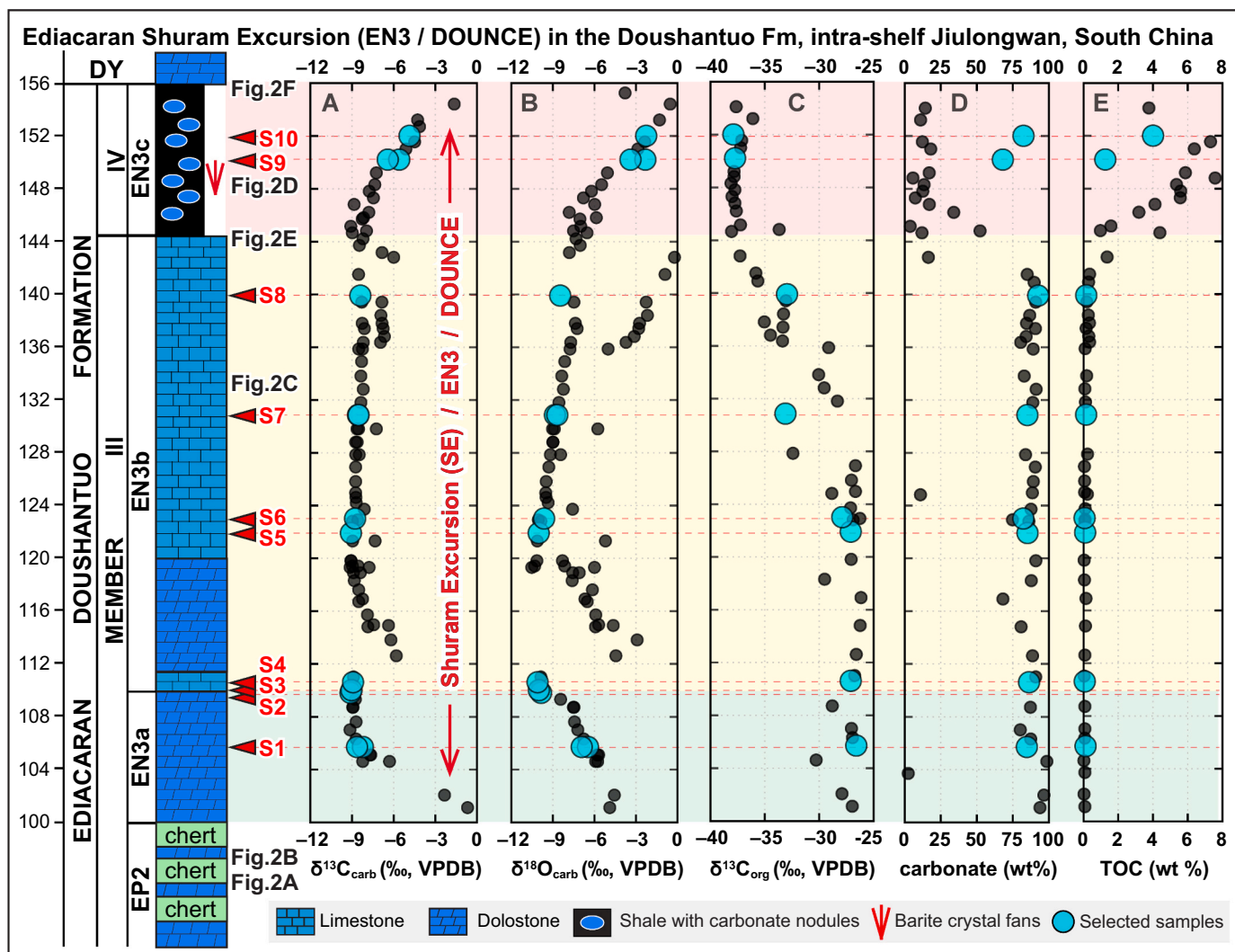
Fig. 3. Integrated chemostratigraphy of the Ediacaran Shuram excursion (i.e., EN3 / DOUNCE interval) in the upper Doushantuo Formation, Jiulongwan section, South China. Cyan circles represent samples investigated in this study, which include bedded dolostones (samples S1–3), bedded dolomitic limestones (samples S4–8), and dolomite nodules (samples S9–10). The chemostratigraphic data include **(A)** $\delta^{13}C_{carb}$ (VPDB, ‰); **(B)** $\delta^{18}O_{carb}$ (VPDB, ‰); **(C)** $\delta^{13}C_{org}$ (VPDB, ‰); **(D)** carbonate content; **(E)** TOC content. The $\delta^{13}C_{carb}$ and $\delta^{18}O_{carb}$ data were analyzed from micro-drilled powders by conventional gas-source isotope ratio mass spectrometer (GS-IRMS). Green, yellow, and red background color correspond to EN3a, EN3b, and EN3c, respectively, defined by McFadden et al. (2008). Data source: (McFadden et al., 2008). Abbreviations: EN = Ediacaran negative excursion; EP = Ediacaran positive excursion; DY = Dengying; TOC = total organic carbon. (For interpretation of the references to color in this figure legend, the reader is referred to the web version of this article.)

$\delta^{13}C_{org}$ data measured on micro-drilled powders by conventional Gas-Source Isotope Ratio Mass Spectrometer (GS-IRMS) have previously been published (Jiang et al., 2007; McFadden et al., 2008; Zhou et al., 2012; Ling et al., 2013) (Table 1). In this study, all ten samples were thoroughly investigated by optical microscopy, as well as CL and SEM imaging (Tables 2, 3). Six samples were analyzed at a μm scale by SIMS for $\delta^{13}C_{carb}$ compositions (Table 3).

3.2. Cathodoluminescence

Cathodoluminescence excitation was achieved with a cold-cathode CITL CL system (Cambridge Image Technology – model Mk5, UK) in the Department of Geology, University of Mons, Belgium. The instrument was operated at 15 kV acceleration voltage, 500 μA beam current, and a current density of about 8 μA/mm². CL images were captured with a Peltier-cooled digital color camera (Lumenera model Infinity 3, Canada) set from 0.1 s to a few seconds exposure time depending on the CL intensity and microscope magnification. Multiple-frame averaging was used to reduce noise. Color calibration of the camera (white balance)

was performed using the blue-filtered, tungsten-halogen light source of the microscope, which may result in CL colors that are slightly different from other equipment (especially around the yellow band, which is narrow), but ensures more or less standardized observation conditions.

3.3. SIMS carbonate carbon isotope analysis

In situ $\delta^{13}C_{carb}$ analysis of both calcite and dolomite was conducted on a CAMECA IMS 1280 at the Wisconsin Secondary Ion Mass Spectrometer (WiscSIMS) Laboratory, Department of Geoscience, University of Wisconsin–Madison. The analyses include two WiscSIMS sessions (2018-01-08 & 2018-02-05). During SIMS analysis, carbon stable isotopes (^{12}C, ^{13}C) were measured with a 7-μm-diameter beam size. These analyses were made using one Faraday cup and two electron multiplier detectors measuring $^{12}C^-$, $^{13}C^-$, and $^{13}C^1H^-$, respectively. The WiscSIMS reference material UWC3 calcite was used as a running standard for both analytical sessions (Fig. A1) (Kozdon et al., 2009; Valley and Kita, 2009; Śliwiński et al., 2016a). Measured ratios of $^{13}C/^{12}C$ were calculated as "raw" δ-values ($\delta^{13}C_{raw}$) before converting to the VPDB
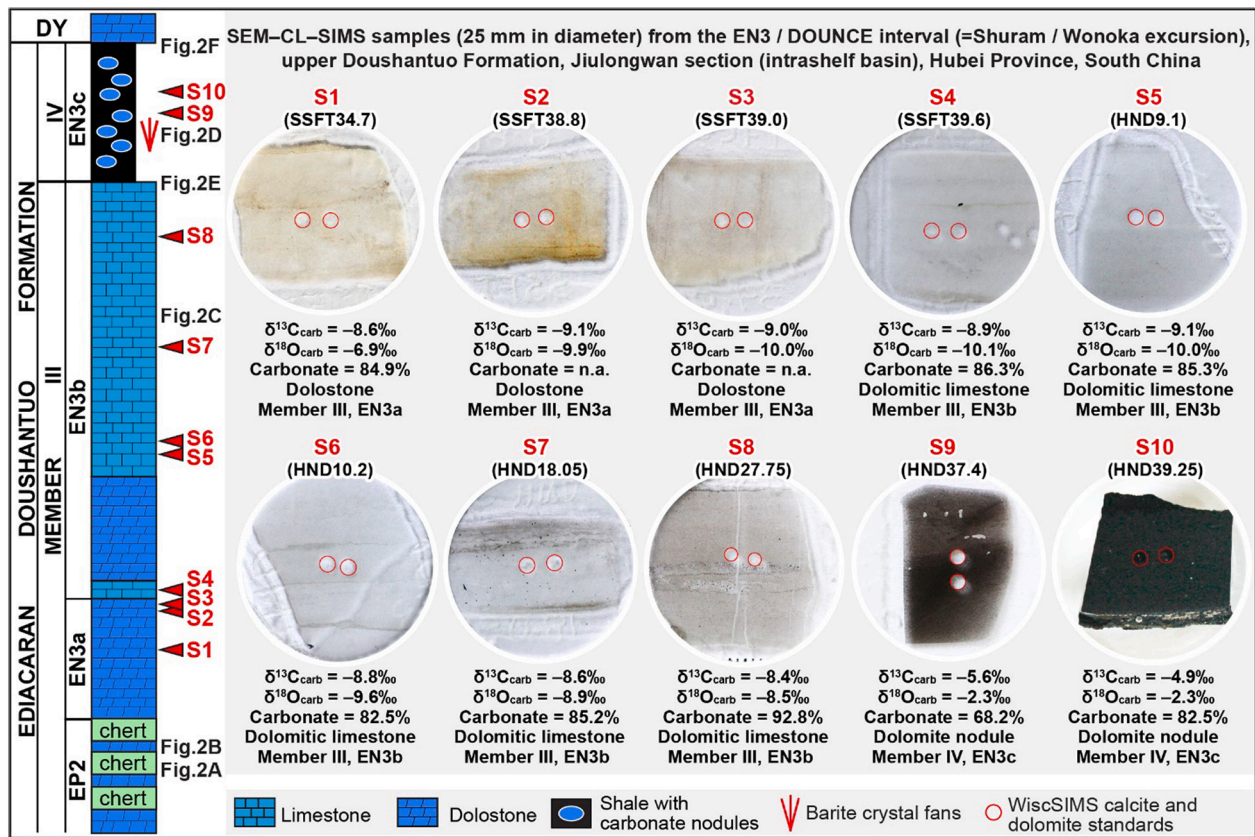
Fig. 4. Ten EN3 samples (S1–10) investigated in this study. Samples S1–9 are glass thin sections; sample S10 is a 5–mm–thick epoxy mount. Each sample is 25 mm in diameter, with WiscSIMS calcite standard UWC3 and dolomite standard UW6220 mounted in the center (red circles). Samples S1, S4–8 were analyzed by SIMS. All samples were investigated by SEM and CL. $\delta^{13}C_{carbonate}$ and $\delta^{18}O_{carbonate}$ data listed in the figure were measured from micro-drilled powders by conventional gas-source isotope ratio mass spectrometer (GS-IRMS). Carbonate content data are also provided when available. Data source: (McFadden et al., 2008). Abbreviations: EN = Ediacaran negative excursion; EP = Ediacaran positive excursion; DY = Dengying; n.a. = not available. (For interpretation of the references to color in this figure legend, the reader is referred to the web version of this article.)

Table 1

Geological context and published GS-IRMS data of the SIMS samples. Samples S1 to S10 (see Fig. 4) are from the EN3 interval of the Doushantuo Formation at the Jiulongwan section (intra-shelf basin), South China. Source of micro-drilled bulk sample data: McFadden et al. (2008). Abbreviations used: GS-IRMS = gas-source isotope ratio mass spectrometry; TOC = total organic carbon; EN = Ediacaran negative excursion.

Samples	Original name (McFadden et al., 2008)	Lithology	Stratigraphic height (m)	Stratigraphic position	Carbonate content (wt%)	$\delta^{13}C_{carb}$ (VPDB, micro-drilled, GS-IRMS)	$\delta^{18}O_{carb}$ (VPDB, micro-drilled, GS-IRMS)	$\delta^{13}C_{org}$ (VPDB, bulk, GS-IRMS)	TOC (wt%)
S1	SSFT-34.7	Dolostone	105.7	EN3a, Mb. III	84.9%	−8.2‰ −8.6‰	−6.5‰ −6.9‰	−26.6‰	0.12%
S2 [#]	SSFT-38.8	Dolostone	109.8	EN3a, Mb. III		−9.1‰	−9.9‰		
S3 [#]	SSFT-39.0	Dolostone	110.0	EN3a, Mb. III		−9.0‰	−10.0‰		
S4	SSFT-39.6	Dolomitic limestone	110.6	EN3b, Mb. III	86.3%	−8.9‰	−10.1‰	−27.1‰	0.07%
S5	HND-9.1	Dolomitic limestone	121.9	EN3b, Mb. III	85.3%	−9.1‰	−10.0‰	−27.1‰	0.09%
S6	HND-10.2	Dolomitic limestone	123.0	EN3b, Mb. III	82.5%	−8.8‰	−9.6‰	−27.9‰	0.06%
S7	HND-18.05	Dolomitic limestone	130.9	EN3b, Mb. III	85.2%	−8.6‰	−8.9‰	−33.1‰	0.15%
S8	HND-27.75	Dolomitic limestone	140.55	EN3b, Mb. III	92.8% *	−8.4‰ *	−8.5‰ *	−33.0‰ *	0.16% *
S9 [#]	HND-37.4	Dolomite nodule	150.2	EN3c, Mb. IV	68.2%	−5.6‰	−2.3‰	−37.7‰	1.25%
S10 [#]	HND-39.25	Dolomite nodule	152.05	EN3c, Mb. IV	82.5%	−4.9‰	−2.3‰	−37.9‰	4.0% (shale)

[#] Not analyzed by SIMS in this study; Detailed SEM-CL images can be found in the online supplementary materials.

* There are no micro-drilled data for sample S8. The value presented in the table was measured from sample HND 27.1, which is stratigraphically 0.6 m below sample S8.

Table 2
Summary of mineralogical, petrographic, and geochemical results of the EN3 samples in this study. More SEM–SIMS–CL and optical microscopic results can be found in the online supplementary materials. Abbreviations: SIMS = secondary ion mass spectrometry; SEM = scanning electron microscopy; CL = cathodoluminescence; EPMA = electron probe microanalysis.

Samples	Lithology	Matrix (average grain size)	Trace mineral (average grain size)	Analyses in this study	SEM–SIMS–CL results
S1	Dolostone	Dolomite (ca. 100 μm)		SIMS/SEM/CL/EPMA	Figs. 6; A5
S2	Dolostone	Dolomite (ca. 100 μm)		SEM/CL	Fig. A6
S3	Dolostone	Dolomite (ca. 100 μm)		SEM/CL	Fig. A7
S4	Dolomitic limestone	Calcite microspar (ca. 5–10 μm)	Zoned, disseminated dolomite (up to 100 μm)	SIMS/SEM/CL/EPMA	Fig. 7; A8
S5	Dolomitic limestone	Calcite microspar (ca. 5–10 μm)	Zoned, disseminated dolomite (up to 100 μm)	SIMS/SEM/CL/EPMA	Figs. 8; A9
S6	Dolomitic limestone	Calcite microspar (ca. 5–10 μm)	Zoned, disseminated dolomite (up to 100 μm); Euhedral dolomite along stylolite (50–100 μm)	SIMS/SEM/CL/EPMA	Figs. 9–10; A10–11
S7	Dolomitic limestone	Calcite microspar (ca. 5–10 μm)	Zoned, disseminated dolomite (up to 100 μm)	SIMS/SEM/CL/EPMA	Figs. 11; A12
S8	Dolomitic limestone	Calcite microspar (ca. 5–10 μm)	Zoned, disseminated dolomite (up to 100 μm); Euhedral dolomite along stylolite (up to 100 μm)	SIMS/SEM/CL/EPMA	Figs. 12; A13
S9	Dolomite nodule	Dolomite (ca. 30 μm)		SEM/CL	Fig. A14
S10	Dolomite nodule	Dolomite (ca. 30 μm)		SEM/CL	Fig. A15

Table 3
A summary of the analyzed SIMS spots. SIMS analyses were grouped in "domains" identified by SEM and CL imaging. In some cases, multiple domains were analyzed on a sample. In these cases, the domains are numbered sequentially and referenced in both the appendix images and supplemental data table. All data can be found in the online supplementary materials (Excel spreadsheets). Original sample numbers of the SIMS samples can be found in McFadden et al. (2008). Abbreviations used: EN = Ediacaran Negative excursion; N.A. = Not analyzed by SIMS; CL = cathodoluminescence; SEM = scanning electron microscope; SIMS = secondary ion mass spectrometry.

EN3 samples	Original sample numbers	Lithology	SIMS domains	WiscSIMS session	SIMS spot ID
S1	SSFT34.7	Dolostone	#1	20180205	@769–781
			#2	20180205	@786–791
S2	SSFT38.8	Dolostone	N.A.	N.A.	N.A.
S3	SSFT39	Dolostone	N.A.	N.A.	N.A.
S4	SSFT39.6	Dolomitic limestone	#1	20180205	@145–168
S5	HND9.1	Dolomitic limestone	#1	20180108	@206–215
S6	HND10.2	Dolomitic limestone	#1	20180205	@676–687
			#2	20180205	@692–703
			#3	20180205	@708–714
			#4	20180205	@715–722
S7	HND18.05	Dolomitic limestone	#1	20180205	@735–746
			#2	20180205	@751–760
S8	HND27.75	Dolomitic limestone	#1	20180205	@415–424
			#1	20180205	@444–447
			#2	20180205	@429–439
			#3	20180205	@448–467
			#4	20180205	@468–482
			#5	20180205	@483–489
S9	HND37.4	Dolostone nodule	N.A.	N.A.	N.A.
S10	HND39.25	Dolostone nodule	N.A.	N.A.	N.A.

scale typically based on eight analyses of UWC3 that bracket each group of 10–15 sample analyses. Carbon isotope ratios are reported in standard per mil (‰) notation relative to VPDB, calculated as $\delta^{13}C_{sample} = [(^{13}C/^{12}C)_{sample} / (^{13}C/^{12}C)_{VPDB} - 1] \times 1000$. The spot-to-spot reproducibility (2SD, 7-μm beam size) of $\delta^{13}C_{carbonate}$ values, calculated from all bracketing analyses on UWC3 in each individual session, is ±0.8‰ for WiscSIMS session 2018-01-08 and ±1.0‰ for WiscSIMS session 2018-02-05. All raw and corrected SIMS data are reported in the online supplementary materials.

Measurements of $^{13}C/^{12}C$ were made using a $^{133}Cs^+$ primary ion beam with an intensity of ~600 pA. The secondary ion intensity of ^{12}C was ~7 × 10^6 cps and was used as a monitor of quality control during analysis. SIMS spots with aberrant count rates (ratio between yield of sample and average yield of bracketing standards: <0.85 or >1.05) were not included in the figures or considered in data interpretation but are listed in the online supplementary materials. In total, 15 data points show abnormal relative yields and are filtered in this study. The remaining 142 SIMS spots ($n = 36$ on calcite, $n = 106$ on dolomite) are further discussed in this study. ^{13}CH was analyzed simultaneously with ^{13}C and ^{12}C also as a quality control to evaluate the effect of hydrogen on SIMS analysis, which might be related to the presence of organic matter or water as discussed in previous carbonate SIMS studies (Denny et al., 2017; Wycech et al., 2018). An electron flood gun in combination with a gold coating (~40 nm) was used for charge compensation. The total analytical time per spot was about 4 min including pre-sputtering (20 s), automatic centering of the secondary ion beam in the field aperture (60 s), and analysis (160 s). The baseline noise level of the Faraday cups was monitored during pre-sputtering.

After SIMS analysis, Fe concentration (Fe# = molar ratio of Fe/[Fe + Mg]) adjacent to each SIMS pit was measured by EPMA to correct the composition-specific instrumental mass fractionation (IMF or bias) of each SIMS $\delta^{13}C_{carb}$ analysis. Typically, for the correction of each raw SIMS $\delta^{13}C_{carb}$ value, an averaged Fe# value was calculated based on the elemental concentration data of two or three EPMA spots that are close to the corresponding SIMS pit. Although constraining the underlying controls on IMF is challenging, it has been found that raw $\delta^{13}C_{carb}$ data obtained by SIMS could be biased by IMFs that vary in magnitude depending on instrumental conditions, mineralogy, and sample composition (Valley and Kita, 2009; Śliwiński et al., 2016a). To address the effect of Fe/Mg on IMF, a suite of standards along the dolomite–ankerite series were analyzed at the beginning of each session and used to generate a calibration curve relative to the dolomite standard UW6220 (Fig. A2) (Śliwiński et al., 2016a). The calibration curve was used to determine the composition-specific IMF and to correct the $\delta^{13}C$ value for each SIMS pit (see online Excel File: SIMS data spreadsheet). As discussed in detail by Śliwiński et al. (2016a), the empirical calibration of IMF for Ca–Mg–Fe carbonates varies with session-specific instrument tuning and running conditions. Therefore, as applied elsewhere (Denny et al., 2020), different IMF vs. Fe# curves were calibrated in each session to correct $\delta^{13}C_{carb}$ data (Fig. A2). EPMA data show that the EN3 calcite is very low in Fe, Mn, and Mg concentration, with average values of FeCO₃ mol% = 0.17, MnCO₃ mol% = 0.01, MgCO₃ mol % = 1.18 ($n = 36$, Table 4). Therefore, the SIMS $\delta^{13}C_{calcite}$ data analyzed from EN3 were corrected for IMF using data from UWC3 and only SIMS $\delta^{13}C_{dolomite}$ data were corrected for matrix effects due to Mg-Fe solid solution. All raw and

Table 4
SIMS and EPMA data of calcite from the EN3 interval, Doushantuo Formation, Jiulongwan, Hubei Province, South China. Each analyzed SIMS pit has a unique spot ID that can be retrieved in the online supplementary materials. Elemental concentration data of each SIMS pit were obtained based on the EPMA analyses of two or three spots that are close to the SIMS pit. An averaged Fe# value = [molar ratio of Fe/(Fe + Mg)] of two or three EMPA spots closely associated with each SIMS pit was used for the $\delta^{13}C_{carb}$ correction of each SIMS pit. Value 0.00 represents concentration under detect limit.

Sample	Mineralogy	SIMS domain	SIMS spot code	SIMS $\delta^{13}C$ [‰, VPDB]	2SD [‰]	Fe#	$MnCO_3$ [mol%]	$FeCO_3$ [mol%]	$MgCO_3$ [mol%]	$CaCO_3$ [mol%]
S4	Calcite	#1	20180205@152	–7.8	1.1	0.03	0.00	0.04	1.30	98.65
S4	Calcite	#1	20180205@153	–7.9	1.1					
S4	Calcite	#1	20180205@161	–8.4	1.3	0.05	0.00	0.06	1.27	98.67
S4	Calcite	#1	20180205@164	–8.7	1.3	0.02	0.00	0.03	1.10	98.87
S4	Calcite	#1	20180205@168	–7.8	1.3	0.03	0.00	0.04	1.23	98.73
S5	Calcite	#1	20180108@212	–8.6	0.8	0.12	0.00	0.26	1.38	98.36
S5	Calcite	#1	20180108@213	–8.8	0.8	0.12	0.01	0.16	1.20	98.63
S5	Calcite	#1	20180108@214	–8.7	0.8	0.14	0.00	0.20	1.19	98.61
S5	Calcite	#1	20180108@215	–9.3	0.8	0.05	0.00	0.07	1.20	98.73
S6	Calcite	#1	20180205@679	–9.0	0.6					
S6	Calcite	#1	20180205@682	–9.1	0.6	0.03	0.00	0.03	0.89	99.08
S6	Calcite	#1	20180205@686	–8.4	0.6	0.14	0.02	0.23	1.45	98.30
S6	Calcite	#1	20180205@687	–8.2	0.6					
S6	Calcite	#2	20180205@696	–6.9	0.7	0.03	0.01	0.09	2.06	97.85
S6	Calcite	#2	20180205@701	–8.3	0.7	0.09	0.00	0.12	1.33	98.54
S6	Calcite	#2	20180205@703	–7.7	0.7	0.20	0.00	0.59	2.31	97.11
S6	Calcite	#3	20180205@710	–7.0	1.1					
S6	Calcite	#3	20180205@711	–7.8	1.1					
S6	Calcite	#3	20180205@713	–8.6	1.1	0.04	0.01	0.04	1.03	98.92
S6	Calcite	#3	20180205@714	–8.4	1.1	0.02	0.01	0.02	0.85	99.13
S6	Calcite	#4	20180205@722	–8.6	1.1	0.03	0.11	0.04	1.17	98.67
S7	Calcite	#1	20180205@737	–8.4	1.0	0.26	0.00	0.45	1.24	98.30
S7	Calcite	#1	20180205@741	–9.5	1.0	0.34	0.01	0.92	1.72	97.36
S7	Calcite	#1	20180205@744	–7.0	1.0	0.27	0.00	0.33	0.94	98.73
S7	Calcite	#1	20180205@745	–8.6	1.0	0.36	0.00	0.70	0.99	98.31
S7	Calcite	#2	20180205@758	–8.2	0.9	0.17	0.03	0.25	1.24	98.48
S7	Calcite	#2	20180205@759	–8.7	0.9	0.07	0.00	0.10	1.39	98.51
S8	Calcite	#2	20180205@437	–7.6	1.0	0.03	0.00	0.03	0.75	99.22
S8	Calcite	#1	20180205@445	–7.7	0.9	0.01	0.00	0.01	0.75	99.24
S8	Calcite	#1	20180205@446	–8.6	0.9	0.02	0.01	0.03	1.22	98.74
S8	Calcite	#1	20180205@447	–9.0	0.9	0.01	0.02	0.00	0.80	99.18
S8	Calcite	#4	20180205@478	–8.8	1.0	0.00	0.01	0.00	0.71	99.28
S8	Calcite	#4	20180205@479	–8.7	1.0	0.04	0.00	0.03	0.79	99.18
S8	Calcite	#4	20180205@480	–8.4	1.0	0.04	0.00	0.03	0.66	99.31
S8	Calcite	#5	20180205@483	–6.9	1.0					
S8	Calcite	#5	20180205@484	–6.2	1.0					

corrected SIMS data, EPMA data, and quality control methods are reported in the online supplementary materials.

3.4. Scanning electron microscope

After SIMS analysis, the gold coating was removed and replaced with an iridium coat for Scanning Electron Microscope (SEM) imaging in the Ray and Mary Wilcox SEM Laboratory, Department of Geoscience, University of Wisconsin–Madison. BSE images of samples were acquired with a Hitachi S3400 VP SEM with EDS using a Thermo Fisher thin window detector. Each pit was investigated by SEM for possible irregularities. SEM images were acquired using an accelerating voltage of 15 keV or 20 keV at a working distance of 10 mm. All the SIMS pits were imaged by SEM and are shown with corresponding $\delta^{13}C_{carb}$ values in the online supplementary materials.

3.5. Electron probe microanalysis

EPMA was performed on the CAMECA SX–51 at the Cameron Electron Microprobe Laboratory at the University of Wisconsin–Madison. Data were collected with a ~120 s analysis time and a 15 keV, 20 nA beam, which was defocused to a 5 μm diameter in an attempt to minimize sample damage. Data were processed using EPMA software (Donovan et al., 2018), and background correction was performed with the Mean Atomic Number procedure (Donovan and Tingle, 1996). As changes over time in measured intensities are common for EPMA measurements in carbonates, particularly for the element Ca, a self-fitted

time-dependent intensity correction was applied for all elements (Donovan et al., 2018). CO_2 was added for the matrix correction, based upon the appropriate C:O ratio, with oxygen determined by stoichiometry to the cations. The matrix correction used was PAP, with Henke mass absorption coefficients. Standards used were Delight Dolomite (Mg), Callender Calcite (Ca), siderite (Fe), rhodochrosite (Mn) and strontianite (Sr). Samples and standards were coated with ~200 Å carbon. WDS X–ray intensities were acquired with EPMA software, with mean atomic number backgrounds and with the PAP matrix correction, iterated within the matrix correction.

4. Results

4.1. Petrographic observations

The ten investigated samples from the EN3 interval show three different lithologies: bedded dolostones (samples S1–3), bedded dolomitic limestones (S4–8), and dolomite nodules (S9–10) (Fig. 4; Table 1). A detailed compilation of petrographic images of all ten samples can be found in the online supplemental materials. Here we summarize the main features in Table 2 and below.

Dolomite (samples S1–3; Figs. 6, A5–7). — Bedded dolostone samples show pervasive subhedral to euhedral dolomite crystals of ca. 100 μm in size. Dolomite in the EN3 dolostone samples typically have a dull CL color (Figs. 6C, F, A4A).

Dolomitic limestones (samples S4–8; Figs. 7–12, A8–13). — Bedded dolomitic limestones show distinct interlocking calcite microspar (ca.

5–10 μm in size) as the matrix under SEM (e.g., Fig. A13J–L). Large dolomite crystals (up to 100 μm) are disseminated in the calcite matrix or occur in patches, many of which show either sharp straight boundaries (Fig. 12) or irregular boundaries (Fig. A10) with surrounding calcite. Euhedral dolomite crystals have also been found concentrated along stylolites in some samples (Fig. A11). Both types of dolomite crystals show clear zoning under BSE and CL. Zonation of dolomite crystals typically shows complementary brightness under BSE and CL: darker BSE zones (lower Fe) correspond to brighter CL zones, and vice versa (Fig. A4B–F).

Dolomite nodules (samples S9–10; Figs. A14–15). — Dolomite nodules largely consist of euhedral to subhedral dolomite crystals of ca. 30 μm in size, and typically show weak zoning under BSE and CL (Fig. A15I).

4.2. SIMS $\delta^{13}C_{carb}$ and EPMA data

The calcite standard UWC3 was analyzed repeatedly, before and after the measurement of every 10 to 15 unknown spots on EN3 carbonates in order to closely monitor run conditions. A total of 244 measurements were conducted by SIMS in the course of two sessions, including 102 spots on UWC3 (Fig. A1), 36 spots on EN3 calcite (Fig. A1; Table 4), and 106 spots on EN3 dolomite (Fig. A1; Table 5). The $\delta^{13}C_{raw}$ values of UWC3 are highly consistent throughout the two WiscSIMS sessions, suggesting stable instrumental conditions (Fig. A1).

Data with anomalous primary beam intensities and ion yields were filtered before raw data correction (see online supplementary materials). The corrected SIMS data show that $\delta^{13}C_{calcite}$ ranges from −9.5 to −6.2‰ VPDB (mean value −8.3‰, n = 36) and $\delta^{13}C_{dolomite}$ from −11.2 to −3.8‰ (mean value −7.8‰, n = 95) (Table 6). A comparison between micro-drilled bulk-sample data (McFadden et al., 2008) and the new data in this study shows a much wider range of SIMS $\delta^{13}C$ values than of micro-drilled $\delta^{13}C$ values (Fig. 5A). SIMS dolomite $\delta^{13}C$ data generally show a wider range and larger variability than SIMS calcite $\delta^{13}C$ values (Fig. 5; Table 6). The mean values of the SIMS $\delta^{13}C_{dolomite}$ and $\delta^{13}C_{calcite}$ data are statistically indistinguishable within uncertainty for each sample and are consistent with the previously published $\delta^{13}C_{micro-drilled}$ data (Table 1) acquired from micro-drilled powders of the same samples (Fig. 5; Table 6). Thus, it appears that the GS-IRMS analysis of powders has homogenized fine-scale variability that can only be revealed by SIMS.

Cross plots of $\delta^{13}C$ compositions vs. $FeCO_3$, $MnCO_3$, $MgCO_3$ abundances show no clear correlation (Fig. A3). The values of SIMS $\delta^{13}C$ IMF, however, reveal an overall negative correlation with Fe# or $FeCO_3$ (Fig. A3C, F), which is consistent with the calibration curve established at the beginning of each SIMS session (Fig. A2).

5. Discussions

5.1. Paragenesis

Because the dolomitic limestone samples in the EN3 interval at the Jiulongwan section contain discrete phases of both calcite and dolomite under SEM, an independent assessment on the paragenesis of these two phases is critical before interpreting the SIMS $\delta^{13}C$ data. The interlocking mosaics of calcite microspar are characteristic of neomorphosed micrite (e.g., Fig. A13J–L). Zoned dolomite crystals with grain sizes up to ca. 100 μm are disseminated in the calcite matrix. The otherwise euhedral dolomite crystals often show irregular boundaries with surrounding calcite microspar (Fig. A10). After the deposition of micrite, two potential paragenetic scenarios seem possible to explain the textural relationships between the calcite microspar and zoned dolomite, which are presented below.

First, the irregular boundaries between calcite and dolomite could be interpreted as zoned dolomite crystals being partially replaced by calcite microspar. In this scenario, dolomite crystals predate calcite microspar.

If this scenario is correct, it means that, prior to the replacement of dolomite, the whole dolomitic limestone rock was originally full of large, euhedral, and zoned dolomite crystals. However, considering that the calcite microspar is uniformly fine grained (5–10 μm), the dolomite rhombs are relatively rare, and there is no obvious evidence for massive diagenetic alteration (e.g., late veins, significant dissolution, replacement, or recrystallization), we regard that the sample did not experience significant dolomitization before the formation of calcite microspar. Therefore, this scenario (i.e., wholesale dolomitization before the formation of calcite microspar) is not favored in this study.

The second possible scenario is that dolomitization occurred along irregular substrates of preexisting calcite microspar. In this scenario, disseminated dolomite crystals in the EN3 limestone samples postdate calcite microspar. In other words, the SEM images of those dolomitic limestone samples represent snapshots of ongoing dolomitization of the calcite-dominated limestone rock. Based on the indistinguishable mean values of the SIMS $\delta^{13}C_{calcite}$ and $\delta^{13}C_{dolomite}$ data in each individual sample (Fig. 5; Table 6), dolomitization should have occurred in an overall sediment-buffered diagenetic system with respect to $\delta^{13}C$ (i.e., diagenesis without significantly changing the overall $\delta^{13}C$ of carbonate sediments).

The timing of dolomitization of the EN3 limestone samples is still not well constrained, either early or late. Notably, a recent clumped isotope study on the Doushantuo Formation at the inner shelf Zhangcunping location demonstrates that early dolomitization could occur near the sediment-water interface of the Ediacaran ocean (Chang et al., 2020). In that case, the Doushantuo dolomite crystals in Chang et al. (2020)'s samples are uniformly fine-grained dolomicrite (mostly ca. 10–20 μm) with spherical or ellipsoidal shapes. In contrast, the dolomite crystals in our EN3 limestone samples are mostly much larger in size (up to ca. 100 μm) and often show irregular margins and clear compositional zonation under CL and SEM (Fig. A4), which likely formed via postdepositional dolomitization, rather than near the sediment-water interface during early diagenesis.

In summary, SEM observation shows that the EN3 samples at Jiulongwan have been subjected to different degrees of dolomitization. The dolostones in the EN3a interval (Figs. A5–7) and dolomite nodules in the EN3c interval (Figs. A14–15) show pervasive dolomite crystals with weak zoning, whereas the limestone samples in the EN3b interval contain zoned dolomite crystals that are either disseminated in the calcite matrix or occur in patches (Figs. A8–13). Some dolomite crystals were also found along stylolites (Figs. A11). Although the precise timing of dolomitization is still not well constrained, a post-depositional dolomitization in a sediment-buffered diagenetic system with respect to $\delta^{13}C$ is preferred in this study.

5.2. Evaluating post-depositional origins for the Shuram excursion

Our detailed petrographic investigation of the EN3 samples allows for a direct test of previously published hypotheses that advocate depositional or diagenetic origins for the SE. It has been suggested that the SE may result from massive fluid-buffered alterations during meteoric and mixing-zone diagenesis (Knauth and Kennedy, 2009; Zhao et al., 2020) or late burial diagenesis (Derry, 2010). Those hypotheses were proposed purely based on geochemical modelling, without any petrographic evidence. If these hypothesized post-depositional processes indeed played a role, there should be a textural signature imparted on the samples.

Different types of post-depositional diagenesis can leave distinct petrographic traces (Tucker and Bathurst, 1990; Scholle and Ulmer-Scholle, 2003; Tucker et al., 2009). For example, meteoric and mixing-zone diagenesis typically leads to extensive dissolution of preexisting carbonates and the precipitation of pendant/gravitational cement, needle-fiber cement, isopachous rims, and/or pore fillings of equant calcite (Allan and Matthews, 1982; Tucker and Bathurst, 1990; Kim and Lee, 2003; Scholle and Ulmer-Scholle, 2003; Tucker et al.,

Table 5

SIMS and EPMA data of dolomite from the EN3 interval, Doushantuo Formation, Jiulongwan, Hubei Province, South China. Each analyzed SIMS pit has a unique spot ID that can be retrieved in the online supplementary materials. Elemental concentration data of each SIMS pit were obtained based on the EPMA analyses of two or three spots that are close to the SIMS pit. An averaged Fe# value = [molar ratio of Fe/(Fe + Mg)] of two or three EMPA spots closely associated with each SIMS pit was used for the $\delta^{13}C_{carb}$ correction of each SIMS pit. Value 0.00 represents concentration under detect limit.

Sample	Mineralogy	SIMS domain	SIMS spot code	SIMS $\delta^{13}C$ [‰, VPDB]	2SD [‰]	Fe#	$MnCO_3$ [mol%]	$FeCO_3$ [mol%]	$MgCO_3$ [mol%]	$CaCO_3$ [mol%]
S1	Dolomite	#1	20180205@769	−7.3	1.0	0.02	0.01	0.91	47.15	51.93
S1	Dolomite	#1	20180205@771	−9.4	1.0	0.02	0.02	0.82	46.30	52.86
S1	Dolomite	#1	20180205@772	−8.2	1.0	0.02	0.00	0.82	46.88	52.30
S1	Dolomite	#1	20180205@774	−9.1	1.0	0.02	0.01	0.82	47.95	51.22
S1	Dolomite	#1	20180205@775	−9.0	1.0	0.02	0.04	0.83	46.79	52.35
S1	Dolomite	#1	20180205@776	−8.8	1.0	0.02	0.00	0.90	47.60	51.50
S1	Dolomite	#1	20180205@777	−9.4	1.0	0.02	0.02	0.80	46.02	53.16
S1	Dolomite	#1	20180205@779	−11.2	1.0	0.02	0.01	0.80	46.44	52.76
S1	Dolomite	#1	20180205@780	−9.5	1.0	0.02	0.04	0.85	46.55	52.56
S1	Dolomite	#2	20180205@786	−9.4	0.8	0.02	0.01	0.73	46.46	52.80
S1	Dolomite	#2	20180205@787	−10.5	0.8	0.02	0.03	0.88	46.59	52.50
S1	Dolomite	#2	20180205@788	−8.9	0.8	0.02	0.00	0.94	47.09	51.97
S1	Dolomite	#2	20180205@789	−7.7	0.8	0.02	0.02	0.77	46.54	52.67
S1	Dolomite	#2	20180205@790	−9.2	0.8	0.02	0.01	0.77	46.56	52.66
S1	Dolomite	#2	20180205@791	−7.7	0.8	0.02	0.02	0.80	46.84	52.34
S4	Dolomite	#1	20180205@145	−6.9	1.1	0.07	0.00	2.77	38.35	58.89
S4	Dolomite	#1	20180205@146	−9.9	1.1	0.01	0.01	0.26	42.04	57.70
S4	Dolomite	#1	20180205@147	−9.8	1.1	0.01	0.04	0.38	41.51	58.08
S4	Dolomite	#1	20180205@148	−7.3	1.1	0.04	0.00	1.62	40.65	57.73
S4	Dolomite	#1	20180205@149	−5.8	1.1	0.06	0.00	2.53	40.07	57.40
S4	Dolomite	#1	20180205@151	−8.5	1.1	0.02	0.00	0.93	38.98	60.09
S4	Dolomite	#1	20180205@154	−8.7	1.1	0.05	0.01	2.31	39.78	57.91
S4	Dolomite	#1	20180205@159	−10.4	1.3	0.01	0.02	0.40	41.22	58.36
S4	Dolomite	#1	20180205@160	−8.5	1.3	0.01	0.03	0.50	41.34	58.13
S4	Dolomite	#1	20180205@162	−8.8	1.3	0.05	0.02	2.10	40.72	57.15
S4	Dolomite	#1	20180205@163	−8.9	1.3	0.06	0.01	2.35	40.13	57.52
S4	Dolomite	#1	20180205@165	−9.1	1.3	0.06	0.00	2.53	39.57	57.90
S4	Dolomite	#1	20180205@166	−9.7	1.3	0.03	0.00	1.44	40.45	58.11
S4	Dolomite	#1	20180205@167	−8.2	1.3	0.05	0.00	1.91	41.03	57.05
S5	Dolomite	#1	20180108@206	−8.6	0.8	0.05	0.00	1.96	40.58	57.46
S5	Dolomite	#1	20180108@207	−8.8	0.8	0.06	0.01	2.65	39.91	57.43
S5	Dolomite	#1	20180108@208	−8.1	0.8	0.05	0.00	2.05	40.83	57.12
S5	Dolomite	#1	20180108@209	−6.4	0.8	0.06	0.00	2.47	39.36	58.17
S5	Dolomite	#1	20180108@210	−10.1	0.8	0.03	0.01	1.07	40.95	57.97
S5	Dolomite	#1	20180108@211	−7.9	0.8	0.07	0.03	2.81	40.04	57.13
S6	Dolomite	#1	20180205@677	−9.3	0.6	0.03	0.00	1.47	40.75	57.78
S6	Dolomite	#1	20180205@678	−8.0	0.6	0.03	0.00	1.47	40.75	57.78
S6	Dolomite	#1	20180205@680	−5.6	0.6	0.09	0.00	3.50	37.45	59.06
S6	Dolomite	#1	20180205@683	−7.5	0.6	0.04	0.00	1.47	40.40	58.14
S6	Dolomite	#1	20180205@684	−9.4	0.6	0.08	0.00	3.41	37.24	59.35
S6	Dolomite	#1	20180205@685	−8.2	0.6	0.08	0.00	3.30	38.67	58.03
S6	Dolomite	#2	20180205@694	−5.8	0.7	0.04	0.04	1.38	36.05	62.53
S6	Dolomite	#2	20180205@699	−6.4	0.7	0.04	0.04	1.38	36.05	62.53
S6	Dolomite	#2	20180205@702	−9.3	0.7	0.05	0.06	2.22	38.76	58.96
S6	Dolomite	#3	20180205@708	−6.5	1.1	0.06	0.00	2.52	41.10	56.38
S6	Dolomite	#3	20180205@712	−9.4	1.1	0.06	0.01	2.76	40.90	56.33
S6	Dolomite	#4	20180205@715	−6.3	1.1	0.02	0.01	0.72	42.24	57.04
S6	Dolomite	#4	20180205@716	−4.1	1.1	0.09	0.01	3.70	39.33	56.95
S6	Dolomite	#4	20180205@717	−7.3	1.1	0.01	0.00	0.63	42.54	56.82
S6	Dolomite	#4	20180205@718	−6.0	1.1	0.04	0.01	1.85	41.22	56.91
S6	Dolomite	#4	20180205@719	−6.8	1.1	0.04	0.04	2.05	44.42	53.49
S6	Dolomite	#4	20180205@720	−6.7	1.1	0.01	0.00	0.62	43.14	56.24
S6	Dolomite	#4	20180205@721	−5.8	1.1	0.07	0.04	3.09	40.37	56.50
S7	Dolomite	#1	20180205@735	−8.6	1.0	0.13	0.01	5.59	37.10	57.30
S7	Dolomite	#1	20180205@736	−7.5	1.0	0.14	0.01	5.88	36.29	57.82
S7	Dolomite	#1	20180205@738	−8.3	1.0	0.13	0.00	5.64	36.27	58.09
S7	Dolomite	#1	20180205@739	−9.4	1.0	0.11	0.00	4.96	38.37	56.67
S7	Dolomite	#1	20180205@740	−6.9	1.0	0.06	0.00	2.57	41.25	56.18
S7	Dolomite	#1	20180205@742	−8.0	1.0	0.14	0.03	5.99	36.64	57.34
S7	Dolomite	#1	20180205@743	−8.6	1.0	0.13	0.01	5.28	36.64	58.08
S7	Dolomite	#1	20180205@746	−8.1	1.0	0.14	0.03	6.07	36.69	57.21
S7	Dolomite	#2	20180205@751	−6.8	0.9	0.05	0.00	1.94	40.34	57.72
S7	Dolomite	#2	20180205@752	−7.4	0.9	0.04	0.00	1.89	40.66	57.44
S7	Dolomite	#2	20180205@753	−9.5	0.9	0.12	0.00	5.49	38.81	55.69
S7	Dolomite	#2	20180205@754	−8.1	0.9	0.12	0.00	5.12	37.05	57.83
S7	Dolomite	#2	20180205@755	−7.1	0.9	0.04	0.02	1.84	40.88	57.26
S7	Dolomite	#2	20180205@756	−8.3	0.9	0.11	0.00	4.46	37.26	58.28
S8	Dolomite	#1	20180205@415	−8.5	1.0	0.01	0.00	0.42	42.32	57.26
S8	Dolomite	#1	20180205@416	−8.7	1.0	0.00	0.00	0.00	43.03	56.97
S8	Dolomite	#1	20180205@417	−6.3	1.0	0.00	0.02	0.01	43.02	56.94

Table 5 (*continued*)

Sample	Mineralogy	SIMS domain	SIMS spot code	SIMS δ¹³C [‰, VPDB]	2SD [‰]	Fe#	MnCO₃ [mol%]	FeCO₃ [mol%]	MgCO₃ [mol%]	CaCO₃ [mol%]
S8	Dolomite	#1	20180205@418	−5.6	1.0	0.00	0.03	0.00	42.67	57.31
S8	Dolomite	#1	20180205@419	−5.8	1.0	0.00	0.01	0.00	42.48	57.51
S8	Dolomite	#1	20180205@420	−9.4	1.0	0.01	0.01	0.34	43.31	56.34
S8	Dolomite	#1	20180205@421	−10.2	1.0	0.01	0.00	0.52	42.06	57.42
S8	Dolomite	#1	20180205@422	−6.1	1.0	0.00	0.01	0.01	42.65	57.32
S8	Dolomite	#1	20180205@423	−8.5	1.0	0.01	0.03	0.26	42.81	56.90
S8	Dolomite	#1	20180205@424	−8.7	1.0	0.01	0.06	0.34	43.63	55.96
S8	Dolomite	#2	20180205@429	−7.9	1.0	0.01	0.01	0.65	43.49	55.85
S8	Dolomite	#2	20180205@430	−8.9	1.0	0.02	0.03	0.93	43.80	55.24
S8	Dolomite	#2	20180205@431	−6.7	1.0	0.02	0.00	1.03	42.65	56.33
S8	Dolomite	#2	20180205@432	−6.6	1.0	0.00	0.01	0.00	44.41	55.58
S8	Dolomite	#2	20180205@433	−6.8	1.0	0.00	0.00	0.01	44.50	55.49
S8	Dolomite	#2	20180205@434	−7.2	1.0	0.00	0.00	0.21	44.39	55.40
S8	Dolomite	#2	20180205@435	−6.1	1.0	0.00	0.01	0.00	43.77	56.22
S8	Dolomite	#2	20180205@436	−9.2	1.0	0.01	0.00	0.41	43.99	55.60
S8	Dolomite	#3	20180205@448	−5.7	0.9	0.00	0.03	0.10	42.22	57.65
S8	Dolomite	#3	20180205@449	−6.8	0.9	0.00	0.02	0.16	43.95	55.87
S8	Dolomite	#3	20180205@450	−6.9	0.9	0.00	0.00	0.00	42.95	57.05
S8	Dolomite	#3	20180205@451	−6.4	0.9	0.01	0.01	0.22	41.80	57.97
S8	Dolomite	#3	20180205@452	−5.8	0.9	0.00	0.00	0.13	42.64	57.22
S8	Dolomite	#3	20180205@453	−5.9	0.9	0.00	0.01	0.08	43.17	56.74
S8	Dolomite	#3	20180205@454	−10.5	0.9	0.00	0.00	0.03	43.42	56.55
S8	Dolomite	#3	20180205@460	−8.7	1.1	0.00	0.01	0.00	42.30	57.69
S8	Dolomite	#3	20180205@461	−6.5	1.1	0.00	0.00	0.13	42.78	57.09
S8	Dolomite	#3	20180205@462	−6.0	1.1	0.00	0.00	0.00	42.68	57.32
S8	Dolomite	#3	20180205@463	−8.7	1.1	0.00	0.01	0.08	41.75	58.16
S8	Dolomite	#3	20180205@464	−3.8	1.1	0.00	0.00	0.09	41.11	58.80
S8	Dolomite	#3	20180205@465	−6.2	1.1	0.00	0.00	0.04	41.94	58.03
S8	Dolomite	#3	20180205@467	−8.7	1.1	0.00	0.01	0.10	42.74	57.14
S8	Dolomite	#4	20180205@468	−7.6	1.1	0.00	0.00	0.10	42.91	57.00
S8	Dolomite	#4	20180205@469	−7.4	1.1	0.00	0.01	0.12	43.04	56.83
S8	Dolomite	#4	20180205@470	−9.4	1.1	0.00	0.00	0.13	43.43	56.44
S8	Dolomite	#4	20180205@471	−5.8	1.1	0.00	0.03	0.21	43.14	56.62
S8	Dolomite	#4	20180205@477	−6.8	1.0	0.00	0.00	0.14	43.08	56.78
S8	Dolomite	#4	20180205@481	−6.6	1.0	0.01	0.00	0.32	42.45	57.22
S8	Dolomite	#4	20180205@482	−7.7	1.0	0.01	0.03	0.43	43.01	56.53

Table 6

Summary of SIMS δ¹³C data. Micro-drilled powders were collected with ca. 800-μm drill holes (McFadden et al., 2008), whereas SIMS analyses were conducted with a ca. 7-μm beam size in this study. Data source: SIMS data (this study); micro-drilled bulk-sample data (McFadden et al., 2008).

SIMS sample	Original code	Lithology	Total SIMS analyses (N)	Calcite δ¹³C [‰, VPDB, SIMS]			Dolomite δ¹³C [‰, VPDB, SIMS]			Bulk sample δ¹³C [‰, VPDB, micro-drilled]
				Mean	2SD	n	Mean	2SD	n	
S1	SSFT34.7	Dolostone	15				−9.0	2.0	15	−8.2; −8.6
S4	SSFT39.6	Dolomitic limestone	19	−8.1	0.8	5	−8.6	2.5	14	−8.9
S5	HND9.1	Dolomitic limestone	10	−8.8	0.6	4	−8.3	2.4	6	−9.1
S6	HND10.2	Dolomitic limestone	30	−8.2	1.4	12	−7.1	3.1	18	−8.8
S7	HND18.05	Dolomitic limestone	20	−8.4	1.7	6	−8.1	1.7	14	−8.6
S8	HND27.75	Dolomitic limestone	48	−8.0	2.0	9	−7.3	3.0	39	−8.4*
SUM			127			36			91	

* There are no micro-drilled data for sample S8. The value presented in the table was measured from sample HND 27.1, which is stratigraphically 0.6 m below sample S8.

2009; Bishop et al., 2014). Late burial diagenesis is typically evidenced by widespread recrystallization and replacement, crosscutting veins, overgrowth of earlier cement crusts, equant calcite mosaics, blocky calcite spar, and/or saddle dolomite (Tucker and Bathurst, 1990; Scholle and Ulmer-Scholle, 2003; Davies and Smith Jr, 2006; Tucker et al., 2009; Barale et al., 2016; Biehl et al., 2016; Jiang et al., 2016; Feng et al., 2017; Hu et al., 2020; Koeshidayatullah et al., 2020). The above-mentioned features can be used as criteria to test whether these different types of diagenesis occurred or not; and if indeed they occurred, the effect of these diagenetic processes on the SE could also be evaluated.

Here, detailed petrographic observations in this study (Figs. 6–12; see more detailed results in the online supplementary materials) reveal no textural supporting evidence for the previously hypothesized meteoric and mixing-zone diagenesis (Knauth and Kennedy, 2009; Zhao et al., 2020) and wholesale late burial diagenesis (Derry, 2010). There is no clear evidence for massive dissolution and replacement — which are typical characteristics of meteoric or deep burial diagenesis — in the EN3 interval. Rather, the EN3 limestone samples contain only minor dolomite rhombs and few stylolites (Figs. A11), and thus appear to be overall well preserved. Dolostones in the lower EN3 suggest that the samples that define the trend to more negative values at the onset of the SE were dolomitized, but this process appears not to have reset depositional carbon isotope values. Therefore, we regard that post-depositional processes played a limited role in altering the δ¹³C signals of the EN3 samples; hence, we focus our discussion on a depositional origin for the SE (see discussion in the next section).

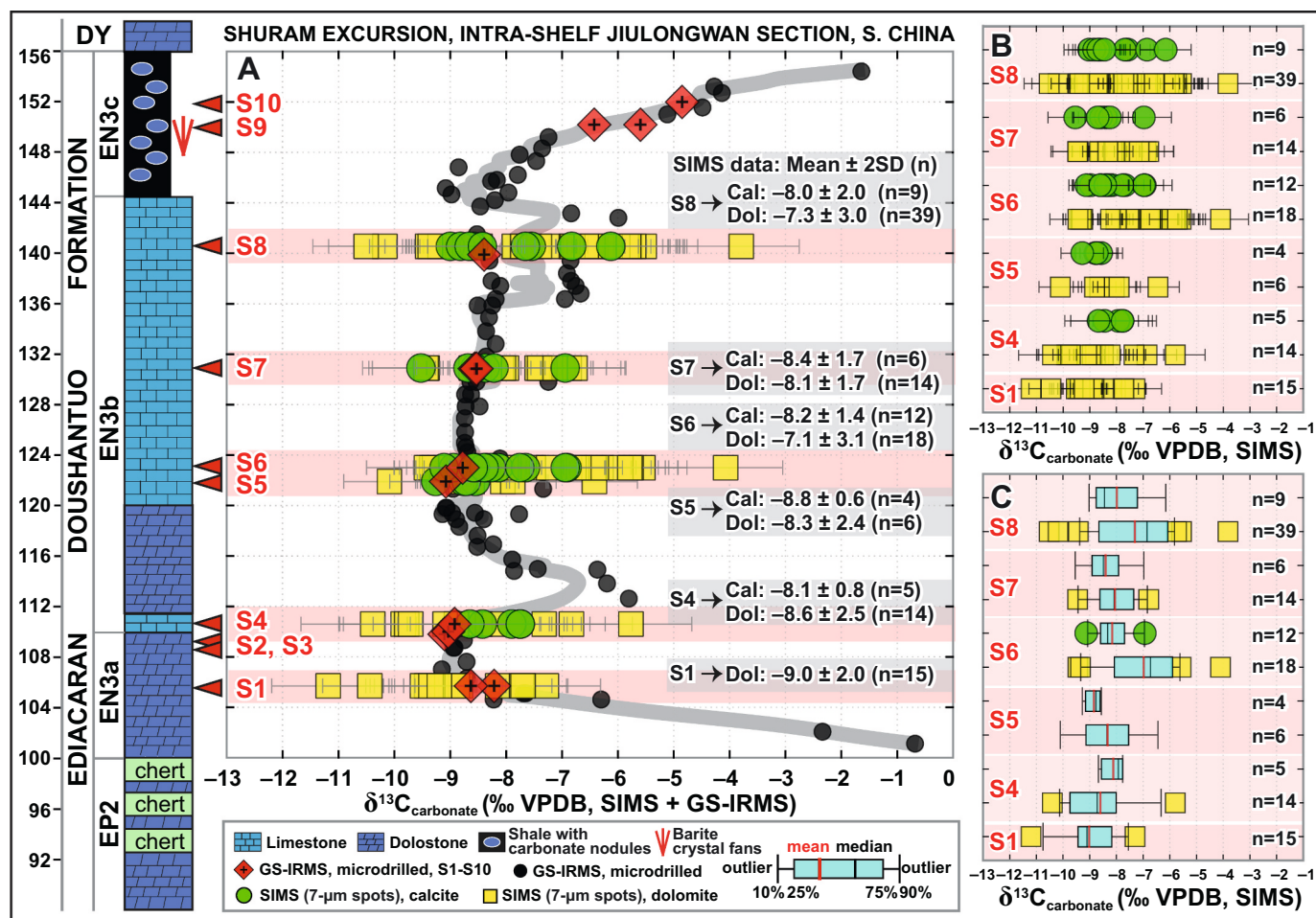**Fig. 5. (A)** Integrated lithological and chemostratigraphic $\delta^{13}C_{carb}$ results of the Shuram Excursion (i.e., EN3 / DOUNCE interval) in the upper Doushantuo Formation at Jiulongwan, South China. Filled black dots represent $\delta^{13}C_{carb}$ data analyzed from micro-drilled powders by GS-IRMS, with the data for samples also analyzed by SIMS highlighted as red diamonds. Green circles and yellow boxes represent SIMS data analyzed from calcite and dolomite, respectively. Error bars show reproducibility as 2 standard deviations of the bracketing analyses on WiscSIMS standard UWC3. Gray curve represents three–point running average based on the GS-IRMS data. Data source: GS-IRMS data (McFadden et al., 2008); SIMS data (this study). **(B)** Plot of each individual SIMS sample, with $\delta^{13}C_{calcite}$ and $\delta^{13}C_{dolomite}$ data offset vertically to improve clarity. **(C)** Box plots of the SIMS $\delta^{13}C_{calcite}$ and $\delta^{13}C_{dolomite}$ data. Note that the mean values of $\delta^{13}C_{calcite}$ and $\delta^{13}C_{dolomite}$ for each sample are identical within uncertainty. The number of SIMS analysis (n) is also provided. Abbreviations: EN = Ediacaran negative excursion; GS-IRMS = gas-source isotope ratio mass spectrometer; SIMS = secondary ion mass spectrometer; SEM = scanning electron microscope; VPDB = Vienna Pee Dee Belemnite; Cal = calcite; Dol = dolomite; DOUNCE = DOUshantuo Negative Carbon isotope Excursion. (For interpretation of the references to color in this figure legend, the reader is referred to the web version of this article.)

5.3. Comparing the SIMS $\delta^{13}C$ data with micro-drilled bulk-rock data

The new SEM–SIMS data in this study allow us to compare the $\delta^{13}C$ results obtained via two different approaches — conventional micro-drilling (ca. 800-μm diameter drill hole) technique vs. in situ SIMS (7-μm beam size) analysis. Compared with the previously published micro-drilled bulk-rock data (McFadden et al., 2008), the SIMS $\delta^{13}C$ results in this study reveal two main features.

First, notable $\delta^{13}C$ variability was found at a single crystal scale (see details in online supplementary materials). Except for Sample S7 that shows similar 2SDs of the measured SIMS $\delta^{13}C$ data on both calcite and dolomite, the other samples show greater SIMS $\delta^{13}C$ variability in dolomite than in calcite (i.e., 2SD$_{dolomite}$ > 2SD$_{calcite}$) (Fig. 5B–C, Table 6). The origin of this phenomenon is not precisely known. We suspect that dolomitization of preexisting calcite may have caused compositional zonation and $\delta^{13}C$ variation at a μm scale. Notably, recent SIMS studies on the lower Doushantuo Formation (Xiao et al., 2019; Xiao et al., 2020b) and elsewhere (Śliwiński et al., 2016b; Denny et al., 2017; Śliwiński et al., 2017; Denny et al., 2020; Husson et al., 2020) also reveal strong $\delta^{13}C$ variations in diagenetic carbonates at a μm scale,

demonstrating the causal link between diagenesis and μm-scale variations in Fe# and $\delta^{13}C$.

It is important to evaluate the uncertainty of SIMS instrumental mass fractionation (IMF) during the analysis of these heavily zoned dolomite grains and to assess whether IMF contributed to the overall larger $\delta^{13}C$ variability of dolomite. The average value of Fe# (= molar ratio of Fe/ [Fe + Mg]) of EPMA pits on dolomite is 0.04 ± 0.04 (1SD), which corresponds to the steepest part of the $\delta^{13}C$ IMF calibration curve (Fig. A2). Thus, it is challenging to accurately correct the raw SIMS $\delta^{13}C$ data of dolomite grains from calcite due to their intrinsic compositional zonation and the relatively small magnitude of IMF when the Fe# numbers are low. That being said, EPMA for each SIMS spot has been carefully conducted in order to make these corrections, and we find that the effect of IMF on the SIMS $\delta^{13}C$ uncertainty should be limited to ca. 2‰ (i.e., IMF varies from ca. –59‰ to ca. –61‰; Fig. A3C, F). Furthermore, if the uncertainty in IMF was the reason for the >8‰ variability seen in this study, there should be consistent correlations of $\delta^{13}C$ values with Fe# (or Mg, Mn) that are not observed (Fig. A3). Therefore, we interpret the differences in $\delta^{13}C_{dolomite}$ to represent variability inherited during the growth of crystals.

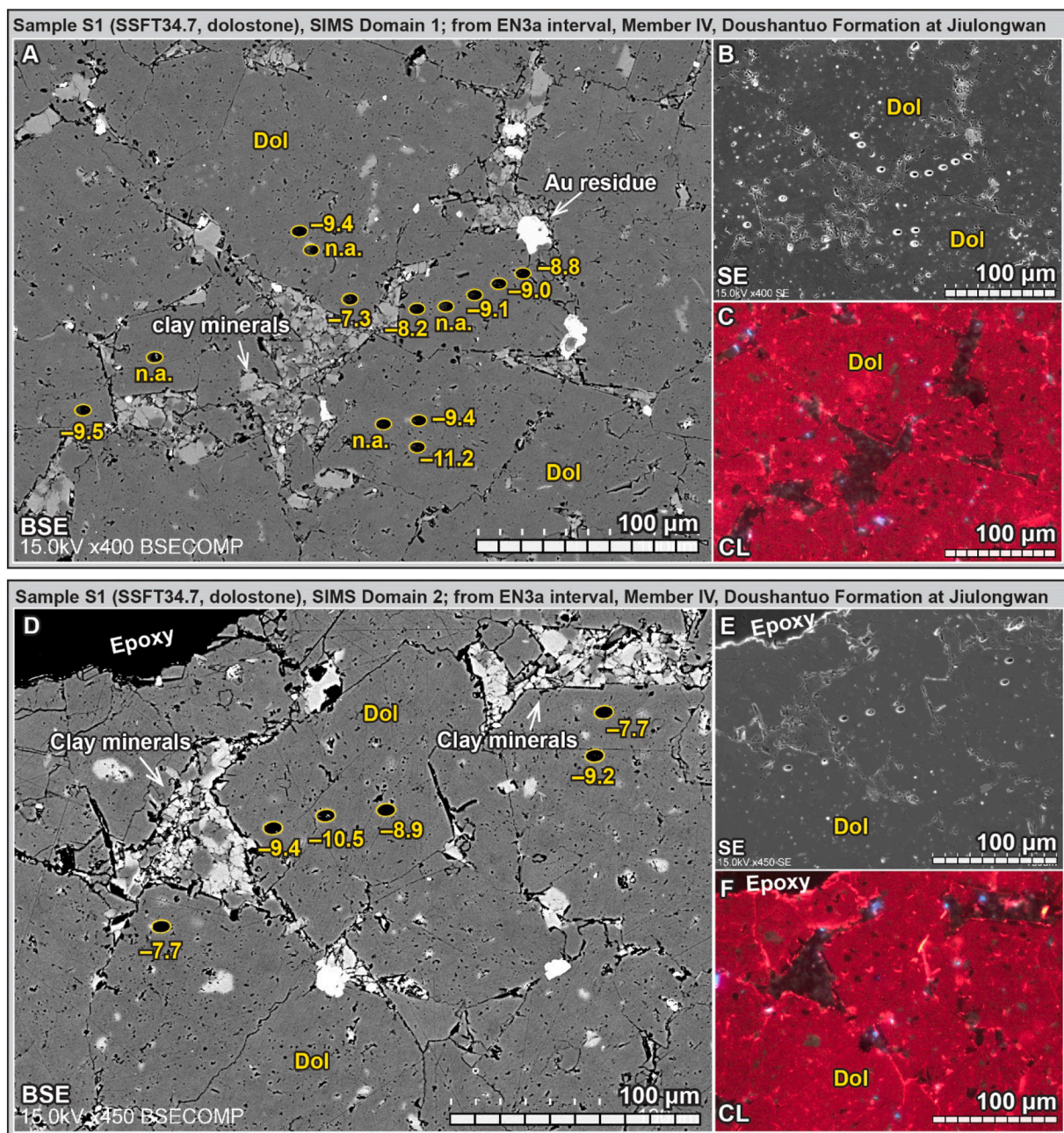**Fig. 6.** Integrated SEM–CL–SIMS results of sample S1 (SSFT34.7). Values of $\delta^{13}C$ are adjacent to 7-μm SIMS pits. **(A–C)** SIMS domain 1; **(D-F)** SIMS domain 2. Note the homogeneous textures under BSE and CL. See Fig. A5B for locations of domains 1–2. Abbreviations: BSE = backscattered electron; SE = secondary electron; SEM = scanning electron microscope; CL = cathodoluminescence; Dol = dolomite.

Second, it is notable that the mean SIMS $\delta^{13}C$ values of calcite and dolomite in each sample are statistically indistinguishable, and are also consistent with the published micro-drilled data (Fig. 1E; Table 6). This likely results from an "averaging effect" of micro-drilling on the measured $\delta^{13}C$ compositions. Basically, micro-drilled powders (with micro-drill bit of ca. 800 μm in diameter) could have averaged the $\delta^{13}C$ heterogeneity revealed by SIMS (7-μm pit size). The overall consistency between SIMS mean value and micro-drilled value also suggest the occurrence of sediment-buffered diagenesis with respect to $\delta^{13}C$. In this regard, the mean SIMS $\delta^{13}C$ values likely reflect $\delta^{13}C$ signals of micrite with a depositional origin.

In summary, the SIMS data in this study reveal notable spatial heterogeneity of $\delta^{13}C$ at a μm scale, with more variation in dolomite than in calcite (i.e., SIMS sample data show $2SD_{dolomite} > 2SD_{calcite}$) in most of

the samples (Fig. 5; Table 6). The mean value of the SIMS $\delta^{13}C$ data is consistent with the previously published micro-drilled data, which likely reflects the averaging effect where micro-drilling excavates and homogenizes powder from multiple μm-scale growth zones. We regard that the mean SIMS $\delta^{13}C$ values in EN3 reflect depositional "background" signals, whereas the μm-scale variation of SIMS $\delta^{13}C$ data among individual spots likely reflects diagenetic variability that was overprinted after deposition.

5.4. Comparing with the SEM-SIMS data of the Wonoka Formation

Typical "Shuram" $\delta^{13}C_{carb}$ values of ca. −10‰ based on micro-drilled bulk powders have been reported from both the EN3 interval in South China (Jiang et al., 2007; McFadden et al., 2008; Zhou et al., 2012; Ling
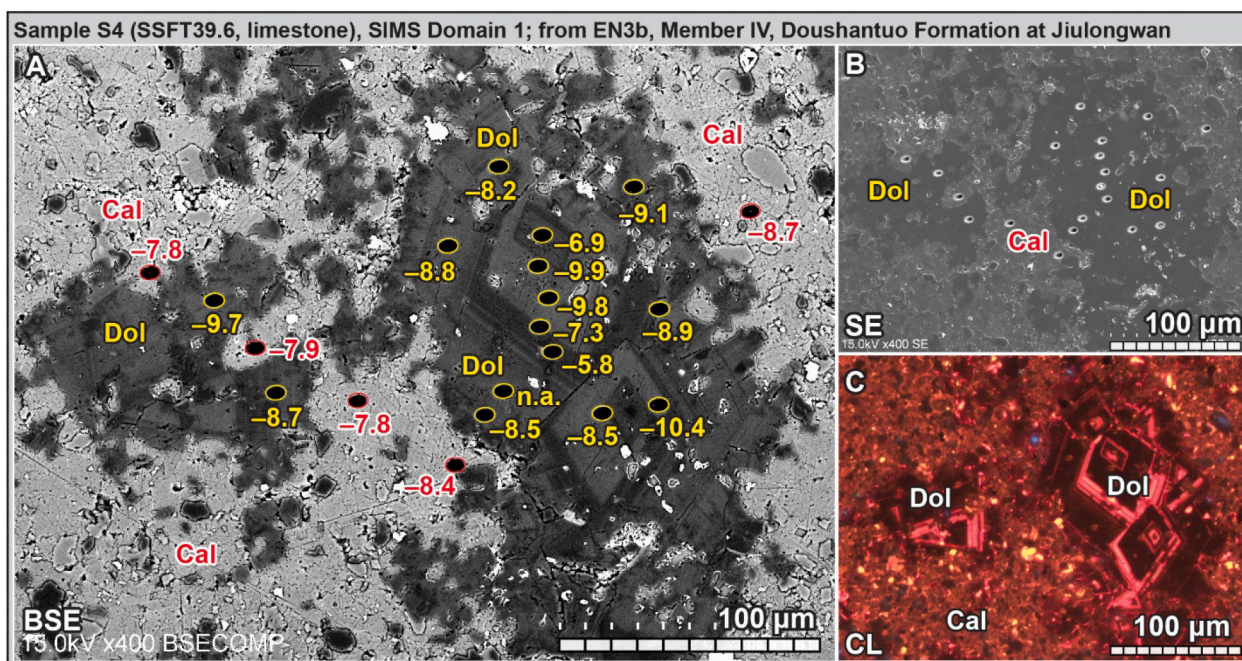
Fig. 7. Petrographic results of Sample 4 (SSFT39.6). See Fig. A8C for domain location. **(A–C)** Integrated SEM–CL–SIMS results of SIMS domain 1 in sample S4 (SSFT39.6). Values of $\delta^{13}C$ are adjacent to 7-μm SIMS pits. Note that the dolomite crystals show irregular boundaries with surrounding calcite microspar. Abbreviations: BSE = backscattered electron; SE = secondary electron; CL = cathodoluminescence; Cal = calcite; Dol = dolomite; n.a. = not available.
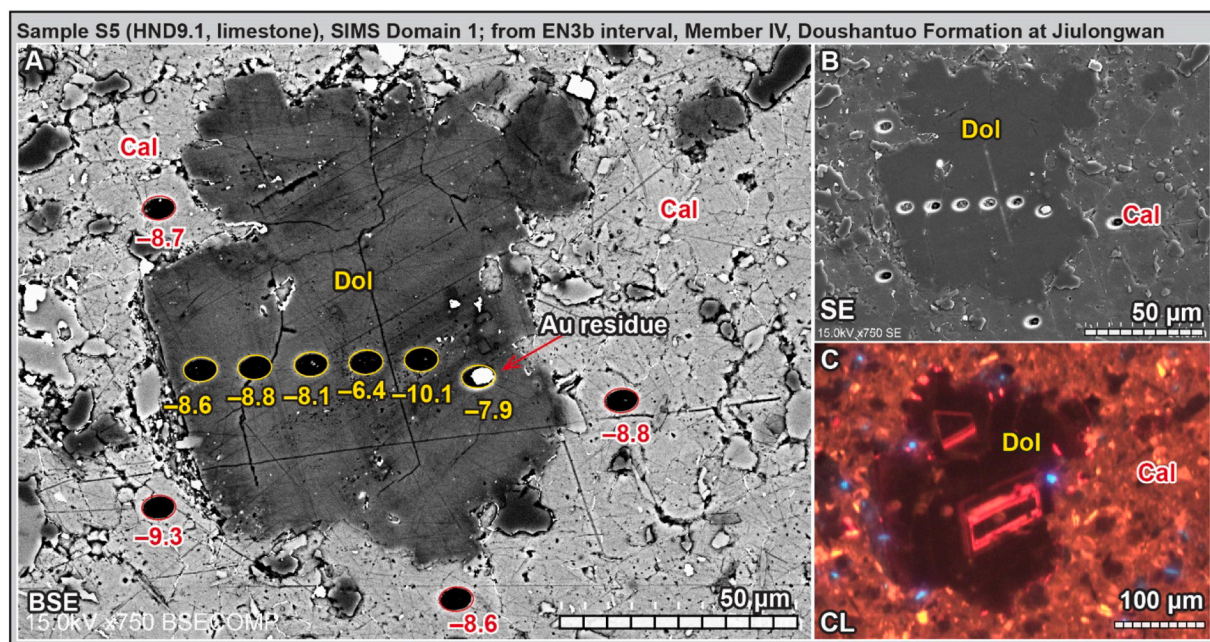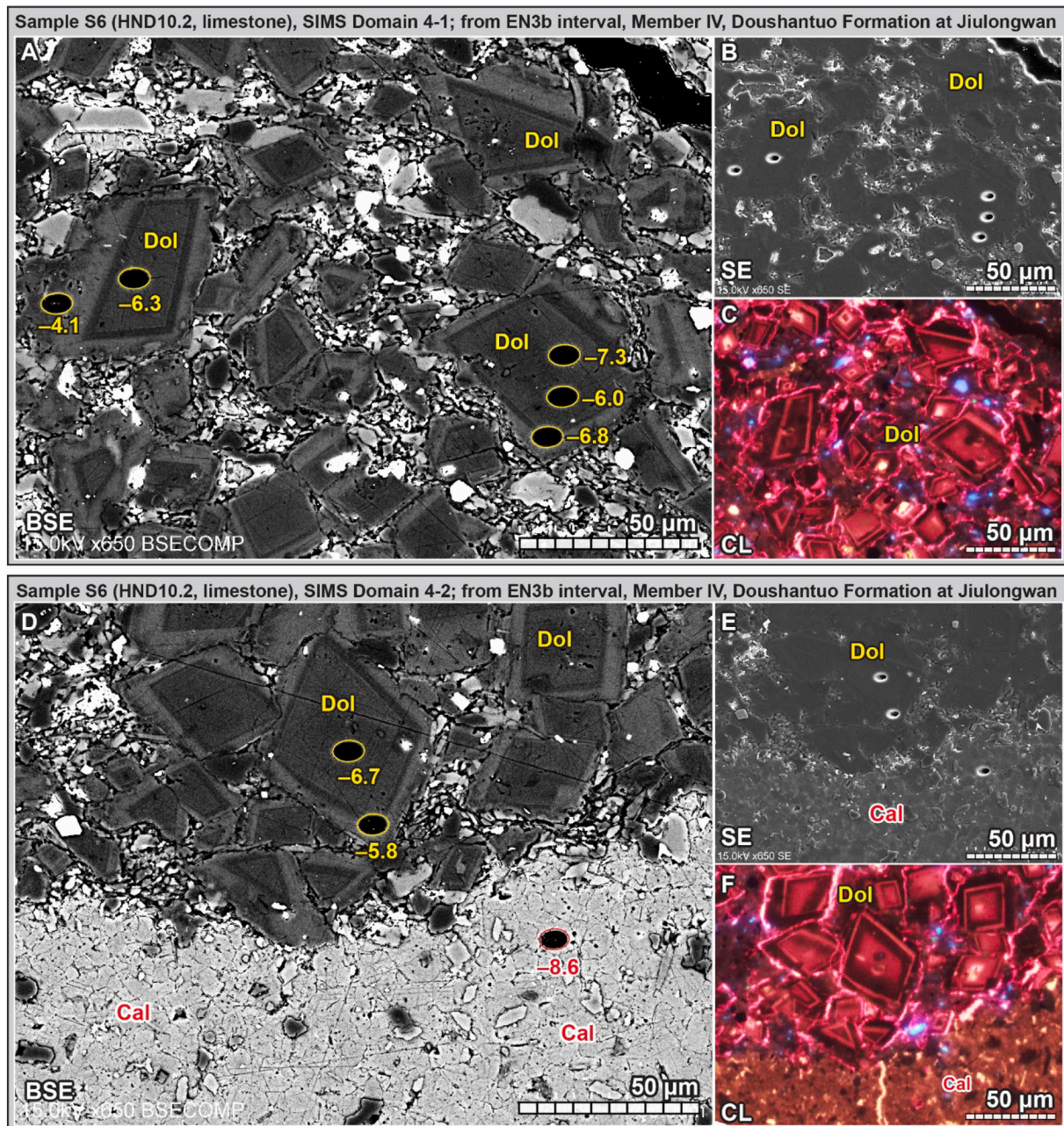

Fig. 8. Integrated SEM–CL–SIMS results of sample S5 (HND9.1). **(A–C)** SIMS domain 1. See Fig. A9B for domain location. Values of $\delta^{13}C$ are adjacent to 7-μm SIMS pits. Abbreviations: BSE = backscattered electron; SE = secondary electron; CL = cathodoluminescence; Cal = calcite; Dol = dolomite.

et al., 2013; Lu et al., 2013; Zhu et al., 2013) and the Wonoka Formation in South Australia (Calver, 2000; Husson et al., 2012; Husson et al., 2015b). Notably, a recent SIMS study of the Wonoka Formation at an outer shelf "canyon-shoulder" section reveals large $\delta^{13}C_{carb}$ variability at a μm-scale, especially in Sample 44.4 (Husson et al., 2020). The new SEM–SIMS data in this study allows for a μm-scale comparison between these correlative stratigraphic units. Below, we will summarize the main features (Table 7) of these two SEM–SIMS data sets.

First, the calcite matrices of the EN3 interval and the Wonoka

Formation show very different petrographic features. The calcite matrix of the EN3 limestone is typically composed of pervasive and homogeneous calcite microspar (5–10 μm grain size) interlocking with each other (e.g., Figs. A12, A13J–L). There is no clear compositional zoning within the EN3 calcite microspar under SEM. In contrast, the calcite matrix of the Wonoka limestone samples show a heterogeneous texture, which is dominated by rounded detrital calcite grains (darker under SEM) and calcite cement overgrowth (brighter under SEM) (Husson et al., 2020). It is evident that the Wonoka calcite grains were
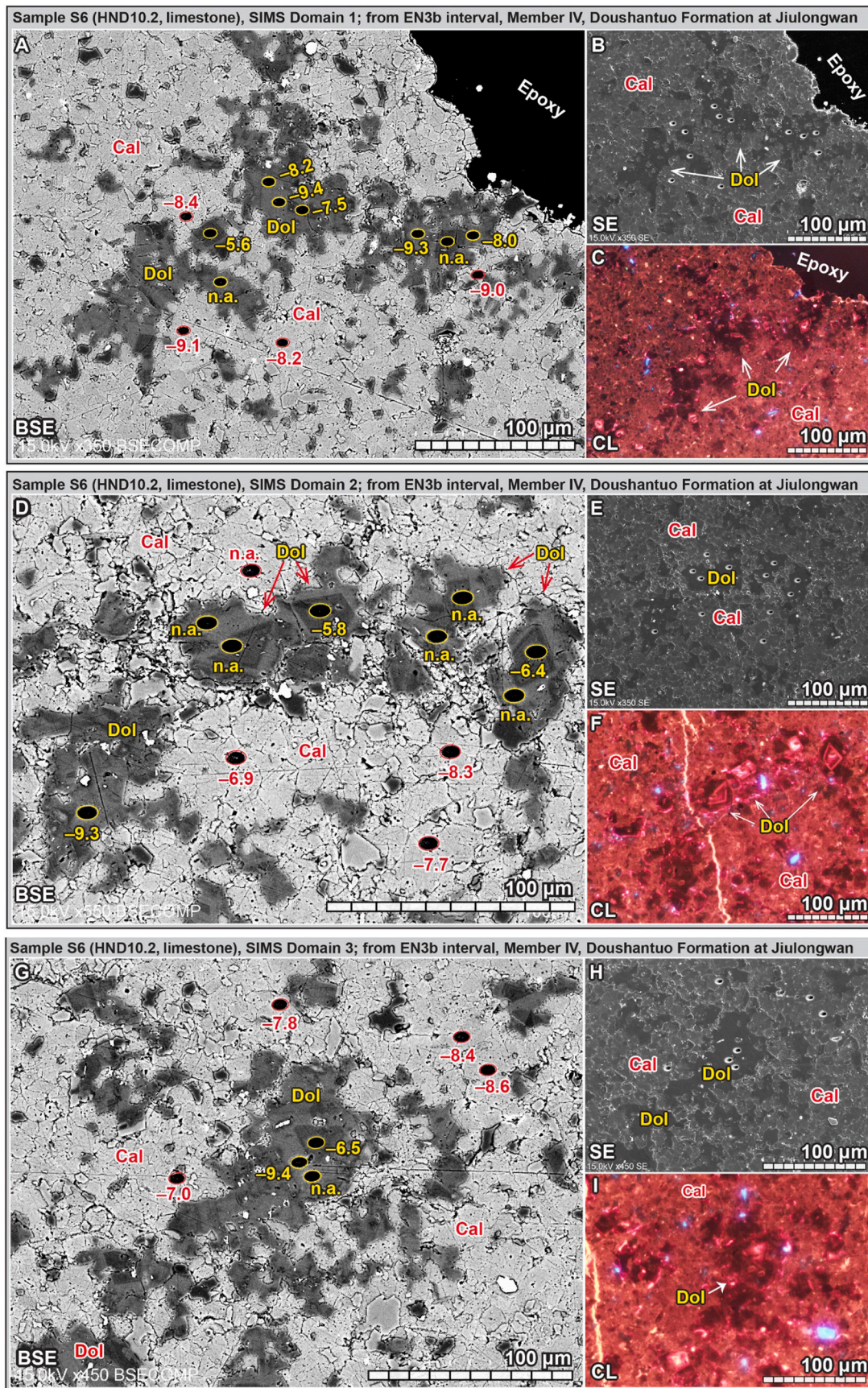
Fig. 9. Integrated SEM–CL–SIMS results of sample S6 (HND10.2). Values of $\delta^{13}C$ are adjacent to 7-μm SIMS pits. **(A–C)** SIMS domain 1; **(D—F)** SIMS domain 2; **(G–I)** SIMS domain 3. Note that the dolomite crystals show irregular boundaries (arrows) with surrounding calcite microspar. See Fig. A10B for domain location. Abbreviations: BSE = backscattered electron; SE = secondary electron; CL = cathodoluminescence; Cal = calcite; Dol = dolomite; n.a. = not available.

Fig. 10. Integrated SEM–CL–SIMS results of sample S6 (HND10.2). **(A–C)** SIMS domain 4–1; **(D—F)** SIMS domain 4–2. Note that the dolomite crystals along stylolite typically show euhedral shapes and zoned textures under BSE and CL. Values of δ^{13}C are adjacent to 7-μm SIMS pits. See Figs. A11B–C for domain location. Abbreviations: BSE = backscattered electron; SE = secondary electron; CL = cathodoluminescence; Cal = calcite; Dol = dolomite.

transported and rounded before final deposition, and were further cemented during early diagenesis.

The causes of these different petrographic features between Doushantuo EN3 and the Wonoka Formation may lie in their different depositional environments. The depositional environment of the Wonoka carbonates studied by Husson et al. (2020) appears to be shallower and more energetic than the Doushantuo Formation at Jiulongwan. The former likely accumulated in a shallow canyon-shoulder environment with dynamic transport and redeposition of detrital grains (Husson et al., 2015b), while the latter was deposited in a protected intra-shelf basin based on sedimentological (Jiang et al., 2011) and chemostratigraphic evidence (Cui et al., 2015). Therefore, the neomorphosed EN3

calcite microspar appears to be autochthonous in comparison with the allochthonous Wonoka carbonate sediments.

Second, the dolomite crystals in the EN3 interval and the Wonoka Formation show contrasting δ^{13}C values. In the EN3 interval, both calcite and dolomite crystals show consistently negative δ^{13}C values that average around −9‰ (Fig. 5). The dolomite crystals in the EN3 limestone samples likely result from post-depositional dolomitization of preexisting calcite in a sediment-buffered diagenetic system (see section 5.1), therefore, inheriting the δ^{13}C signals of calcite matrix to a large extent.

In contrast, dolomite crystals within the Wonoka Formation (in particular, the sample at 44.4 m) show heterogeneous SIMS δ^{13}C values,
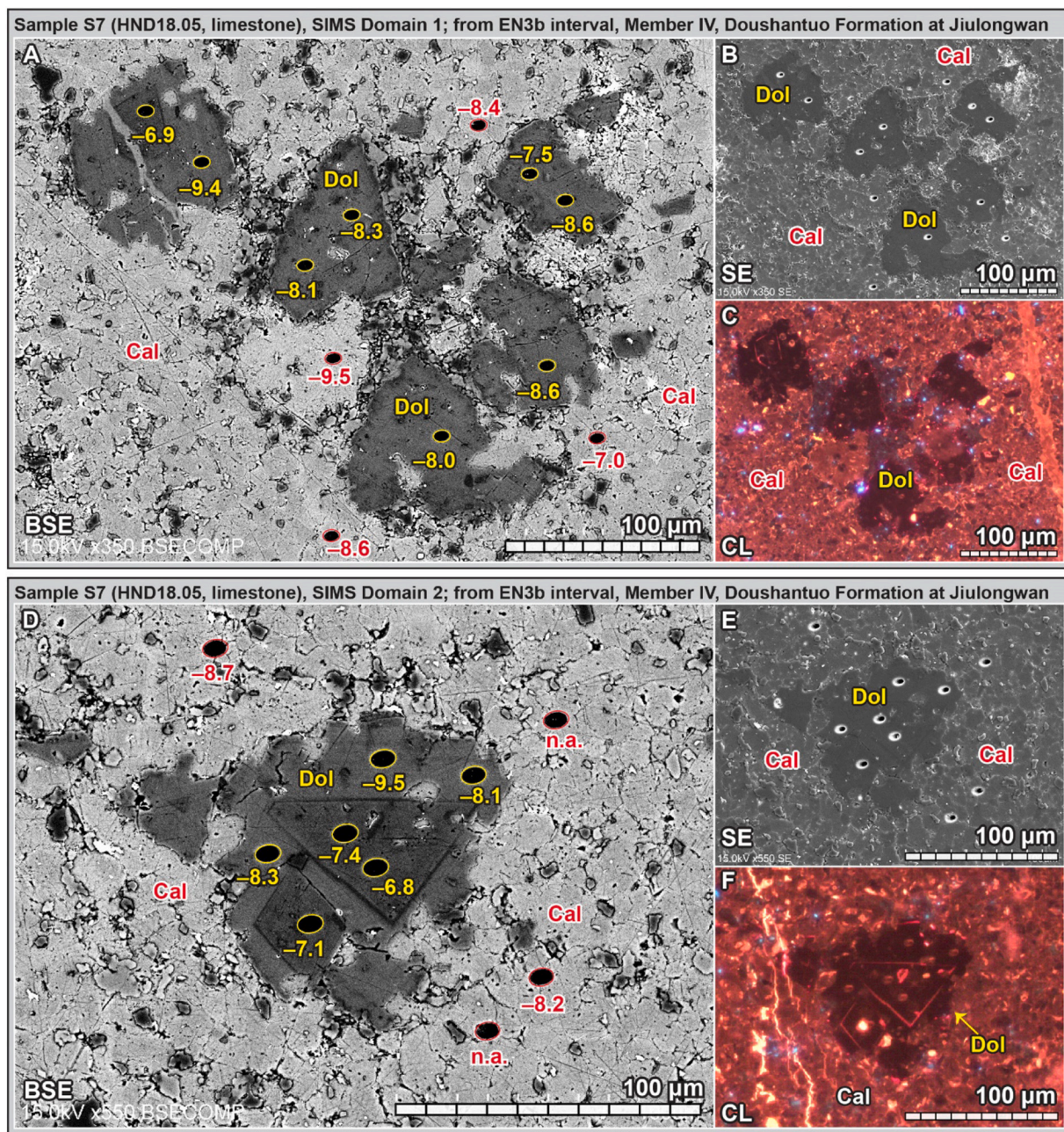
Fig. 11. Integrated SEM–CL–SIMS results of sample S7 (HND18.05). **(A–C)** SIMS domain 1; **(D-F)** SIMS domain 2. Values of δ^{13}C are adjacent to 7-μm SIMS pits. See Fig. A12B for domain location. Abbreviations: BSE = backscattered electron; SE = secondary electron; CL = cathodoluminescence; Cal = calcite; Dol = dolomite.

ranging from ca. +5‰ in the dolomite core down to ca. −10‰ in the dolomite rim (Husson et al., 2020). The origin (early authigenic vs. late diagenetic) of these zoned dolomite crystals in the Wonoka Formation remains enigmatic. Petrographic features appear to be insufficient to reliably reconstruct the paragenesis between dolomite and calcite. Notably, Husson et al. (2020) interpreted these isotopically heterogeneous dolomite crystals as "early authigenic" in origin, which captured positive δ^{13}C signals in shallow seawater (as dolomite cores), and negative δ^{13}C signals of deeper shelf or porewater after deposition (as dolomite rims).

In summary, although the EN3 interval in this study and the Wonoka Formation (Husson et al., 2020) both show typical Shuram-like δ^{13}C values of ca. −10‰ in calcite, they have different petrographic features in calcite and contrasting isotopic values in dolomite (Table 7). The inconsistency between these two sites indicates a complex origin or

diagenetic history of the SE. It is likely that both the depositional facies (shallower in the case of Wonoka; deeper in the case of Jiulongwan) and the diagenetic history (early dolomitization in the case of Wonoka; late dolomitization in the case of Jiulongwan) may have played a role (Table 7).

5.5. Implications for the Shuram excursion

Several contrasting models have been proposed to advocate the existence of a marine DIC (dissolved inorganic carbon) reservoir with a depth-gradient in δ^{13}C during the SE. Based on a basin-scale chemostratigraphic investigation, Jiang et al. (2007) proposed a large δ^{13}C gradient in the marine DIC of the Nanhua Basin, with positive values in shallow shelf and negative values in basinal environment (see a different view in Schrag et al., 2013). Later, Ader et al. (2009) proposed a more
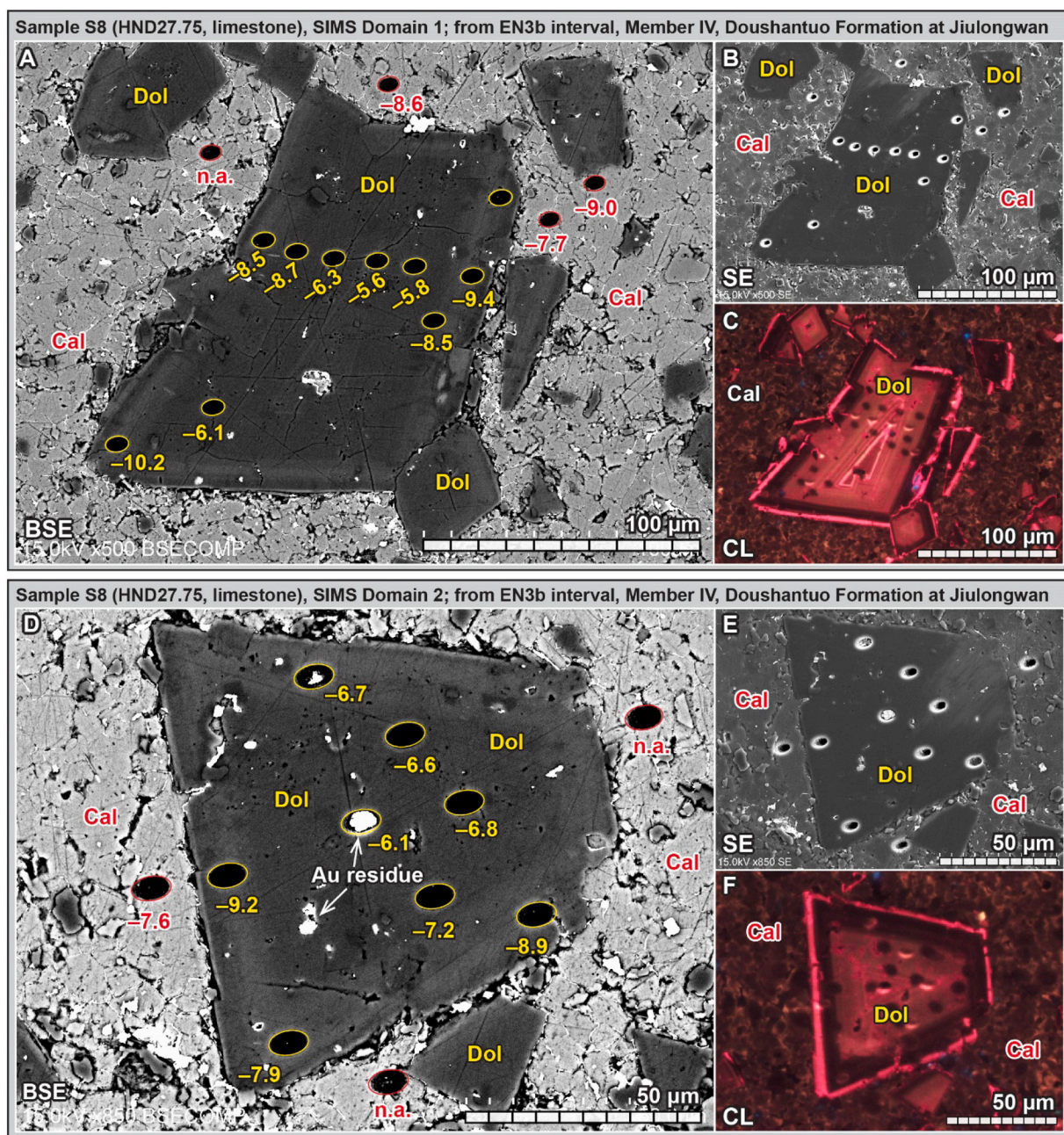
Fig. 12. Integrated SEM–CL–SIMS results of sample S8 (HND27.75). Values of $\delta^{13}C$ are adjacent to 7-μm SIMS pits. **(A–C)** SIMS domain 1; **(D—F)** SIMS domain 2. **(G–I)** SIMS domain 3. **(J–L)** SIMS domain 4. See Fig. A13C for domain location. Abbreviations: BSE = backscattered electron; SE = secondary electron; CL = cathodoluminescence; Cal = calcite; Dol = dolomite.

complex model with positive $\delta^{13}C$ signals in shallow seawater, negative $\delta^{13}C$ signals in an intermediate layer due to the oxidation of organic matter, and positive $\delta^{13}C$ signals at greater depth due to methanogenesis. More recently, Husson et al. (2020) suggested the presence of a large $\delta^{13}C$ gradient with Shuram-like values of −12‰ in shallow waters and positive $\delta^{13}C$ values up to +5‰ in deeper shelf and/or porewaters. Although these models are not exactly the same, a common feature is the existence of a heterogeneous marine DIC reservoir in order to reconcile the coexistence of both positive and negative $\delta^{13}C_{carb}$ signals at either a

μm scale (Husson et al., 2020) or a basinal scale (Jiang et al., 2007; Ader et al., 2009).

Here, in the case of the EN3 interval at Jiulongwan, no positive $\delta^{13}C$ signals have been found after a thorough investigation by SIMS. Instead, all the SIMS $\delta^{13}C$ data measured in this study show negative values with μm-scale variability (Fig. 5). On the one hand, our SIMS data do not offer support to the isotopically heterogeneous DIC models mentioned above (Jiang et al., 2007; Ader et al., 2009; Husson et al., 2020). On the other hand, the lack of positive $\delta^{13}C$ signals in this study does not necessarily

Sample S8 (HND27.75, limestone), SIMS Domain 3; from EN3b interval, Member IV, Doushantuo Formation at Jiulongwan

Sample S8 (HND27.75, limestone), SIMS Domain 4; from EN3b interval, Member IV, Doushantuo Formation at Jiulongwan
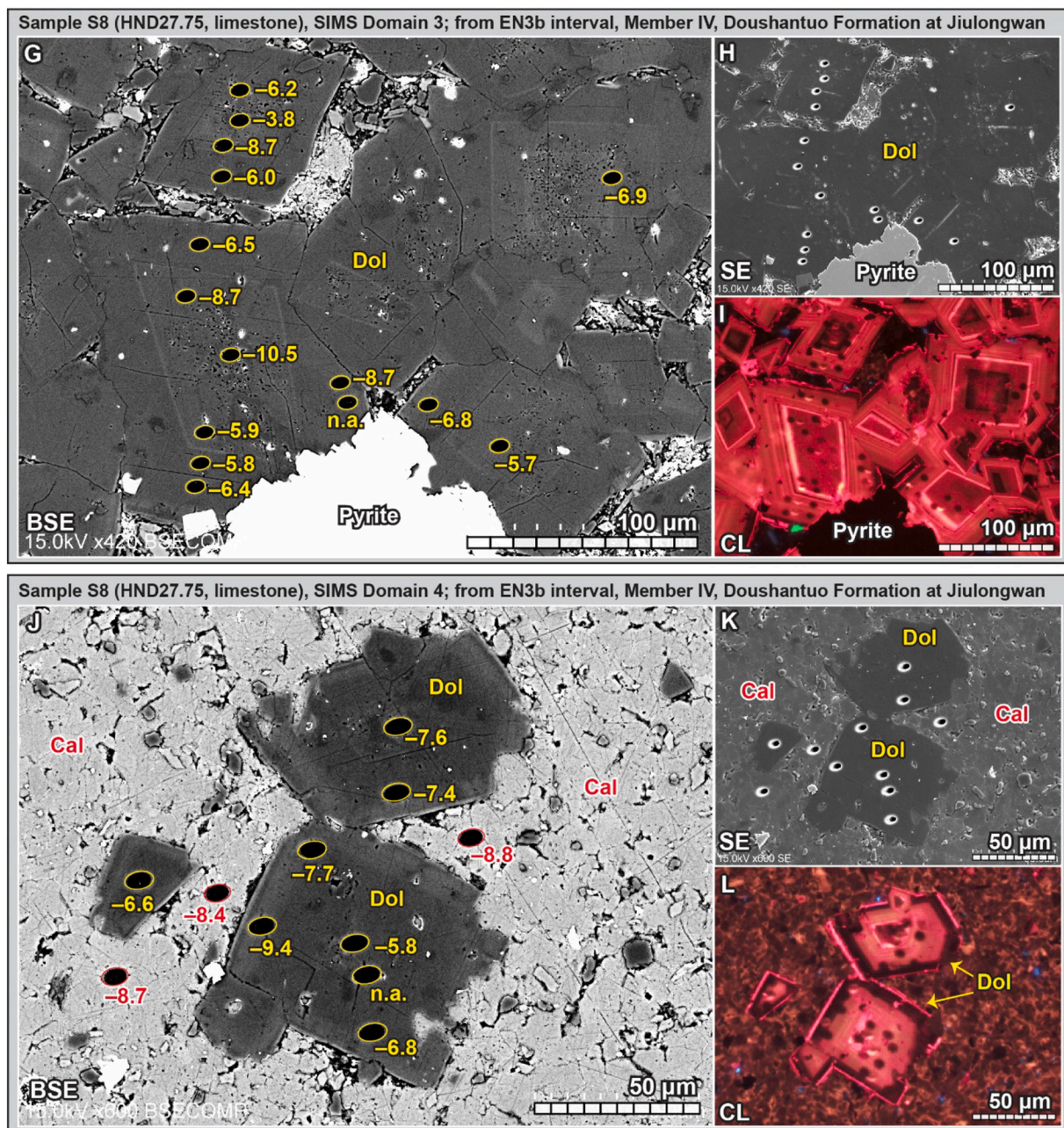
Fig. 12. (*continued*).

rule out the possibility of an isotopically heterogeneous ocean during the SE. Nevertheless, our data indicate that the Shuram-like values of ca. −10‰ are likely of depositional origin, rather than post-depositional signals (Knauth and Kennedy, 2009; Derry, 2010; Zhao et al., 2020).

It should also be emphasized that, although we favor a depositional origin for EN3, our results do not preclude the influence of authigenesis on EN3 $\delta^{13}C$ signals during syndeposition (e.g., $\delta^{13}C$ resetting by sulfate-driven anaerobic oxidation of organic matters during early diagenesis) (Grotzinger et al., 2011; Schrag et al., 2013; Cui et al., 2017), which are expected to retain depositional textures to a large extent. A depositional origin for the EN3 also does not necessarily mean that the Shuram-like values (i.e., $\delta^{13}C$ = ca. −10‰) must be open-ocean signals. The possibility of a locally maintained Shuram-like DIC reservoir in a restricted basin (Cui et al., 2013; Cui et al., 2017; Li et al., 2017) still remains viable. In other words, our study provides constraints for the "timing" of the EN3 anomaly (i.e., depositional, instead of post-depositional), but

more studies are needed to further determine the sources of alkalinity (seawater vs. porewater), the sources of low-$\delta^{13}C$ carbon (methane, DOC, or others), and the geographic extent (open ocean vs. local basin) of the SE.

6. Conclusions

In this study, we provide the first integrated SEM–CL–SIMS data set for the SE-equivalent EN3 interval of the Doushantuo Formation at Jiulongwan, South China. SEM observation shows that the EN3 samples at Jiulongwan were subjected to different degrees of dolomitization. Dolostones in the EN3a interval (Figs. 6, A5–7) and dolomite nodules in the EN3c interval (Figs. A14–15) show pervasive dolomite crystals with weak zoning, whereas dolomitic limestone samples in the EN3b interval contain zoned dolomite crystals that are either disseminated in the calcite matrix or occur in patches (Figs. 7–12). Some dolomite crystals in

Table 7

A comparison of the calcite and dolomite phases in the SE of the Wonoka Formation, South Australia (Husson et al., 2020) and the EN3 interval at Jiulongwan, South China (this study). See section 5.4 for detailed discussion.

Mineralogy	Investigation	Wonoka Formation, South Australia (Husson et al., 2020)	EN3 interval, South China (this study)
Calcite	SEM petrography	Rounded and zoned grains with overgrowth cement	Homogeneous microspar with interlocking boundary
	SIMS δ^{13}C (VPDB)	ca. –12‰	ca. –9‰
	Interpretation	Detrital grains from shallow shelf environment; Cement precipitation after deposition; SIMS δ^{13}C signals of shallow marine DIC	Depositional micrite in intra-shelf environment; Neomorphism during authigenesis; SIMS δ^{13}C signals of a depositional origin
Dolomite	SEM petrography	Euhedral, zoned	Large (up to 100 μm), disseminated, zoned, showing straight or irregular boundaries with surrounding calcite microspar
	SIMS δ^{13}C (VPDB)	From ca. –10‰ to +5‰	ca. –9‰, with μm-scale variability
	Interpretation	Early authigenic dolomitization; Heterogeneous δ^{13}C signals in marine DIC reservoirs, with negative δ^{13}C in shallow seawater and positive δ^{13}C in deeper depth or porewater	Post-depositional dolomitization; Sediment-buffered diagenesis with respect to δ^{13}C; μm-scale variability overprinted by diagenesis

EN3b also occur along stylolites (Fig. A11). Although the precise timing of dolomitization is still not well constrained, post-depositional dolomitization in a sediment-buffered diagenetic system with respect to δ^{13}C is preferred in this study.

Detailed petrographic observations in this study (Figs. 6–12; see more detailed results in the supplementary materials) reveal no supporting evidence for the previously hypothesized meteoric and mixing-zone diagenesis (Knauth and Kennedy, 2009; Zhao et al., 2020) and wholesale late burial diagenesis (Derry, 2010). Instead, the limestone samples in EN3b appear overall to be well preserved, although post-depositional dolomitization altered the samples to various degrees. (See Fig. 12.)

Six samples from the EN3 interval were analyzed by SIMS in this study. The SIMS (7-μm pit diameters) data reveal notable spatial variability of δ^{13}C at a μm scale, with more variation in dolomite than in calcite (i.e., SIMS data $2SD_{dolomite} > 2SD_{calcite}$) in most of the samples (Fig. 5; Table 6). The mean value of the SIMS δ^{13}C data is consistent with the previously published micro-drilled bulk-rock data, which likely reflects the averaging effect of micro-drilling. We regard that the mean SIMS δ^{13}C values in EN3 reflect depositional signals, whereas the μm-scale variations of SIMS δ^{13}C data among individual spots likely reflect different degrees of diagenetic alteration.

Compared with the supposedly correlative Wonoka Formation in South Australia (Husson et al., 2020), the EN3 interval shows different petrographic features in calcite and contrasting isotopic values in

dolomite (Table 7). The inconsistency between these two sites highlights the complexity of depositional and diagenetic histories of the two basins during deposition of the SE. It is likely that local facies (shallower in the case of Wonoka; deeper in the case of Jiulongwan) and diagenetic history (early dolomitization in the case of Wonoka; late dolomitization in the case of Jiulongwan) may have played a role (Table 7).

Our study provides petrographic and geochemical constraints for the timing (i.e., a depositional origin, instead of a burial or meteoric diagenetic origin) of the EN3 event, and demonstrates that coupled petrographic and in situ analysis is an effective tool to assess the origins of deep-time δ^{13}C anomalies. It should be emphasized that a depositional origin for EN3 is not mutually exclusive with the previously published hypotheses that purport an early authigenic origin of the SE, which can retain primary depositional texture to a large degree (Schrag et al., 2013; Cui et al., 2017; Jiang et al., 2019) and/or a locally maintained Shuram-like DIC reservoir in a restricted basin (Cui et al., 2013; Cui et al., 2017; Li et al., 2017). More studies are needed to further constrain the sources of alkalinity (seawater vs. porewater), the sources of low-δ^{13}C carbon (methane, DOC, or others), and the geographic extent (open ocean vs. local basin) of the SE.

Contributions

HC designed research; SX provided samples collected by McFadden et al. (2008); HC and MJS prepared samples for SIMS analysis; HC and IJO performed SIMS analysis at JWV's WiscSIMS Laboratory; HC and JHF performed SEM and EPMA analyses; KK, IJO, AD, and HC corrected raw SIMS data; HC and JMB performed CL analysis; HC interpreted the results and wrote the manuscript with contributions from all coauthors. All authors contributed to discussion and manuscript revision.

Declaration of Competing Interest

The authors declare that they have no conflict of interests.
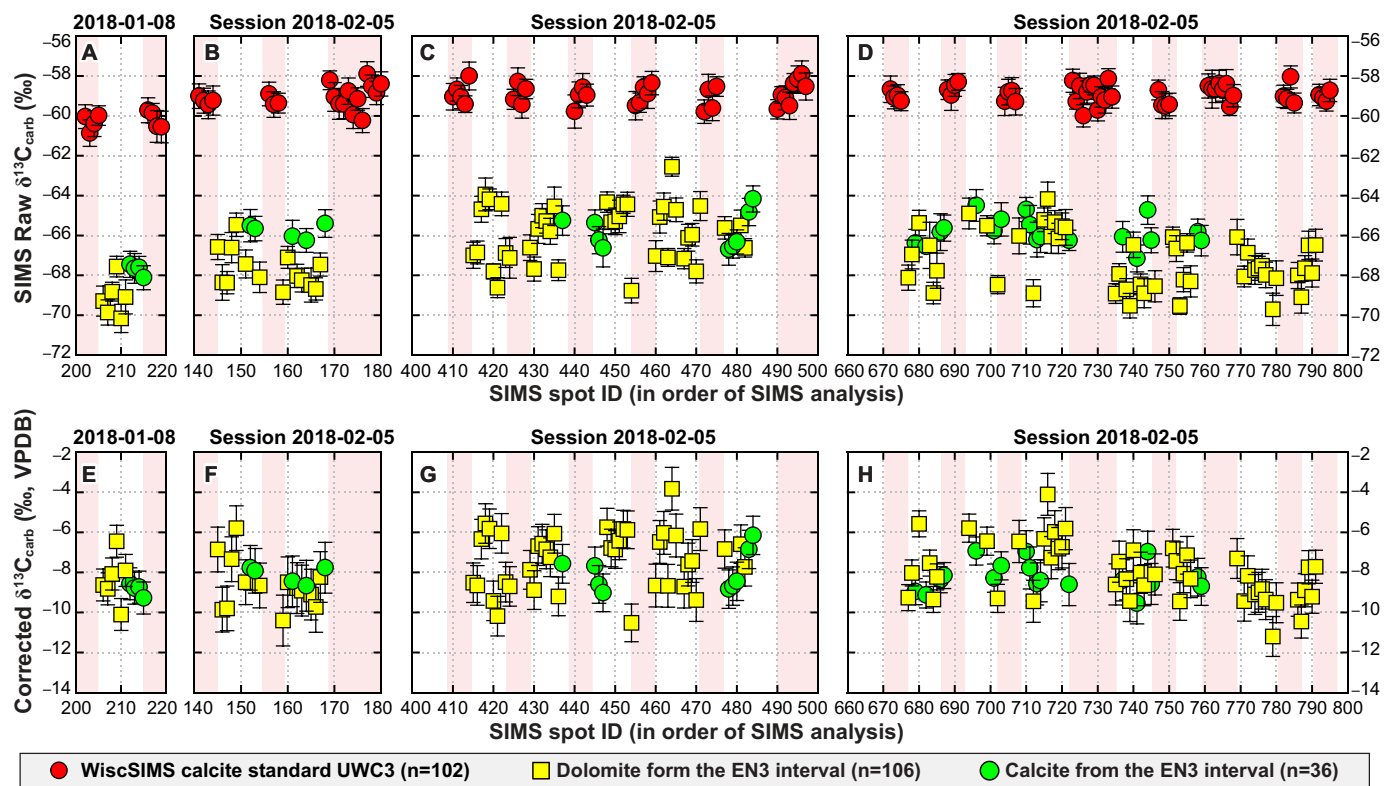
Acknowledgements

Appendices A1–A15

Fig. A1. **(A–D)** Raw $\delta^{13}C_{carbonate}$ data in order of SIMS analysis during four individual sessions. Error bars represent 2 standard errors. Red-shaded intervals represent the analyses of UWC3 calcite standard. **(E–H)** Corrected $\delta^{13}C_{carbonate}$ data (‰, VPDB) in order of SIMS analysis during four individual sessions. Error bars represent 2 standard deviations based on the analysis of bracketing UWC3 standard. All the data can be found in the Excel spreadsheet of the online appendices.
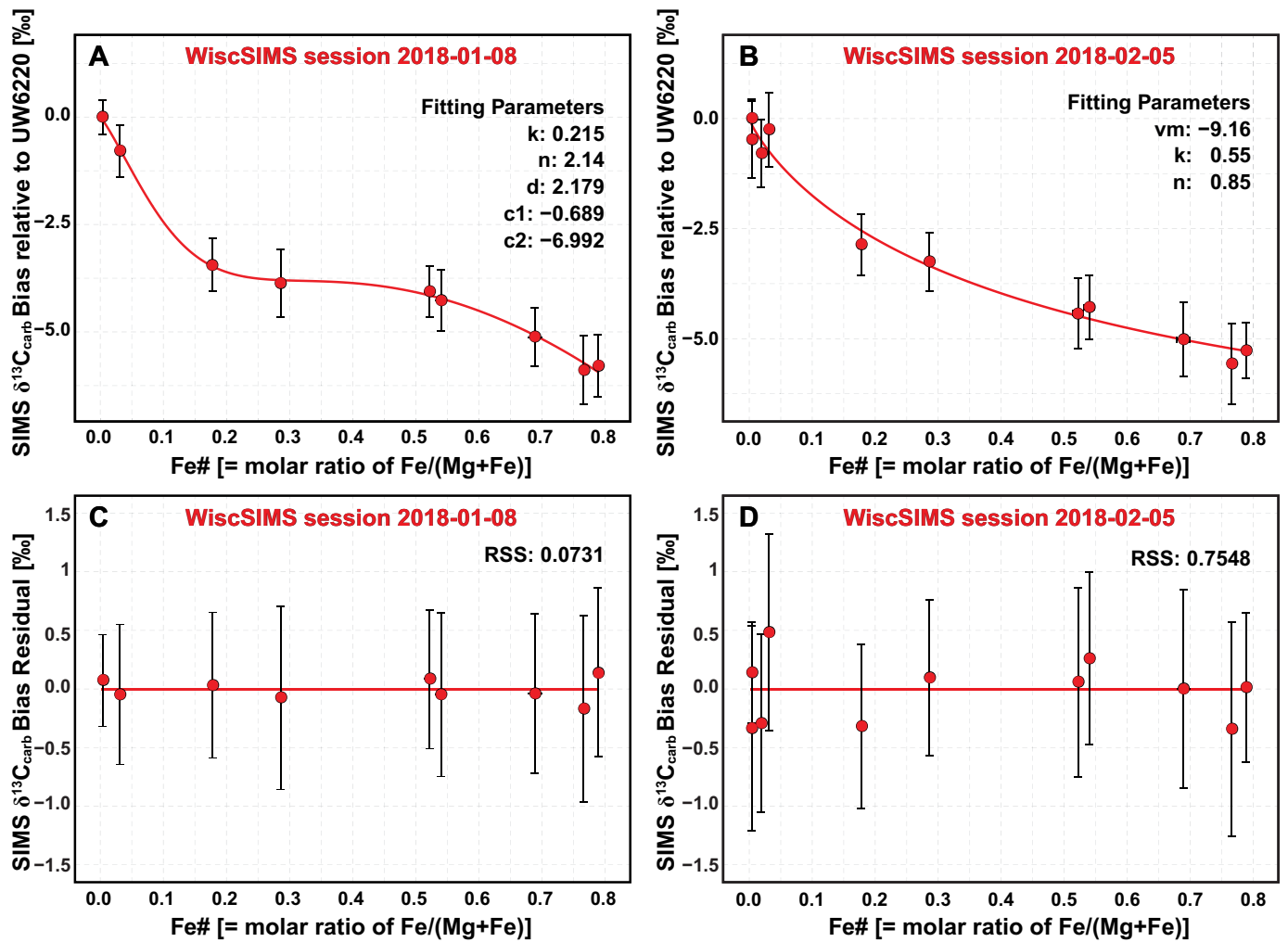
Fig. A2. SIMS $\delta^{13}C_{carb}$ bias (i.e., Instrumental Mass Fractionation, IMF) during WiscSIMS session 2018-01-08 and session 2018–02–05 plotted against Fe# [= molar ratio of Fe/(Mg + Fe)]. **(A, B)** SIMS bias relative to WiscSIMS dolomite standard UW6220. **(C, D)** SIMS bias residuals after correction. Error bars represent propagated errors [= (ERR_RM^2 + ERR_STD^2)$^{0.5}$] calculated from the 2SE of reference materials (i.e., calibration standards) (ERR_RM) and the 2SE of bracketing standards for calibration standards (ERR_STD).
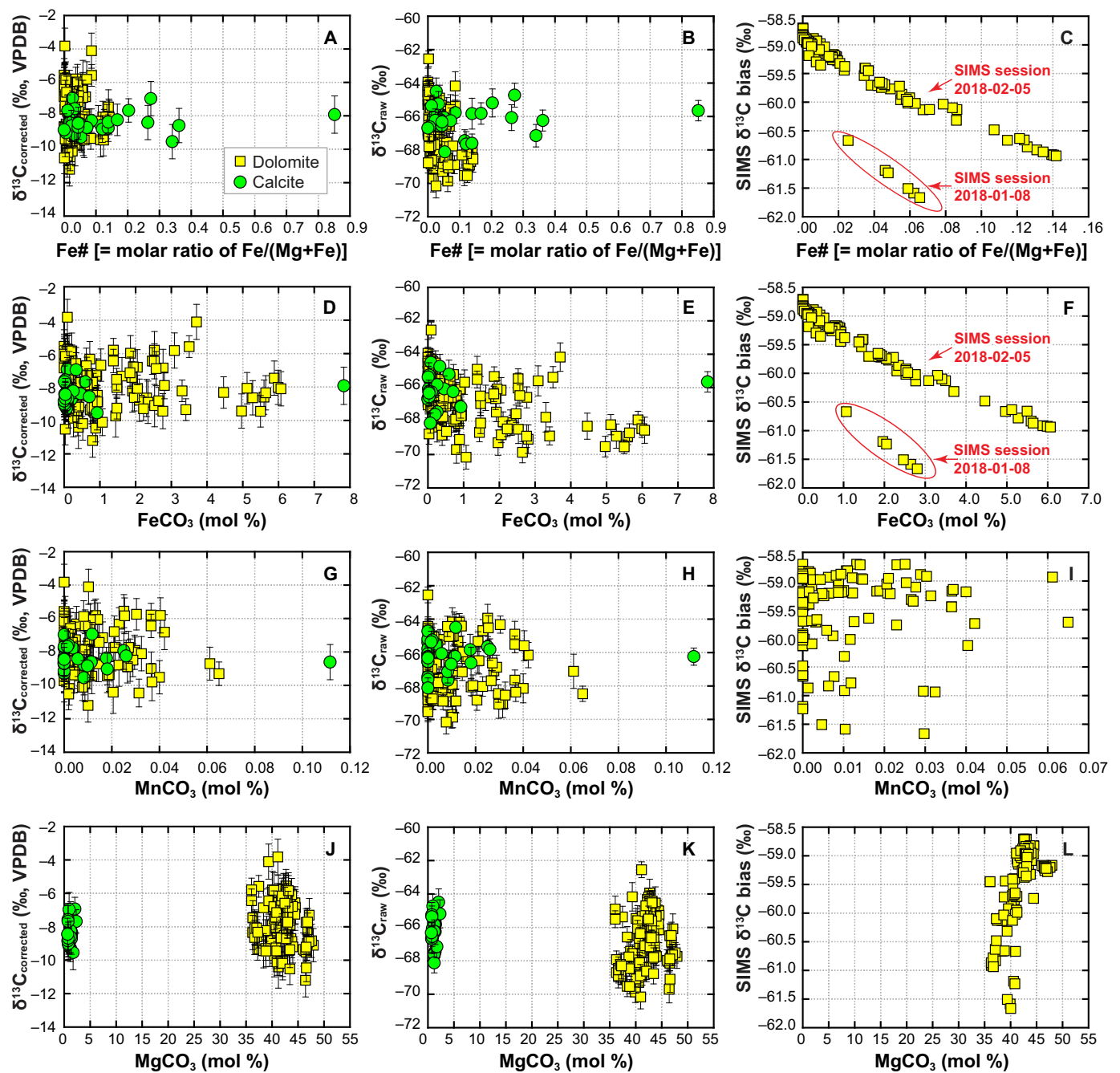
Fig. A3. Cross-plots of the SIMS data vs. EPMA data. Green circles represent calcite, yellow squares represent dolomite. The SIMS $\delta^{13}C_{calcite}$ data analyzed from EN3 were corrected for IMF using data from UWC3 and only SIMS $\delta^{13}C_{dolomite}$ data were corrected for matrix effects due to Mg—Fe solid solution. **(A–C)** Corrected SIMS data, raw SIMS data, and instrumental bias vs. Fe# [= molar ratio of Fe/(Mg + Fe)]. **(D-F)** Corrected SIMS data, raw SIMS data, and instrumental bias vs. FeCO$_3$ (mol %). **(G–I)** Corrected SIMS data, raw SIMS data, and instrumental bias vs. MnCO$_3$ (mol%). **(J–L)** Corrected SIMS data, raw SIMS data, and instrumental bias vs. MgCO$_3$ (mol%). Note that panels C and F show two distinct arrays, which represent instrumental bias during two different WiscSIMS analytical sessions. These two distinct arrays demonstrate the necessity of establishing independent calibration curve for each individual session. (For interpretation of the references to color in this figure legend, the reader is referred to the web version of this article.)
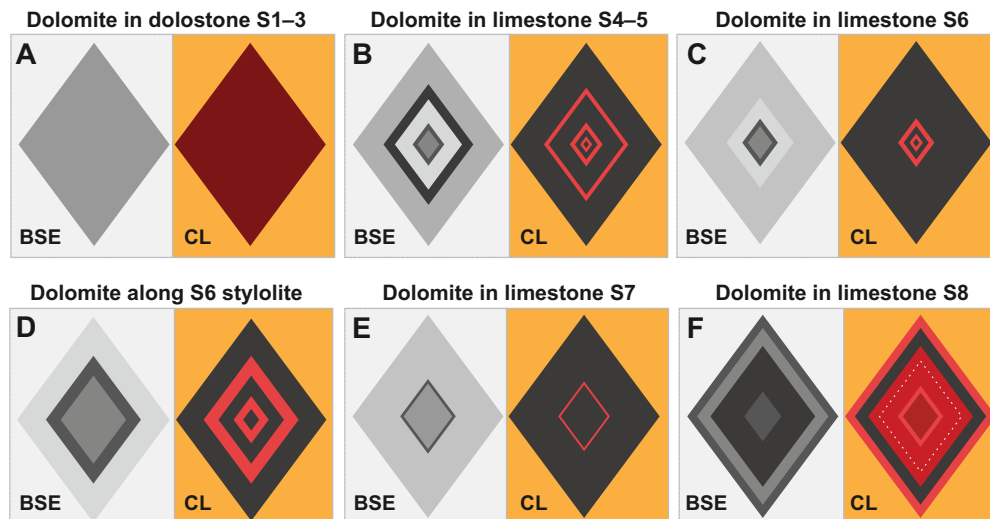
Fig. A4. Typical examples of EN3 dolomite under BSE and CL. Zonation of dolomite crystals typically shows complementary brightness under BSE and CL: darker BSE zones (lower Fe) correspond to brighter CL zones, and vice versa. Note that dolomite crystals in the EN3 limestone samples often show irregular boundaries with surrounding calcite microspar matrix (e.g., Fig. A10). Abbreviations: BSE = backscattered electron; CL = cathodoluminescence.
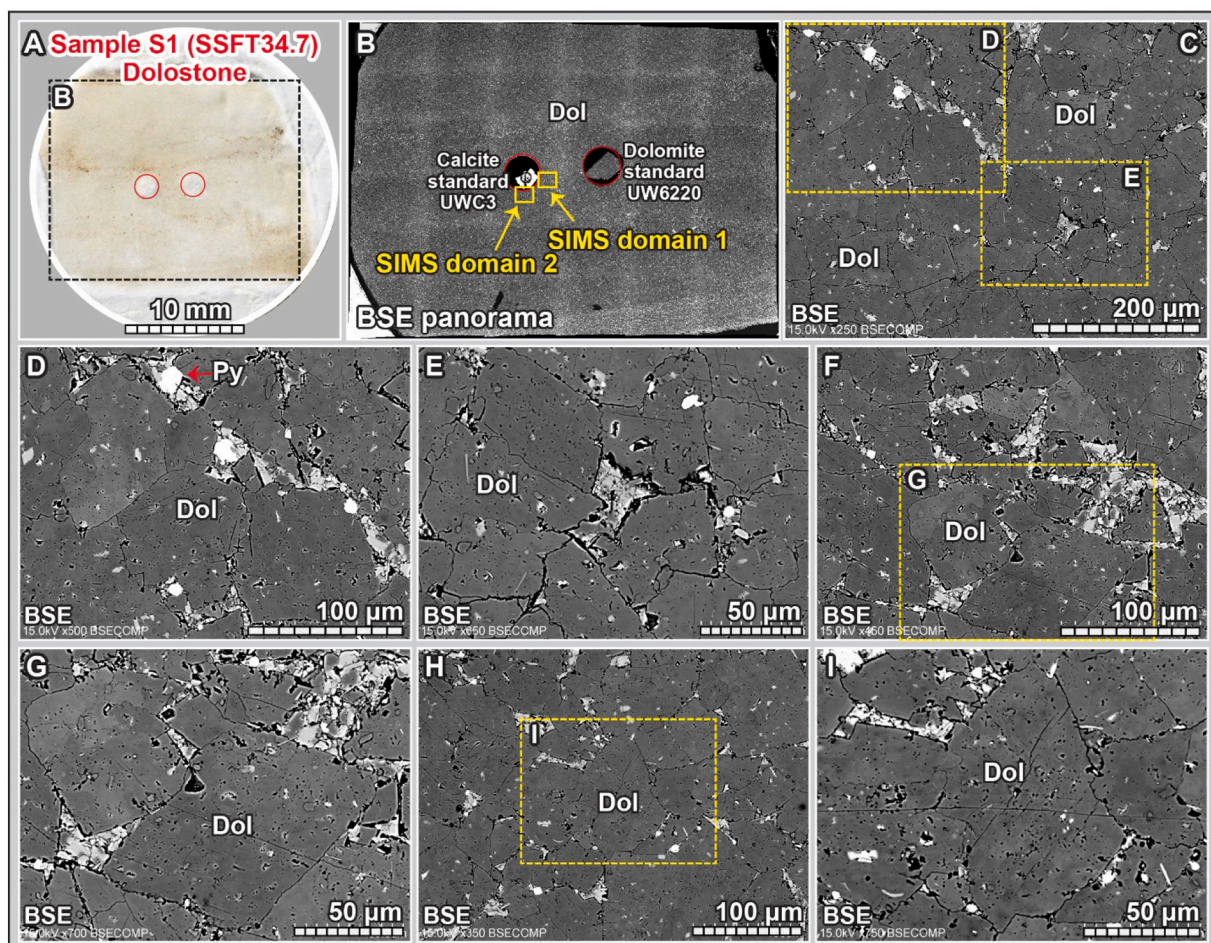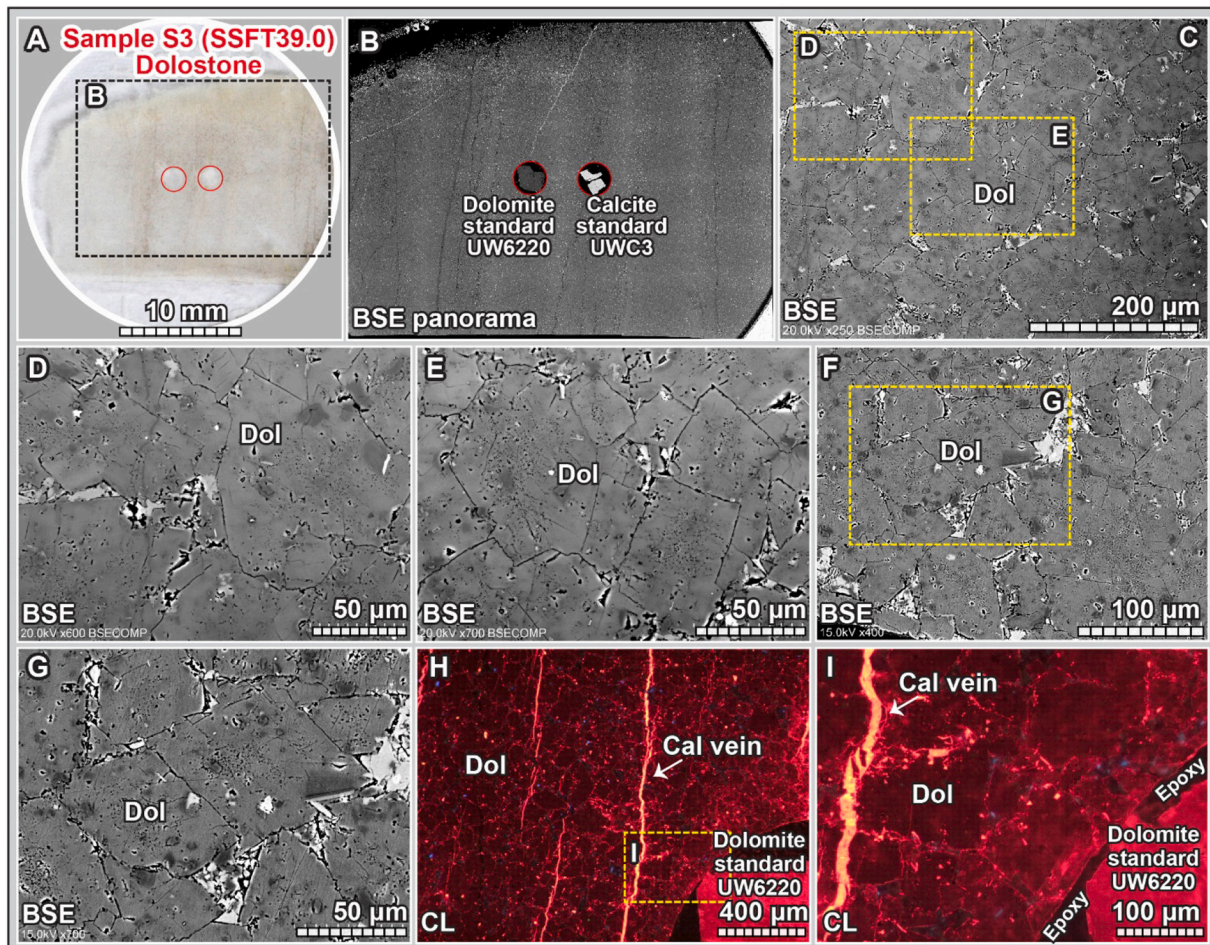

Fig. A5. Petrographic results of sample S1 (SSFT34.7). **(A)** SIMS thin section with WiscSIMS calcite standard UWC3 and dolomite standard UW6220 mounted in the center. **(B)** BSE panorama of the dash box in A based on the integration of 6 × 6 individual BSE images. **(C–I)** BSE images of dolomite crystals showing euhedral to subhedral textures. Abbreviations: BSE = backscattered electron; Cal = calcite; Dol = dolomite.
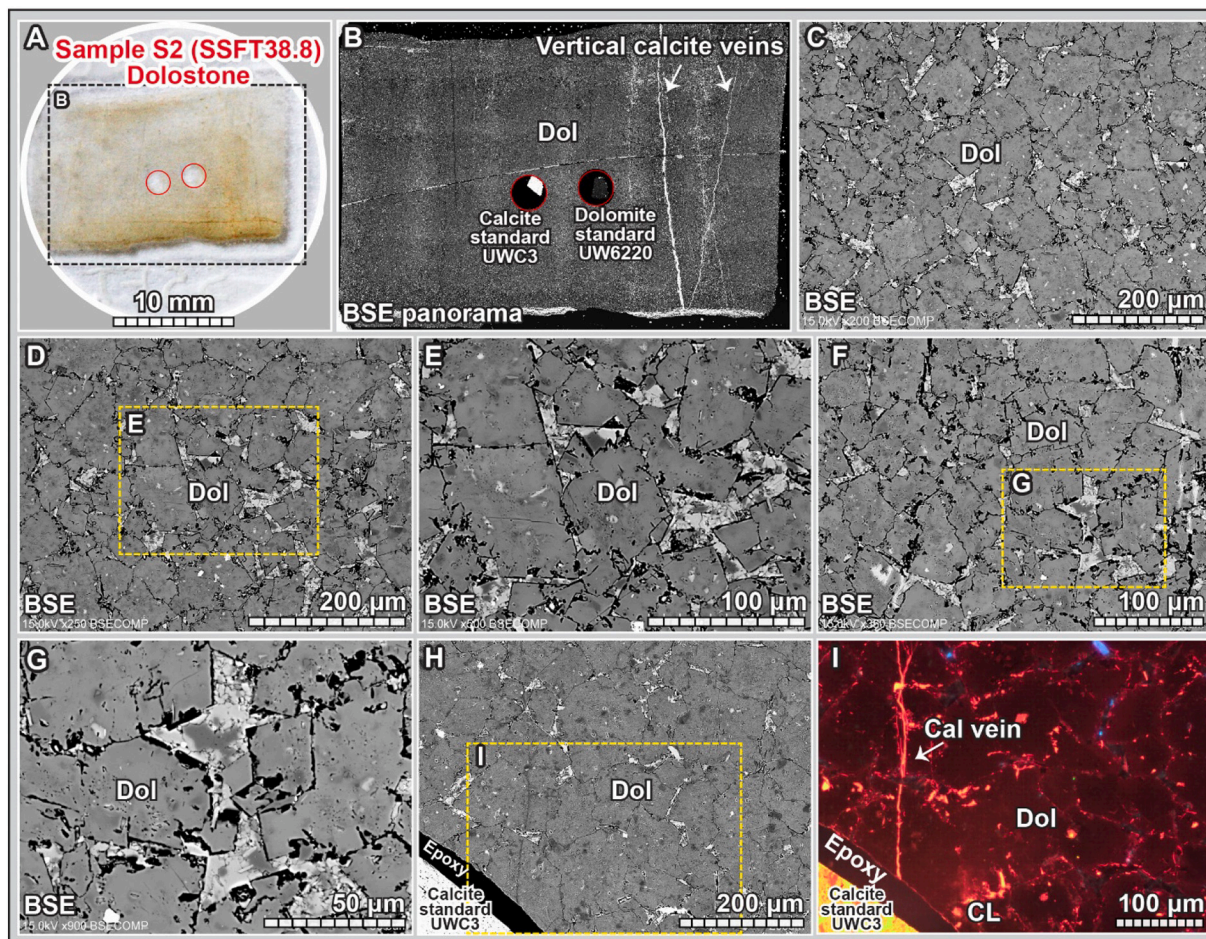
Fig. A6. Petrographic results of Sample S2 (SSFT38.8) in this study. **(A)** SIMS thin section with calcite standard UWC3 and dolomite standard UW6220 mounted in the center. **(B)** BSE panorama based on the integration of 6 × 6 individual BSE images. **(C—H)** BSE images of dolomite in this sample. **(I)** CL image of dolomite in this sample. The lower left corners in H and I show the WiscSIMS calcite standard UWC3 that was mounted in the center of the thin section before SIMS analysis. Note the homogeneous textures under BSE and CL. Abbreviations: BSE = backscattered electron; SEM = scanning electron microscope; CL = cathodoluminescence; Dol = dolomite.
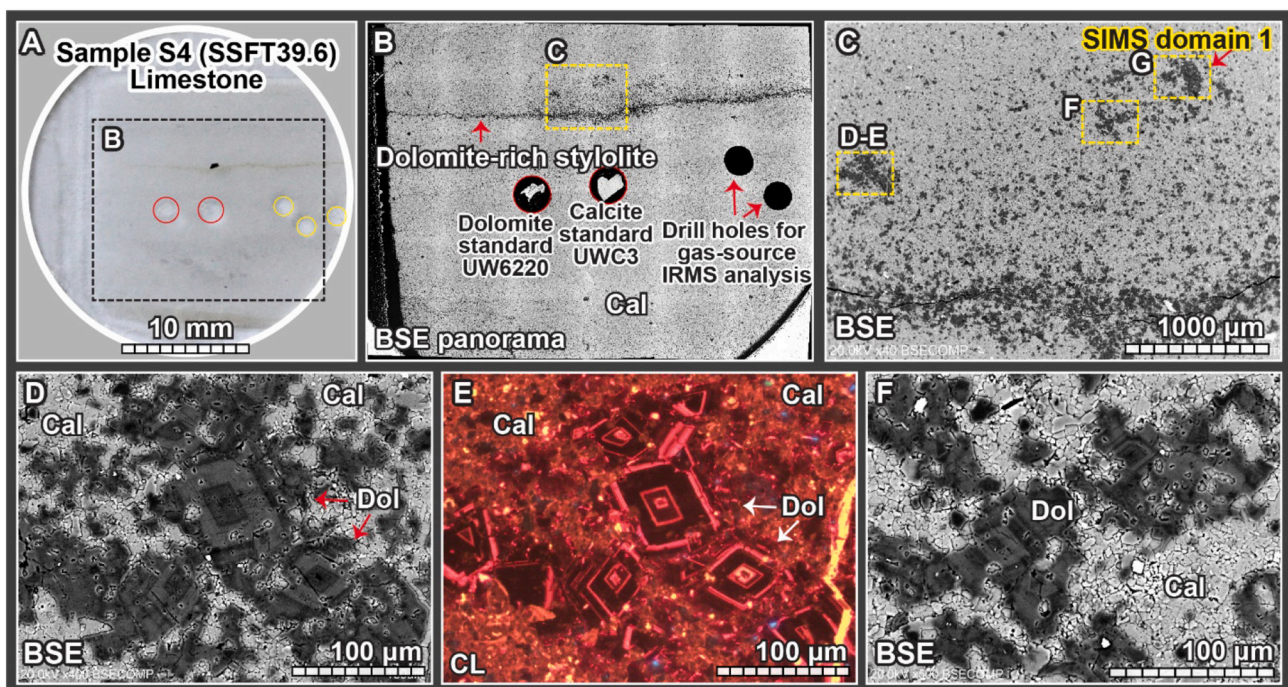
Fig. A7. Petrographic results of Sample S3 (SSFT39.0). **(A)** SIMS thin section with WiscSIMS calcite standard UWC3 and dolomite standard UW6220 mounted in the center. **(B)** BSE panorama based on the integration of 6 × 6 individual BSE images. **(C–G)** BSE images of dolomite in this sample. **(H—I)** CL images showing dolomite with dull luminescence. The lower right corner shows the SIMS dolomite standard UW6220 that was mounted in the center of the thin section before SIMS analysis. Abbreviations: BSE = backscattered electron; SEM = scanning electron microscope; CL = cathodoluminescence; Dol = dolomite.

Fig. A8. Petrographic results of Sample 4 (SSFT39.6). **(A)** SIMS thin section with WiscSIMS calcite standard UWC3 and dolomite standard UW6220 mounted in the center. The three drill holes (yellow circles) were made for gas-source IRMS analysis. **(B)** BSE panorama of the dash box in image A based on the integration of 6 × 6 individual BSE images. The upper part of this image shows a dolomite–rich stylolite. **(C, D)** BSE images showing dolomite crystals (darker color) floating in calcite matrix (brighter color). **(E)** CL image of the view in D. **(F)** BSE image of calcitic microspar matrix and zoned dolomite crystals. Abbreviations: BSE = backscattered electron; SE = secondary electron; CL = cathodoluminescence; Cal = calcite; Dol = dolomite; n.a. = not available. (For interpretation of the references to color in this figure legend, the reader is referred to the web version of this article.)
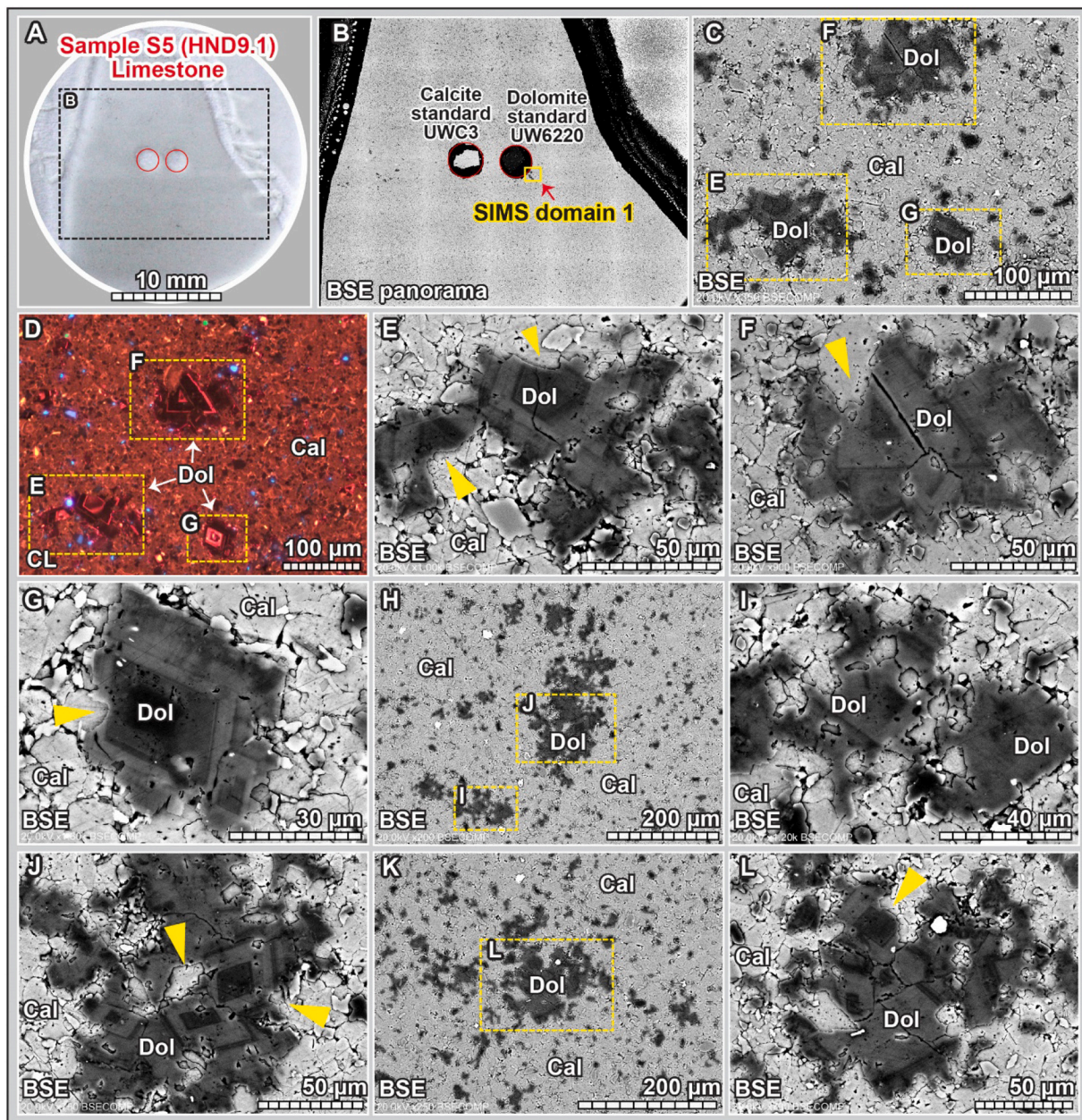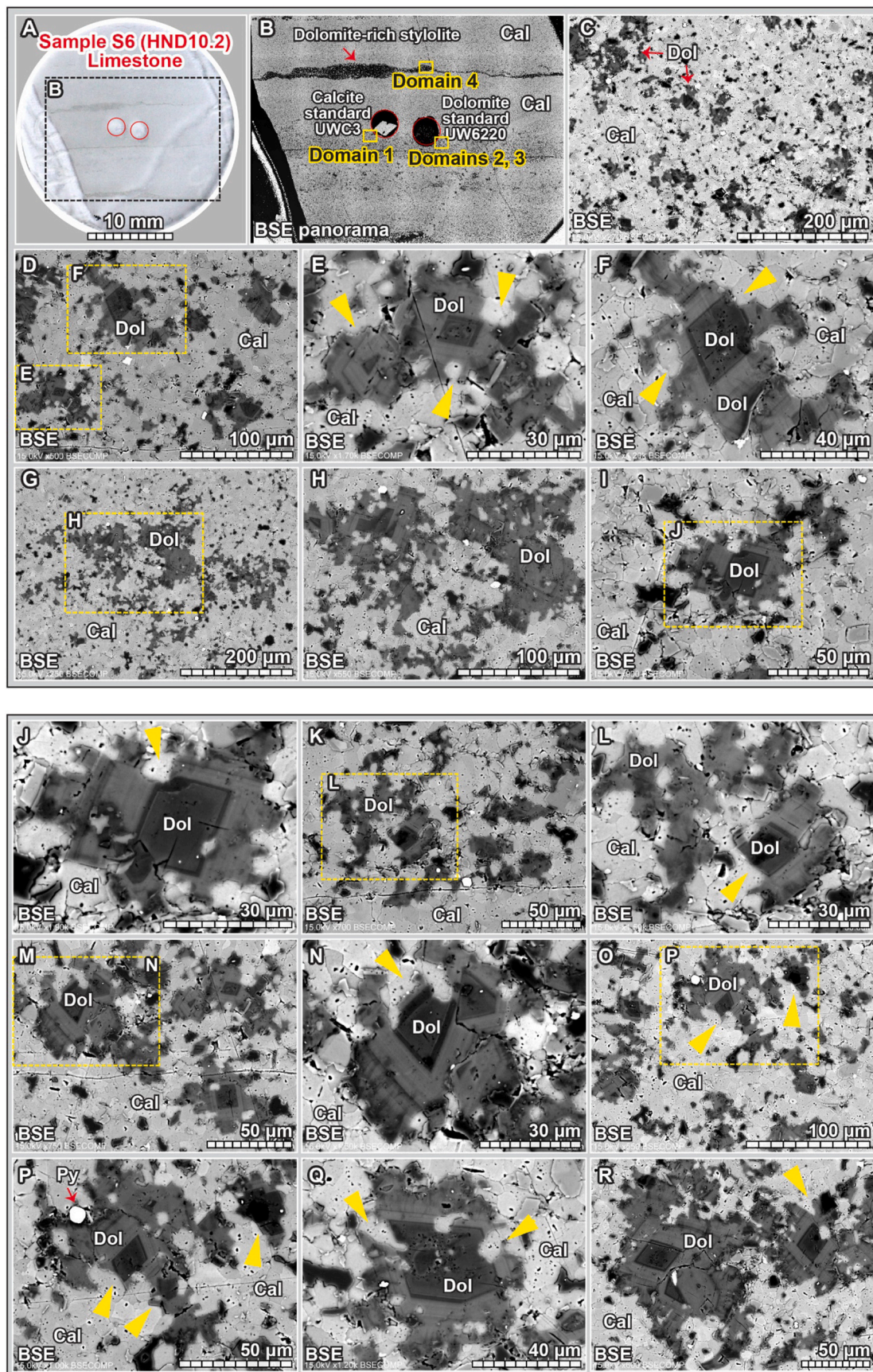
Fig. A9. Petrographic results of Sample 5 (HND9.1). **(A)** SIMS thin section with WiscSIMS calcite standard UWC3 and dolomite standard UW6220 mounted in the center. **(B)** BSE panorama based on the integration of 6 × 6 individual BSE images. **(C)** BSE images of calcite matrix and disseminated dolomite crystals. **(D)** CL image of the view in C, showing zoned dolomite crystals. **(E–L)** BSE images showing floating dolomite crystals and calcite matrix. Note that the dolomite crystals show irregular boundaries (arrows) with surrounding calcite microspar.

Fig. A10. Petrographic results of sample S6 (HND10.2). **(A)** SIMS thin section with WiscSIMS calcite standard UWC3 and dolomite standard UW6220 mounted in the center. **(B)** BSE panorama of the dash box in A based on the integration of 6 × 6 individual BSE images. **(C–R)** BSE images showing dolomite crystals in calcite matrix. Note that the dolomite crystals show irregular boundaries (arrows) with surrounding calcite microspar. Abbreviations: BSE = backscattered electron; Cal = calcite; Dol = dolomite.
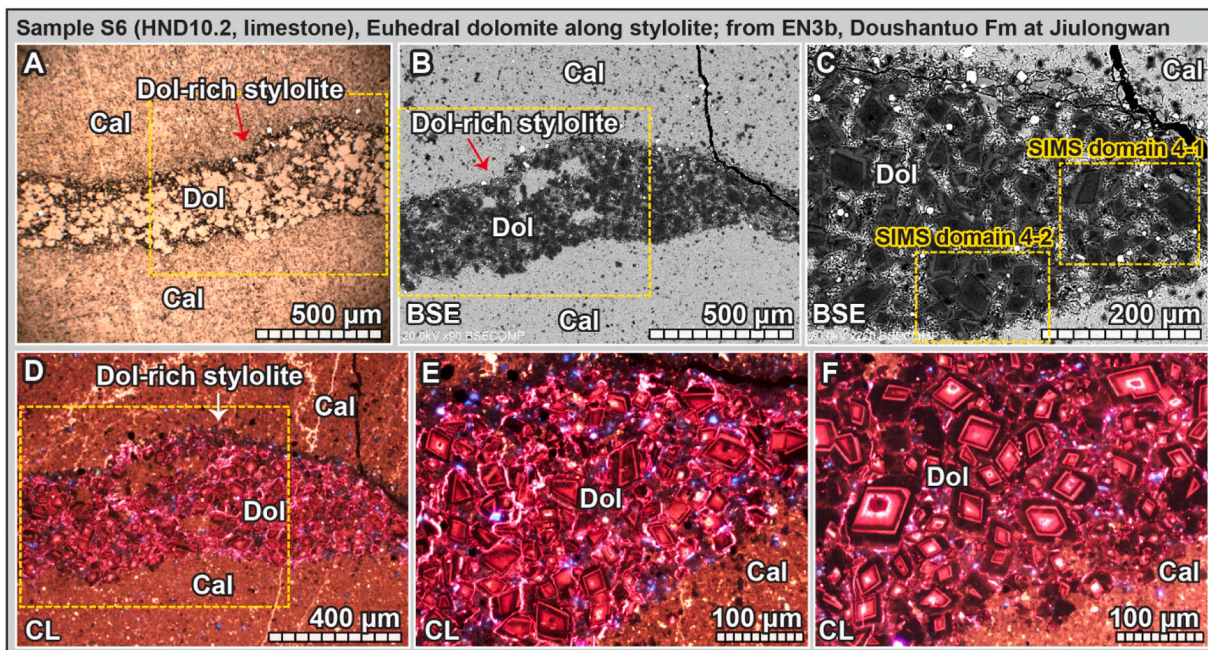
Fig. A11. Petrographic results of sample S6 (HND10.2). The dash boxes in A, B and D show the same views. **(A)** Optical microscopic image showing a dolomite–rich stylolite in a limestone sample under reflected light. **(B)** BSE image showing a dolomite–rich stylolite. **(C)** BSE image of the central right of image B. **(D-F)** CL images showing zoned dolomite crystals along stylolite.
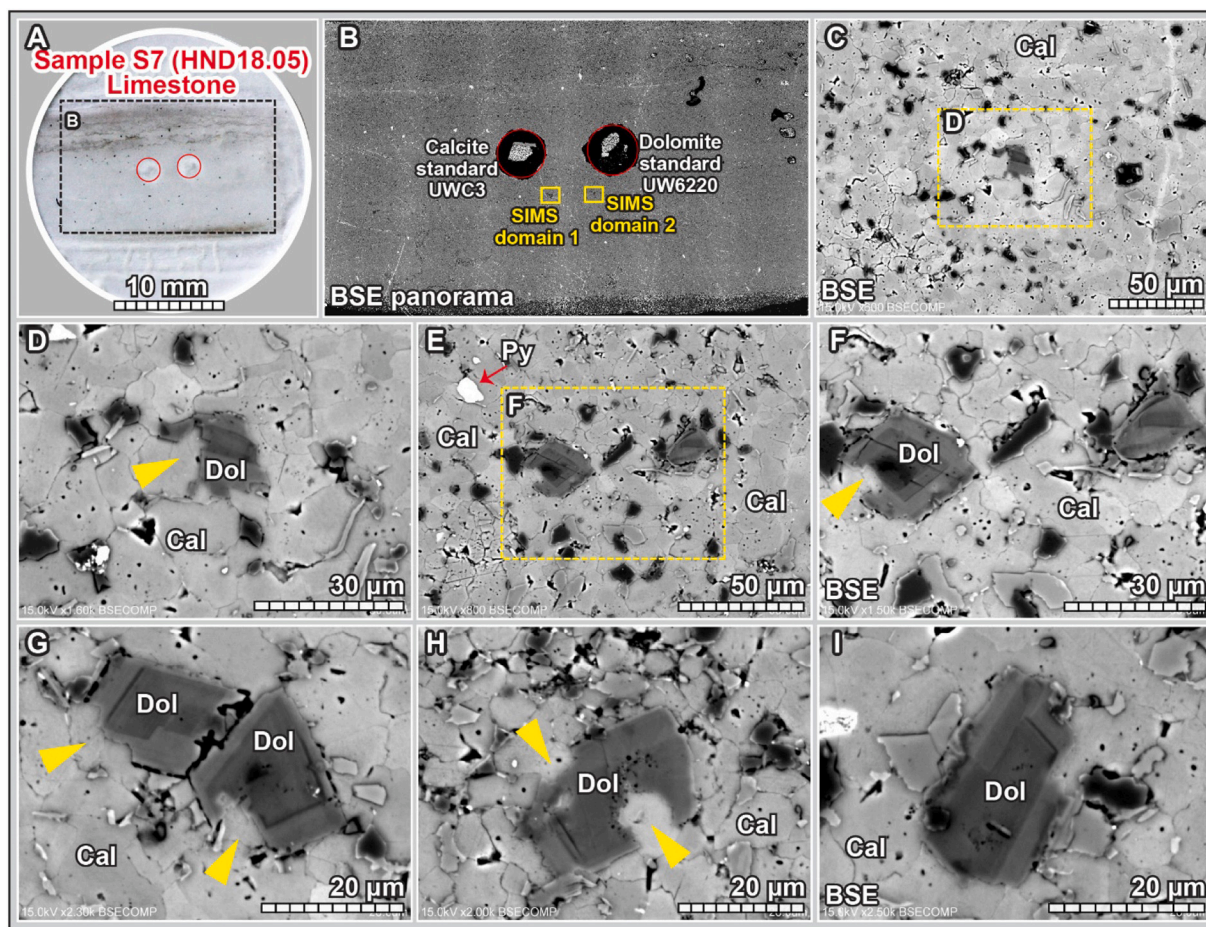
Fig. A12. Petrographic results of sample S7 (HND18.05). **(A)** SIMS thin section with WiscSIMS calcite standard UWC3 and dolomite standard UW6220 mounted in the center. **(B)** BSE panorama based on the integration of 6 × 6 individual BSE images. **(C—I)** BSE images of calcite and dolomite. Note that the dolomite crystals show irregular boundaries (arrows) with surrounding calcite microspar. Abbreviations: BSE = backscattered electron; Cal = calcite; Dol = dolomite.
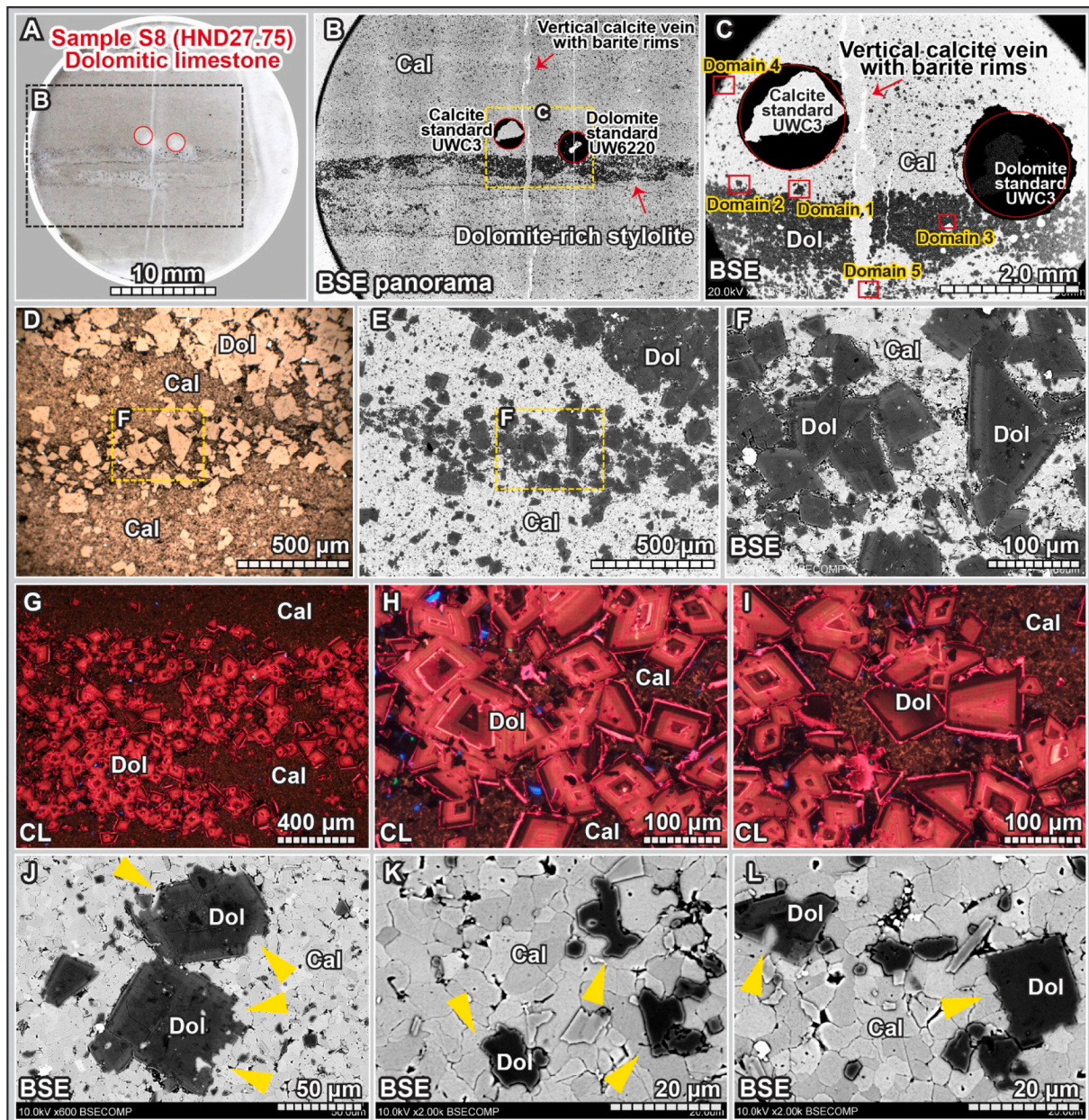
Fig. A13. Petrographic results of sample S8 (HND27.75). **(A)** SIMS thin section with WiscSIMS calcite standard UWC3 and dolomite standard UW6220 mounted in the center. **(B)** BSE panorama based on the integration of 6 × 6 individual BSE images. **(C)** A closer view of the dash box in B. Note the vertical calcite vein with barite rims. The thin barite rims are shown in the brightest color in the BSE images of this sample. **(D-F)** Petrographic images of dolomite along stylolite. **(G–I)** CL images show zoned dolomite crystals along stylolite. **(J–L)** Petrographic images of dolomite crystals in calcite matrix. Note that the dolomite crystals often show irregular boundaries (arrows) with surrounding calcite microspar. Abbreviations: BSE = backscattered electron; CL = cathodoluminescence; Cal = calcite; Dol = dolomite.
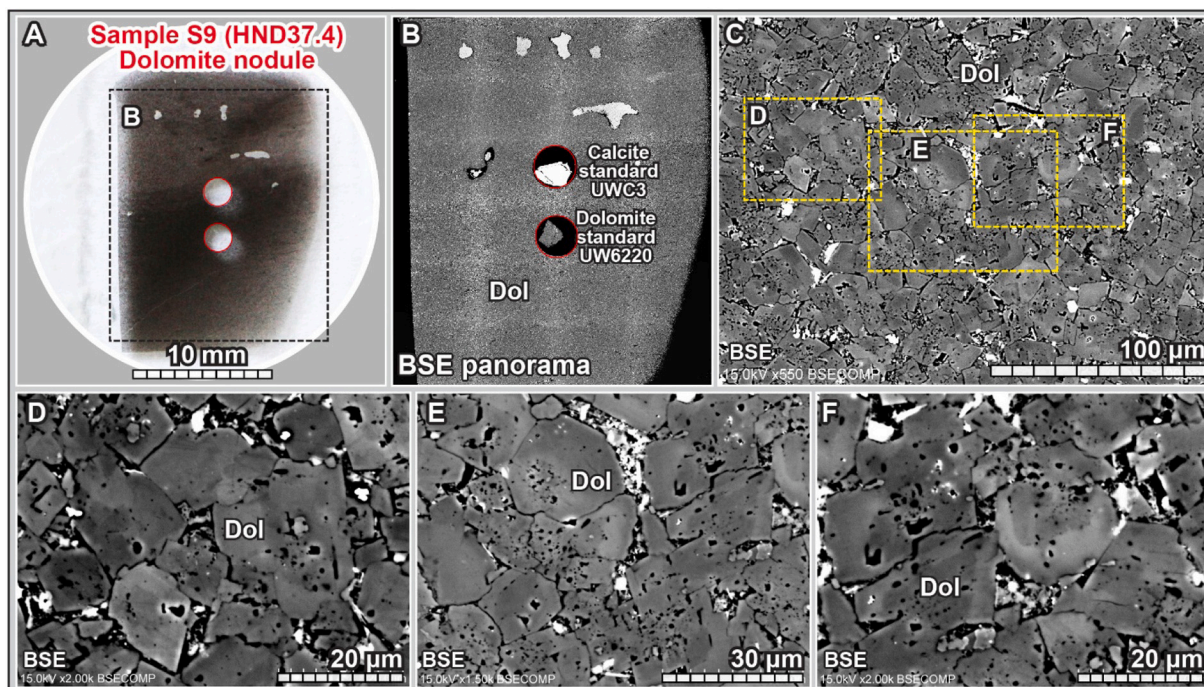
Fig. A14. Petrographic results of dolomite nodule sample S9 (HND37.4). **(A)** SIMS thin section with WiscSIMS calcite standard UWC3 and dolomite standard UW6220 mounted in the center. **(B)** BSE panorama of the dash box in image A based on the integration of 6 × 6 individual BSE images. **(C—F)** BSE images of dolomite crystals. Note the weakly zoned texture of each individual dolomite crystal. Abbreviations: BSE = backscattered electron; Dol = dolomite.
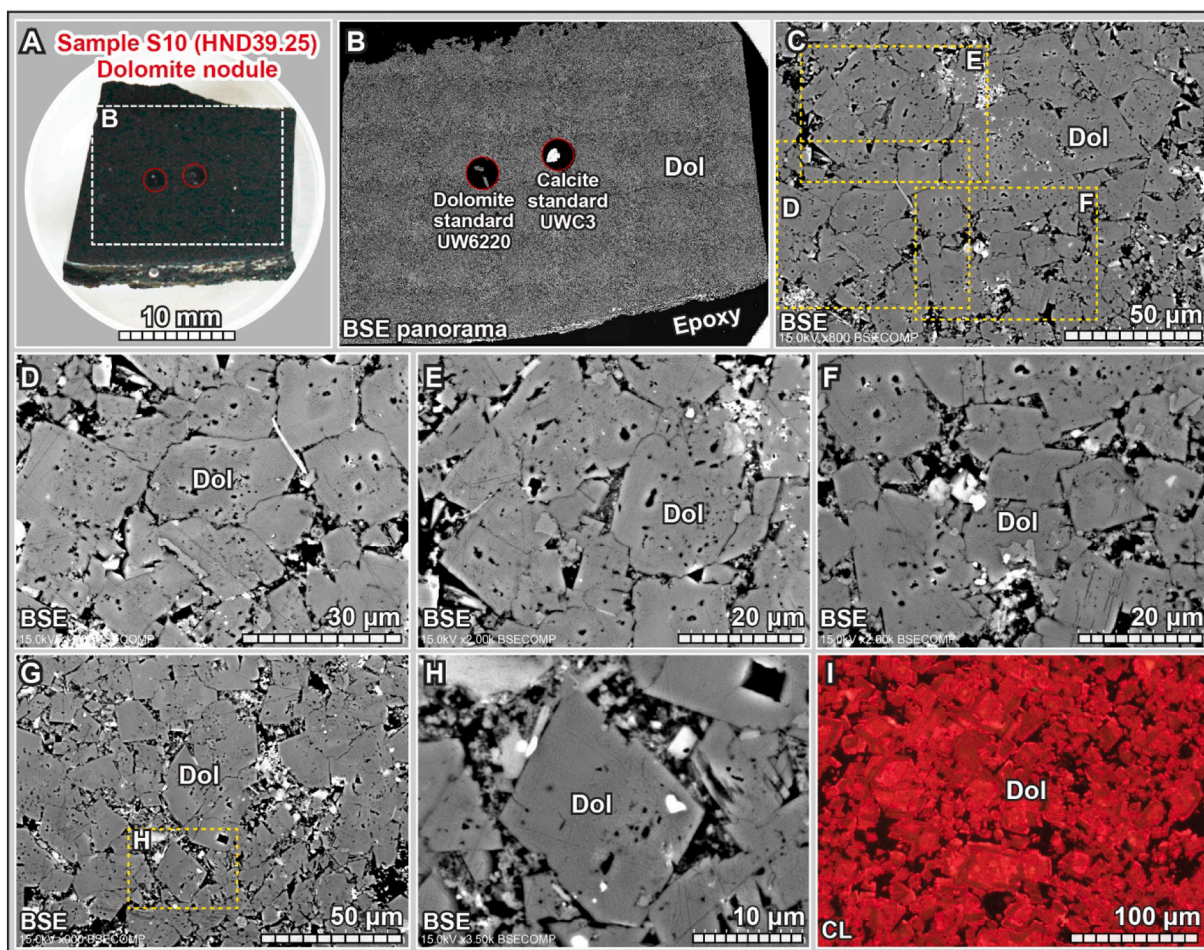

Fig. A15. Petrographic results of sample S10 (HND39.25). **(A)** SIMS thin section with WiscSIMS calcite standard UWC3 and dolomite standard UW6220 mounted in the center. **(B)** BSE panorama based on the integration of 6 × 6 individual BSE images. **(C—H)** BSE images showing euhedral to subhedral dolomite crystals. **(I)** CL image showing weakly zoned dolomite crystals. Abbreviations: BSE = backscattered electron; CL = cathodoluminescence; Cal = calcite; Dol = dolomite.

Appendix A. Supplementary data

Supplementary data to this article can be found online at https://doi.org/10.1016/j.gloplacha.2021.103591.

References

Ader, M., Macouin, M., Trindade, R.I.F., Hadrien, M.-H., Yang, Z., Sun, Z., Besse, J., 2009. A multilayered water column in the Ediacaran Yangtze platform? Insights from carbonate and organic matter paired $\delta^{13}C$. Earth Planet. Sci. Lett. 288, 213–227. https://doi.org/10.1016/j.epsl.2009.09.024.

Allan, J.R., Matthews, R.K., 1982. Isotope signatures associated with early meteoric diagenesis. Sedimentology 29, 797–817. https://doi.org/10.1111/j.1365-3091.1982.tb00085.x.

An, Z., Jiang, G., Tong, J., Tian, L., Ye, Q., Song, H., Song, H., 2015. Stratigraphic position of the Ediacaran Miaohe biota and its constrains on the age of the upper Doushantuo $\delta^{13}C$ anomaly in the Yangtze Gorges area, South China. Precambrian Res. 271, 243–253. https://doi.org/10.1016/j.precamres.2015.10.007.

Andrieu, S., Brigaud, B., Barbarand, J., Lasseur, E., 2017. The complex diagenetic history of discontinuities in shallow-marine carbonate rocks: new insights from high-resolution ion microprobe investigation of $\delta^{18}O$ and $\delta^{13}C$ of early cements. Sedimentology 65, 360–399. https://doi.org/10.1111/sed.12384.

Barale, L., Bertok, C., Salih Talabani, N., d'Atri, A., Martire, L., Piana, F., Préat, A., 2016. Very hot, very shallow hydrothermal dolomitization: an example from the Maritime Alps (north-West Italy–south-east France). Sedimentology 63, 2037–2065. https://doi.org/10.1111/sed.12294.

Biehl, B.C., Reuning, L., Schoenherr, J., Lüders, V., Kukla, P.A., 2016. Impacts of hydrothermal dolomitization and thermochemical sulfate reduction on secondary porosity creation in deeply buried carbonates: a case study from the Lower Saxony Basin, Northwest Germany. AAPG Bull. 100, 597–621. https://doi.org/10.1306/01141615055.

Bishop, J.W., Osleger, D.A., Montañez, I.P., Sumner, D.Y., 2014. Meteoric diagenesis and fluid-rock interaction in the Middle Permian Capitan backreef: Yates Formation, Slaughter Canyon, New Mexico. AAPG Bull. 98, 1495–1519. https://doi.org/10.1306/05201311158.

Bjerrum, C.J., Canfield, D.E., 2011. Towards a quantitative understanding of the late Neoproterozoic carbon cycle. Proc. Natl. Acad. Sci. 108, 5542–5547. https://doi.org/10.1073/pnas.1101755108.

Bristow, T.F., Bonifacie, M., Derkowski, A., Eiler, J.M., Grotzinger, J.P., 2011. A hydrothermal origin for isotopically anomalous cap dolostone cements from South China. Nature 474, 68–71. https://doi.org/10.1038/nature10096.

Burns, S.J., Matter, A., 1993. Carbon isotopic record of the latest Proterozoic from Oman. Eclogae Geol. Helv. 86, 595–607. https://doi.org/10.5169/seals-167254.

Cai, Y., Hua, H., Xiao, S., Schiffbauer, J.D., Li, P., 2010. Biostratinomy of the late Ediacaran pyritized Gaojiashan Lagerstätte from southern Shaanxi, South China: Importance of event deposits. PALAIOS 25, 487–506. https://doi.org/10.2110/palo.2009.p09-133r.

Calver, C.R., 2000. Isotope stratigraphy of the Ediacarian (Neoproterozoic III) of the Adelaide Rift Complex, Australia, and the overprint of water column stratification. Precambrian Res. 100, 121–150. https://doi.org/10.1016/s0301-9268(99)00072-8.

Chang, B., Li, C., Liu, D., Foster, I., Tripati, A., Lloyd, M.K., Maradiaga, I., Luo, G., An, Z., She, Z., Xie, S., Tong, J., Huang, J., Algeo, T.J., Lyons, T.W., Immenhauser, A., 2020. Massive formation of early diagenetic dolomite in the Ediacaran Ocean: Constraints on the "dolomite problem". Proc. Natl. Acad. Sci. 117, 14005–14014. https://doi.org/10.1073/pnas.1916673117.

Chen, Z., Zhou, C., Meyer, M., Xiang, K., Schiffbauer, J.D., Yuan, X., Xiao, S., 2013. Trace fossil evidence for Ediacaran bilaterian animals with complex behaviors. Precambrian Res. 224, 690–701. https://doi.org/10.1016/j.precamres.2012.11.004.

Chen, Z., Zhou, C., Xiao, S., Wang, W., Guan, C., Hua, H., Yuan, X., 2014. New Ediacara fossils preserved in marine limestone and their ecological implications. Sci. Rep. 4, 4180. https://doi.org/10.1038/srep04180.

Condon, D., Zhu, M., Bowring, S., Wang, W., Yang, A., Jin, Y., 2005. U–Pb ages from the Neoproterozoic Doushantuo Formation, China. Science 308, 95–98. https://doi.org/10.1126/science.1107765.

Cui, H., 2021. Inside out: deep carbon linked to deep-time carbon cycle. Sci. Bull. https://doi.org/10.1016/j.scib.2021.06.001. In press.

Cui, H., Kaufman, A.J., Xiao, S., Zhou, C., Zhu, M., 2013. Was the Shuram Carbon Isotope Anomaly Driven by an Oxidative Pulse of Alkalinity and Sulfate to the Ediacaran Ocean?, Geological Society of America Annual Meeting in Denver: 125th Anniversary of GSA. Geological Society of America, Denver, Colorado, USA, p. 700.

Cui, H., Kaufman, A.J., Xiao, S., Zhu, M., Zhou, C., Liu, X.-M., 2015. Redox architecture of an Ediacaran Ocean margin: integrated chemostratigraphic ($\delta^{13}C-\delta^{34}S-^{87}Sr/^{86}Sr-Ce/Ce^*$) correlation of the Doushantuo Formation, South China. Chem. Geol. 405, 48–62. https://doi.org/10.1016/j.chemgeo.2015.04.009.

Cui, H., Kaufman, A.J., Xiao, S., Peek, S., Cao, H., Min, X., Cai, Y., Siegel, Z., Liu, X.M., Peng, Y., Schiffbauer, J.D., Martin, A.J., 2016a. Environmental context for the terminal Ediacaran biomineralization of animals. Geobiology 14, 344–363. https://doi.org/10.1111/gbi.12178.

Cui, H., Xiao, S., Zhou, C., Peng, Y., Kaufman, A.J., Plummer, R.E., 2016b. Phosphogenesis associated with the Shuram Excursion: petrographic and geochemical observations from the Ediacaran Doushantuo Formation of South China. Sediment. Geol. 341, 134–146. https://doi.org/10.1016/j.sedgeo.2016.05.008.

Cui, H., Kaufman, A.J., Xiao, S., Zhou, C., Liu, X.-M., 2017. Was the Ediacaran Shuram Excursion a globally synchronized early diagenetic event? Insights from methane-derived authigenic carbonates in the uppermost Doushantuo Formation, South China. Chem. Geol. 450, 59–80. https://doi.org/10.1016/j.chemgeo.2016.12.010.

Cui, H., Orland, I.J., Denny, A., Kitajima, K., Fournelle, J.H., Baele, J.-M., de Winter, N.J., Goderis, S., Claeys, P., Valley, J.W., 2019a. Ice or fire? Constraining the origin of isotopically anomalous cap carbonate cements by SIMS, Geological Society of America Abstracts with Programs, Vol. 51. https://doi.org/10.1130/abs/2019AM-332456. No. 5, Phoenix, Arizona, USA.

Cui, H., Xiao, S., Cai, Y., Peek, S., Plummer, R.E., Kaufman, A.J., 2019b. Sedimentology and chemostratigraphy of the terminal Ediacaran Dengying Formation at the Gaojiashan section, South China. Geol. Mag. 156, 1924–1948. https://doi.org/10.1017/S0016756819000293.

Cunningham, J.A., Vargas, K., Yin, Z., Bengtson, S., Donoghue, P.C.J., 2017. The Weng'an Biota (Doushantuo Formation): an Ediacaran window on soft-bodied and multicellular microorganisms. J. Geol. Soc. 174, 793–802. https://doi.org/10.1144/jgs2016-142.

Darroch, S.A.F., Smith, E.F., Laflamme, M., Erwin, D.H., 2018. Ediacaran Extinction and Cambrian Explosion. Trends Ecol. Evol. 33, 653–663. https://doi.org/10.1016/j.tree.2018.06.003.

Davies, G.R., Smith Jr., L.B., 2006. Structurally controlled hydrothermal dolomite reservoir facies: An overview. AAPG Bull. 90, 1641–1690. https://doi.org/10.1306/05220605164.

Denny, A.C., Kozdon, R., Kitajima, K., Valley, J.W., 2017. Isotopically zoned carbonate cements in Early Paleozoic sandstones of the Illinois Basin: $\delta^{18}O$ and $\delta^{13}C$ records of burial and fluid flow. Sediment. Geol. 361, 93–110. https://doi.org/10.1016/j.sedgeo.2017.09.004.

Denny, A.C., Orland, I.J., Valley, J.W., 2020. Regionally correlated oxygen and carbon isotope zonation in diagenetic carbonates of the Bakken Formation. Chem. Geol. 531, 119327. https://doi.org/10.1016/j.chemgeo.2019.119327.

Derry, L.A., 2010. A burial diagenesis origin for the Ediacaran Shuram–Wonoka carbon isotope anomaly. Earth Planet. Sci. Lett. 294, 152–162. https://doi.org/10.1016/j.epsl.2010.03.022.

Donovan, J.J., Tingle, T.N., 1996. An improved mean atomic number background correction for quantitative microanalysis. Microsc. Microanal. 2, 1–7.

Donovan, J.J., Kremser, D., Fournelle, J., Goemann, K., 2018. Probe for Windows User's Guide and Reference, Enterprise edition. Probe Software, Inc., Eugene, OR.

Feng, M., Wu, P., Qiang, Z., Liu, X., Duan, Y., Xia, M., 2017. Hydrothermal dolomite reservoir in the Precambrian Dengying Formation of Central Sichuan Basin, Southwestern China. Mar. Pet. Geol. 82, 206–219. https://doi.org/10.1016/j.marpetgeo.2017.02.008.

Fike, D.A., Grotzinger, J.P., Pratt, L.M., Summons, R.E., 2006. Oxidation of the Ediacaran Ocean. Nature 444, 744–747. https://doi.org/10.1038/nature05345.

Grotzinger, J.P., Fike, D.A., Fischer, W.W., 2011. Enigmatic origin of the largest-known carbon isotope excursion in Earth's history. Nat. Geosci. 4, 285–292. https://doi.org/10.1038/ngeo1138.

Hayes, J.M., 1993. Factors controlling ^{13}C contents of sedimentary organic compounds: Principles and evidence. Mar. Geol. 113, 111–125. https://doi.org/10.1016/0025-3227(93)90153-m.

Hu, Y., Cai, C., Pederson, C.L., Liu, D., Jiang, L., He, X., Shi, S., Immenhauser, A., 2020. Dolomitization history and porosity evolution of a giant, deeply buried Ediacaran gas field (Sichuan Basin, China). Precambrian Res. 338, 105595. https://doi.org/10.1016/j.precamres.2020.105595.

Hua, H., Chen, Z., Yuan, X., 2007. The advent of mineralized skeletons in Neoproterozoic Metazoa—new fossil evidence from the Gaojiashan Fauna. Geol. J. 42, 263–279. https://doi.org/10.1002/gj.1077.

Husson, J.M., Maloof, A.C., Schoene, B., 2012. A syn-depositional age for Earth's deepest $\delta^{13}C$ excursion required by isotope conglomerate tests. Terra Nova 24, 318–325. https://doi.org/10.1111/j.1365-3121.2012.01067.x.

Husson, J.M., Higgins, J.A., Maloof, A.C., Schoene, B., 2015a. Ca and Mg isotope constraints on the origin of Earth's deepest C excursion. Geochim. Cosmochim. Acta 160, 243–266. https://doi.org/10.1016/j.gca.2015.03.012.

Husson, J.M., Maloof, A.C., Schoene, B., Chen, C.Y., Higgins, J.A., 2015b. Stratigraphic expression of Earth's deepest $\delta^{13}C$ excursion in the Wonoka Formation of South Australia. Am. J. Sci. 315, 1–45. https://doi.org/10.2475/01.2015.01.

Husson, J.M., Linzmeier, B.J., Kitajima, K., Ishida, A., Maloof, A.C., Schoene, B., Peters, S.E., Valley, J.W., 2020. Large isotopic variability at the micron-scale in 'Shuram' excursion carbonates from South Australia. Earth Planet. Sci. Lett. 538, 116211. https://doi.org/10.1016/j.epsl.2020.116211.

Jiang, G., Kennedy, M.J., Christie-Blick, N., 2003. Stable isotopic evidence for methane seeps in Neoproterozoic postglacial cap carbonates. Nature 426, 822–826. https://doi.org/10.1038/nature02201.

Jiang, G., Kennedy, M.J., Christie-Blick, N., Wu, H., Zhang, S., 2006. Stratigraphy, sedimentary structures, and textures of the late Neoproterozoic Doushantuo cap carbonate in South China. J. Sediment. Res. 76, 978–995. https://doi.org/10.2110/jsr.2006.086.

Jiang, G., Kaufman, A.J., Christie-Blick, N., Zhang, S., Wu, H., 2007. Carbon isotope variability across the Ediacaran Yangtze platform in South China: Implications for a

large surface-to-deep ocean δ¹³C gradient. Earth Planet. Sci. Lett. 261, 303–320. https://doi.org/10.1016/j.epsl.2007.07.009.

Jiang, G., Shi, X., Zhang, S., Wang, Y., Xiao, S., 2011. Stratigraphy and paleogeography of the Ediacaran Doushantuo Formation (ca. 635–551Ma) in South China. Gondwana Res. 19, 831–849. https://doi.org/10.1016/j.gr.2011.01.006.

Jiang, Y., Tao, Y., Gu, Y., Wang, J., Qiang, Z., Jiang, N., Lin, G., Jiang, C., 2016. Hydrothermal dolomitization in Dengying Formation, Gaoshiti-Moxi area, Sichuan Basin, SW China. Pet. Explor. Dev. 43, 54–64. https://doi.org/10.1016/S1876-3804(16)30006-4.

Jiang, L., Planavsky, N., Zhao, M., Liu, W., Wang, X., 2019. Authigenic origin for a massive negative carbon isotope excursion. Geology 47, 115–118. https://doi.org/10.1130/G45709.1.

Johnston, D.T., Macdonald, F.A., Gill, B.C., Hoffman, P.F., Schrag, D.P., 2012. Uncovering the Neoproterozoic carbon cycle. Nature 483, 320–323. https://doi.org/10.1038/nature10854.

Kaufman, A.J., Corsetti, F.A., Varni, M.A., 2007. The effect of rising atmospheric oxygen on carbon and sulfur isotope anomalies in the Neoproterozoic Johnnie Formation, Death Valley, USA. Chem. Geol. 237, 47–63. https://doi.org/10.1016/j.chemgeo.2006.06.023.

Kim, Y., Lee, Y.I., 2003. Radiaxial fibrous calcites as low-magnesian calcite cement precipitated in a marine-meteoric mixing zone. Sedimentology 50, 731–742. https://doi.org/10.1046/j.1365-3091.2003.00573.x.

Knauth, L.P., Kennedy, M.J., 2009. The late Precambrian greening of the Earth. Nature 460, 728–732. https://doi.org/10.1038/nature08213.

Koeshidayatullah, A., Corlett, H., Stacey, J., Swart, P.K., Boyce, A., Hollis, C., 2020. Origin and evolution of fault-controlled hydrothermal dolomitization fronts: a new insight. Earth Planet. Sci. Lett. 541, 116291. https://doi.org/10.1016/j.epsl.2020.116291.

Kozdon, R., Ushikubo, T., Kita, N.T., Spicuzza, M., Valley, J.W., 2009. Intratest oxygen isotope variability in the planktonic foraminifer *N. pachyderma*: real vs. apparent vital effects by ion microprobe. Chem. Geol. 258, 327–337. https://doi.org/10.1016/j.chemgeo.2008.10.032.

Kump, L.R., Arthur, M.A., 1999. Interpreting carbon-isotope excursions: carbonates and organic matter. Chem. Geol. 161, 181–198. https://doi.org/10.1016/s0009-2541(99)00086-8.

Li, C., Hardisty, D.S., Luo, G., Huang, J., Algeo, T.J., Cheng, M., Shi, W., An, Z., Tong, J., Xie, S., Jiao, N., Lyons, T.W., 2017. Uncovering the spatial heterogeneity of Ediacaran carbon cycling. Geobiology 15, 211–224. https://doi.org/10.1111/gbi.12222.

Li, Z., Cao, M., Loyd, S.J., Algeo, T.J., Zhao, H., Wang, X., Zhao, L., Chen, Z.-Q., 2020. Transient and stepwise ocean oxygenation during the late Ediacaran Shuram Excursion: Insights from carbonate δ²³⁸U of northwestern Mexico. Precambrian Res. 344, 105741. https://doi.org/10.1016/j.precamres.2020.105741.

Liang, D., Cai, Y., Nolan, M., Xiao, S., 2020. The terminal Ediacaran tubular fossil *Cloudina* in the Yangtze Gorges area of South China. Precambrian Res. 351, 105931. https://doi.org/10.1016/j.precamres.2020.105931.

Lin, Z., Wang, Q., Feng, D., Liu, Q., Chen, D., 2011. Post-depositional origin of highly ¹³C-depleted carbonate in the Doushantuo cap dolostone in South China: Insights from petrography and stable carbon isotopes. Sediment. Geol. 242, 71–79. https://doi.org/10.1016/j.sedgeo.2011.10.009.

Ling, H.-F., Chen, X., Li, D., Wang, D., Shields-Zhou, G.A., Zhu, M., 2013. Cerium anomaly variations in Ediacaran–earliest Cambrian carbonates from the Yangtze Gorges area, South China: Implications for oxygenation of coeval shallow seawater. Precambrian Res. 225, 110–127. https://doi.org/10.1016/j.precamres.2011.10.011.

Liu, P., Moczydłowska, M., 2019. Ediacaran microfossils from the Doushantuo Formation chert nodules in the Yangtze Gorges area, South China, and new biozones. Fossils Strata 65, 1–172. https://doi.org/10.1002/9781119564225.ch1.

Liu, P., Xiao, S., Yin, C., Chen, S., Zhou, C., Li, M., 2014. Ediacaran acanthomorphic acritarchs and other microfossils from chert nodules of the upper Doushantuo Formation in the Yangtze Gorges area, South China. J. Paleontol. 88, 1–139. https://doi.org/10.1666/13-009.

Liu, Y., Chen, W., Foley, S.F., Shen, Y., Chen, C., Li, J., Ou, X., He, D., Feng, Q., Lin, J., 2021. The largest negative carbon isotope excursions in neoproterozoic carbonates caused by recycled carbonatite volcanic ash. Sci. Bull. https://doi.org/10.1016/j.scib.2021.04.021.

Lu, M., Zhu, M., Zhang, J., Shields-Zhou, G., Li, G., Zhao, F., Zhao, X., Zhao, M., 2013. The DOUNCE event at the top of the Ediacaran Doushantuo Formation, South China: Broad stratigraphic occurrence and non-diagenetic origin. Precambrian Res. 225, 86–109. https://doi.org/10.1016/j.precamres.2011.10.018.

McFadden, K.A., Huang, J., Chu, X., Jiang, G., Kaufman, A.J., Zhou, C., Yuan, X., Xiao, S., 2008. Pulsed oxidation and biological evolution in the Ediacaran Doushantuo Formation. Proc. Natl. Acad. Sci. 105, 3197–3202. https://doi.org/10.1073/pnas.0708336105.

Meyer, M., Xiao, S., Gill, B.C., Schiffbauer, J.D., Chen, Z., Zhou, C., Yuan, X., 2014. Interactions between Ediacaran animals and microbial mats: Insights from Lamonte trevallis, a new trace fossil from the Dengying Formation of South China. Palaeogeogr. Palaeoclimatol. Palaeoecol. 396, 62–74. https://doi.org/10.1016/j.palaeo.2013.12.026.

Narbonne, G.M., Xiao, S., Shields, G.A., Gehling, J.G., 2012. The Ediacaran Period. In: Gradstein, F.M., Ogg, J.G., Schmitz, M.D., Ogg, G.M. (Eds.), The Geologic Time Scale. Elsevier, Boston, USA, pp. 413–435. https://doi.org/10.1016/b978-0-444-59425-9.00018-4.

Ouyang, Q., Guan, C., Zhou, C., Xiao, S., 2017. Acanthomorphic acritarchs of the Doushantuo Formation from an upper slope section in northwestern Hunan Province, South China, with implications for early–middle Ediacaran

biostratigraphy. Precambrian Res. 298, 512–529. https://doi.org/10.1016/j.precamres.2017.07.005.

Ouyang, Q., Zhou, C., Xiao, S., Chen, Z., Shao, Y., 2019. Acanthomorphic acritarchs from the Ediacaran Doushantuo Formation at Zhangcunping in South China, with implications for the evolution of early Ediacaran eukaryotes. Precambrian Res. 320, 171–192. https://doi.org/10.1016/j.precamres.2018.10.012.

Ouyang, Q., Zhou, C., Xiao, S., Guan, C., Chen, Z., Yuan, X., Sun, Y., 2021. Distribution of Ediacaran acanthomorphic acritarchs in the lower Doushantuo Formation of the Yangtze Gorges area, South China: evolutionary and stratigraphic implications. Precambrian Res. 353, 106005. https://doi.org/10.1016/j.precamres.2020.106005.

Paulsen, T., Deering, C., Sliwinski, J., Bachmann, O., Guillong, M., 2017. Evidence for a spike in mantle carbon outgassing during the Ediacaran period. Nat. Geosci. 10, 930–934. https://doi.org/10.1038/s41561-017-0011-6.

Rooney, A.D., Cantine, M.D., Bergmann, K.D., Gómez-Pérez, I., Al Baloushi, B., Boag, T. H., Busch, J.F., Sperling, E.A., Strauss, J.V., 2020. Calibrating the coevolution of Ediacaran life and environment. Proc. Natl. Acad. Sci. 117, 16824–16830. https://doi.org/10.1073/pnas.2002918117.

Rothman, D.H., Hayes, J.M., Summons, R.E., 2003. Dynamics of the Neoproterozoic carbon cycle. Proc. Natl. Acad. Sci. 100, 8124–8129. https://doi.org/10.1073/pnas.0832439100.

Schmitz, M.D., 2012. Radiometric ages used in GTS2012. In: Gradstein, F.M., Ogg, J.G., Schmitz, M.D., Ogg, G.M. (Eds.), The Geologic Time Scale. Elsevier, Boston, pp. 1045–1082. https://doi.org/10.1016/b978-0-444-59425-9.15002-4.

Scholle, P.A., Ulmer-Scholle, D.S., 2003. A Color Guide to the Petrography of Carbonate Rocks: Grains, Textures, Porosity, Diagenesis, AAPG Memoir 77, 77. AAPG.

Schrag, D.P., Higgins, J.A., Macdonald, F.A., Johnston, D.T., 2013. Authigenic carbonate and the history of the global carbon cycle. Science 339, 540–543. https://doi.org/10.1126/science.1229578.

Shi, W., Li, C., Luo, G., Huang, J., Algeo, T.J., Jin, C., Zhang, Z., Cheng, M., 2018. Sulfur isotope evidence for transient marine-shelf oxidation during the Ediacaran Shuram Excursion. Geology 46, 267–270. https://doi.org/10.1130/g39663.1.

Shields, G.A., Mills, B.J.W., Zhu, M., Raub, T.D., Daines, S.J., Lenton, T.M., 2019. Unique Neoproterozoic carbon isotope excursions sustained by coupled evaporite dissolution and pyrite burial. Nat. Geosci. 12, 823–827. https://doi.org/10.1038/s41561-019-0434-3.

Śliwiński, M.G., Kitajima, K., Kozdon, R., Spicuzza, M.J., Fournelle, J.H., Denny, A., Valley, J.W., 2016a. Secondary ion mass spectrometry bias on isotope ratios in dolomite–ankerite, Part II: δ¹³C matrix effects. Geostand. Geoanal. Res. 40, 173–184. https://doi.org/10.1111/1751-908X.2015.00380.x.

Śliwiński, M.G., Kozdon, R., Kitajima, K., Valley, J.W., Denny, A., 2016b. Microanalysis of carbonate cement δ¹⁸O in a CO₂-storage system seal: insights into the diagenetic history of the Eau Claire Formation (Upper Cambrian), Illinois Basin. AAPG Bull. 1003–1031. https://doi.org/10.1306/02031615065.

Śliwiński, M.G., Kitajima, K., Kozdon, R., Spicuzza, M.J., Denny, A., Valley, J.W., 2017. In situ δ¹³C and δ¹⁸O microanalysis by SIMS: a method for characterizing the carbonate components of natural and engineered CO2-reservoirs. Int. J. Greenhouse Gas Control 57, 116–133. https://doi.org/10.1016/j.ijggc.2016.12.013.

Tahata, M., Ueno, Y., Ishikawa, T., Sawaki, Y., Murakami, K., Han, J., Shu, D., Li, Y., Guo, J., Yoshida, N., Komiya, T., 2013. Carbon and oxygen isotope chemostratigraphies of the Yangtze platform, South China: decoding temperature and environmental changes through the Ediacaran. Gondwana Res. 23, 333–353. https://doi.org/10.1016/j.gr.2012.04.005.

Tucker, M.E., Bathurst, R.G.C., 1990. Carbonate Diagenesis, 1. Blackwell Scientific Publications.

Tucker, M.E., Wright, V.P., Dickson, J.A.D., 2009. Carbonate Sedimentology. Blackwell Scientific Publications, Oxford.

Valley, J.W., Kita, N.T., 2009. In situ oxygen isotope geochemistry by ion microprobe. In: Fayek, M. (Ed.), Secondary Ion Mass Spectrometry in the Earth Sciences – Gleaning the Big Picture from a Small Spot. Mineralogical Association of Canada Short Course 41, Toronto, pp. 19–63.

Wang, J., Jiang, G., Xiao, S., Li, Q., Wei, Q., 2008. Carbon isotope evidence for widespread methane seeps in the ca. 635 Ma Doushantuo cap carbonate in South China. Geology 36, 347–350. https://doi.org/10.1130/g24513a.1.

Wang, X., Jiang, G., Shi, X., Xiao, S., 2016. Paired carbonate and organic carbon isotope variations of the Ediacaran Doushantuo Formation from an upper slope section at Siduping, South China. Precambrian Res. 273, 53–66. https://doi.org/10.1016/j.precamres.2015.12.010.

Wycech, J.B., Kelly, D.C., Kozdon, R., Orland, I.J., Spero, H.J., Valley, J.W., 2018. Comparison of δ¹⁸O analyses on individual planktic foraminifer (Orbulina universa) shells by SIMS and gas-source mass spectrometry. Chem. Geol. 483, 119–130. https://doi.org/10.1016/j.chemgeo.2018.02.028.

Xiao, S., Narbonne, G.M., 2020. The Ediacaran period. In: Gradstein, F.M., Ogg, J.G., Schmitz, M.D., Ogg, G.M. (Eds.), Geologic Time Scale 2020. Elsevier, pp. 521–561. https://doi.org/10.1016/B978-0-12-824360-2.00018-8.

Xiao, S., Zhang, Y., Knoll, A.H., 1998. Three-dimensional preservation of algae and animal embryos in a Neoproterozoic phosphorite. Nature 391, 553–558. https://doi.org/10.1038/35318.

Xiao, S., Shen, B., Zhou, C., Xie, G., Yuan, X., 2005. A uniquely preserved Ediacaran fossil with direct evidence for a quilted bodyplan. Proc. Natl. Acad. Sci. U. S. A. 102, 10227–10232. https://doi.org/10.1073/pnas.0502176102.

Xiao, S., Zhou, C., Liu, P., Wang, D., Yuan, X., 2014. Phosphatized acanthomorphic acritarchs and related microfossils from the Ediacaran Doushantuo Formation at Weng'an (South China) and their implications for biostratigraphic correlation. J. Paleontol. 88, 1–67. https://doi.org/10.1666/12-157r.

Xiao, S., Narbonne, G.M., Zhou, C., Laflamme, M., Grazhdankin, D.V., Moczydłowska-Vidal, M., Cui, H., 2016. Toward an Ediacaran time scale: Problems, protocols, and

prospects. Episodes 39, 540–555. https://doi.org/10.18814/epiiugs/2016/v39i4/103886.

Xiao, S., Cui, H., Kang, J., Mcfadden, K.A., Kaufman, A.J., Kitajima, K., Fournelle, J.H., Valley, J.W., 2019. Using SIMS data to understand the role of authigenic carbonate in the origin of chaotic stratigraphic variations of carbon isotopes in the early Ediacaran Doushantuo Formation, Geological Society of America annual meeting, Phoenix, Arizona, USA. https://doi.org/10.1130/abs/2019AM-335046.

Xiao, S., Chen, Z., Pang, K., Zhou, C., Yuan, X., 2020a. The Shibantan Lagerstätte: insights into the proterozoic-phanerozoic transition. J. Geol. Soc. 178 https://doi.org/10.1144/jgs2020-135 jgs2020–135.

Xiao, S., Cui, H., Kang, J., McFadden, K.A., Kaufman, A.J., Kitajima, K., Fournelle, J.H., Schwid, M., Nolan, M., Baele, J.-M., Valley, J.W., 2020b. Using SIMS to decode noisy stratigraphic δ13C variations in Ediacaran carbonates. Precambrian Res. 343, 105686. https://doi.org/10.1016/j.precamres.2020.105686.

Yin, Z., Zhu, M., Davidson, E.H., Bottjer, D.J., Zhao, F., Tafforeau, P., 2015. Sponge grade body fossil with cellular resolution dating 60 Myr before the Cambrian. Proc. Natl. Acad. Sci. 112 https://doi.org/10.1073/pnas.1414577112. E1453-E1460.

Zhang, F., Xiao, S., Romaniello, S.J., Hardisty, D., Li, C., Melezhik, V., Pokrovsky, B., Cheng, M., Shi, W., Lenton, T.M., Anbar, A.D., 2019. Global marine redox changes drove the rise and fall of the Ediacara biota. Geobiology 17, 594–610. https://doi.org/10.1111/gbi.12359.

Zhao, M., Planavsky, N., Oehlert, A.M., Wei, G., Gong, Z., 2020. Simulating meteoric and mixing zone carbonate diagenesis with a two-dimensional reactive transport model. Am. J. Sci. 320, 599–636. https://doi.org/10.2475/09.2020.02.

Zhou, C., Xiao, S., 2007. Ediacaran δ13C chemostratigraphy of South China. Chem. Geol. 237, 89–108. https://doi.org/10.1016/j.chemgeo.2006.06.021.

Zhou, C., Bao, H., Peng, Y., Yuan, X., 2010. Timing the deposition of 17O-depleted barite at the aftermath of Nantuo glacial meltdown in South China. Geology 38, 903–906. https://doi.org/10.1130/g31224.1.

Zhou, C., Jiang, S., Xiao, S., Chen, Z., Yuan, X., 2012. Rare earth elements and carbon isotope geochemistry of the Doushantuo Formation in South China: implication for middle Ediacaran shallow marine redox conditions. Chin. Sci. Bull. 57, 1998–2006. https://doi.org/10.1007/s11434-012-5082-6.

Zhou, C., Guan, C., Cui, H., Ouyang, Q., Wang, W., 2016. Methane-derived authigenic carbonate from the lower Doushantuo Formation of South China: Implications for seawater sulfate concentration and global carbon cycle in the early Ediacaran Ocean. Palaeogeogr. Palaeoclimatol. Palaeoecol. 461, 145–155. https://doi.org/10.1016/j.palaeo.2016.08.017.

Zhou, C., Xiao, S., Wang, W., Guan, C., Ouyang, Q., Chen, Z., 2017. The stratigraphic complexity of the middle Ediacaran carbon isotopic record in the Yangtze Gorges area, South China, and its implications for the age and chemostratigraphic significance of the Shuram excursion. Precambrian Res. 288, 23–38. https://doi.org/10.1016/j.precamres.2016.11.007.

Zhou, C., Yuan, X., Xiao, S., Chen, Z., Hua, H., 2019. Ediacaran integrative stratigraphy and timescale of China. Sci. China Earth Sci. 62, 7–24. https://doi.org/10.1007/s11430-017-9216-2.

Zhu, M., Strauss, H., Shields, G.A., 2007a. From snowball earth to the Cambrian bioradiation: calibration of Ediacaran–Cambrian earth history in South China. Palaeogeogr. Palaeoclimatol. Palaeoecol. 254, 1–6. https://doi.org/10.1016/j.palaeo.2007.03.026.

Zhu, M., Zhang, J., Yang, A., 2007b. Integrated Ediacaran (Sinian) chronostratigraphy of South China. Palaeogeogr. Palaeoclimatol. Palaeoecol. 254, 7–61. https://doi.org/10.1016/j.palaeo.2007.03.025.

Zhu, M., Lu, M., Zhang, J., Zhao, F., Li, G., Yang, A., Zhao, X., Zhao, M., 2013. Carbon isotope chemostratigraphy and sedimentary facies evolution of the Ediacaran Doushantuo Formation in western Hubei, South China. Precambrian Res. 225, 7–28. https://doi.org/10.1016/j.precamres.2011.07.019.